

**Editor-in-Chief B.E.Paton**

**EDITORIAL BOARD**

Yu.S. Borisov, A.Ya. Ishchenko,  
B.V. Khitrovskaya (*exec. secretary*),  
V.F. Khorunov, I.V. Krivtsun,  
S.I. Kuchuk-Yatsenko (*vice-chief editor*),  
V.I. Kyrian, Yu.N. Lankin,  
V.N. Lipodaev (*vice-chief editor*),  
L.M. Lobanov, A.A. Mazur,  
O.K. Nazarenko, I.K. Pokhodnya,  
V.D. Poznyakov, I.A. Ryabtsev,  
K.A. Yushchenko,  
A.T. Zelnichenko (*exec. director*)

**INTERNATIONAL EDITORIAL  
COUNCIL**

N.P. Alyoshin (Russia)  
Guan Qiao (China)  
V.I. Lysak (Russia)  
B.E. Paton (Ukraine)  
Ya. Pilarczyk (Poland)  
O.I. Steklou (Russia)  
G.A. Turichin (Russia)  
M. Zinigrad (Israel)  
A.S. Zubchenko (Russia)

**Founders**

E.O. Paton Electric Welding Institute  
of the NAS of Ukraine,  
International Association «Welding»

**Publisher**

International Association «Welding»

*Translators:*

A.A. Fomin, O.S. Kurochko,  
I.N. Kutianova, T.K. Vasilenko  
*Editor*  
N.A. Dmitrieva  
*Electron galley*  
D.I. Sereda, T.Yu. Snegiryova

**Address**

E.O. Paton Electric Welding Institute,  
International Association «Welding»  
11, Bozhenko Str., 03680, Kyiv, Ukraine  
Tel.: (38044) 200 60 16, 200 82 77  
Fax: (38044) 200 82 77, 200 81 45  
E-mail: journal@paton.kiev.ua  
www.patonpublishinghouse.com  
URL: www.rucont.ru

State Registration Certificate  
KV 4790 of 09.01.2001  
ISSN 0957-798X

**Subscriptions**

\$348, 12 issues per year,  
air postage and packaging included.  
Back issues available.

All rights reserved.

This publication and each of the articles  
contained herein are protected by copyright.  
Permission to reproduce material contained in  
this journal must be obtained in writing from  
the Publisher.

## CONTENTS

### SCIENTIFIC AND TECHNICAL

*Makhnenko V.I., Makhnenko O.V., Velikoivanenko E.O.,  
Rozyinka G.F. and Pivtorak N.I.* Indices of pore formation in  
heat treatment of welded assemblies from steels susceptible  
to tempering cracking ..... 2

*Kostin V.A., Grigorenko G.M., Solomijchuk T.G., Zhukov V.V.  
and Zuber T.A.* Microstructure of HAZ metal of joints of  
high-strength structural steel WELDOX 1300 ..... 6

*Volpp J., Gatzen M. and Vollertsen F.* Simplified analytical  
modeling of dynamic behavior of the keyhole for different  
spatial laser intensity distributions during laser deep  
penetration welding ..... 14

*Markashova L.I., Poklyatsky A.G. and Kushnaryova O.S.*  
Influence of welding processes on the structure and  
mechanical properties of welded joints of aluminium alloy  
1460 ..... 18

*Akhonin S.V., Belous V.Yu., Muzhichenko A.F. and Selin R.V.*  
Mathematical modelling of structural transformations in HAZ of  
titanium alloy VT23 during TIG welding ..... 24

*Maksymova S.V., Khorunov V.F. and Voronov V.V.* Effect of  
size of the gap and initial state of the brazing filler alloy on  
formation of structure of the titanium alloy brazed joints ..... 28

### INDUSTRIAL

*Pokhodnya I.K., Yavdoshchin I.R., Skorina N.V. and Folbort  
O.I.* New electrodes for repair surfacing of railway frogs ..... 34

*Shlepakov V.N., Gavrilyuk Yu.A., Kotelchuk A.S., Ignatyuk  
V.N., Kosenko P.A., Rokhlin O.N. and Topchy A.V.* Application  
of mechanized welding with self-shielding flux-cored wire in  
repair of metallurgical equipment ..... 38

*Krivtsun I.V., Bushma A.I. and Khaskin V.Yu.* Hybrid  
laser-plasma welding of stainless steels ..... 46

*Knysh V.V., Klochkov I.N. and Berezin I.V.* Improvement of  
fatigue strength of overlap joints of sheet aluminium alloys  
made by fusion welding ..... 51

*Chernyak Ya.P.* Experience in cladding of parts and units of  
construction and road-building machinery ..... 54

News ..... 5, 13, 27, 37, 50

### INFORMATION

News ..... 58

Rules for Journal Authors ..... 59



# INDICES OF PORE FORMATION IN HEAT TREATMENT OF WELDED ASSEMBLIES FROM STEELS SUSCEPTIBLE TO TEMPERING CRACKING

V.I. MAKHNENKO, O.V. MAKHNENKO, E.O. VELIKOIVANENKO, G.F. ROZYNKA and N.I. PIVTORAK

E.O. Paton Electric Welding Institute, NASU

11 Bozhenko Str., 03680, Kiev, Ukraine. E-mail: office@paton.kiev.ua

It is well-known fact that the welded joints from heat-resistant steel of 10GN2MFA type, widely used in power engineering, have a tendency to formation of tempering cracks. Aim of the present work was a grounded explanation of reasons of crack appearance as well as understanding of mechanisms of their preventing based on pore formation in material creep. It is shown in the work using published experimental data of Prof. I. Hryvnyak on this problem and attracting modern statements of mechanism of pore formation in plastic deforming (strain ageing) that mechanism of section loss near the grain boundary in HAZ metal becomes significantly apparent in two-hour holding at 700–600 °C temperature due to pore formation at relaxation of high tempering residual stresses. Efficiency of heat treatment (relaxation of high residual stresses related with manufacture and, in particular, with repair of critical structures from considered steel) is rapidly reduced at tempering temperatures below 600 °C. Therefore, existing anxieties related with effect of modes of high tempering on appearance of tempering cracks in HAZ at fusion welding of specified type of steel are grounded enough and require particular attention to problems of determination of permissibility of corresponding repairs and development of suitable technologies on modes of post-weld heat treatment. This allows significantly reducing operation expenses. 8 Ref., 2 Tables, 3 Figures.

**Keywords:** tempering cracks in HAZ of low-alloy steel, strain ageing, relaxation of residual stresses, grain-boundary diffusion, pore formation

Tempering (reheating) or strain ageing cracks are one of the most character defects of welded structures manufactured from some modern low-alloy Cr–Mo steels. These defects have intercrystalline character (Figure 1) and appear, as a rule, in the HAZ in coarse grain areas. Effect of chemical composition of steel on tendency to formation of tempering cracks is determined by equation based on the results of experiments for low-alloy steel with maximum 1.5 % Cr [1]:

$$\Delta G = Cr + 3.3Mo + 3.1V + 10C - 2. \quad (1)$$

If  $\Delta G > 0$ , then steel is susceptible to formation of tempering cracks. Besides the chemical composition, an appearance of the tempering cracks is affected by mode of reheating (high tempering), namely time of material holding at high temperature promoting its strain aging. Figure 2 shows the data of Prof. Hryvnyak [2] concerning the effect of temperature of two-hour holding in reheating of the specimens of 10GN2MFA steel welded joint from near-weld zone ( $\Delta G = 0.8\text{--}1.4$ ) on value of nominal (applied) tensile stresses, necessary for obtaining of studied failure (see Figure 1). It can be seen that the temperature of two-hour holding provides significant effect on minimum allowable value of applied stresses at which formation of tempering cracks takes place (see Figure 2).

The failures were observed at 700–580 °C tempering temperature and 280–380 MPa nominal stresses, and there were no studied failures at temperatures below 550 °C even with nominal stresses above 625 MPa.

Consideration of only grain-boundary diffusion of additives and corresponding grain boundary embrittlement can not explain these facts. It can be assumed that process of nucleation and growth of pores, related with relaxation of sufficiently high residual welding stresses, and cor-

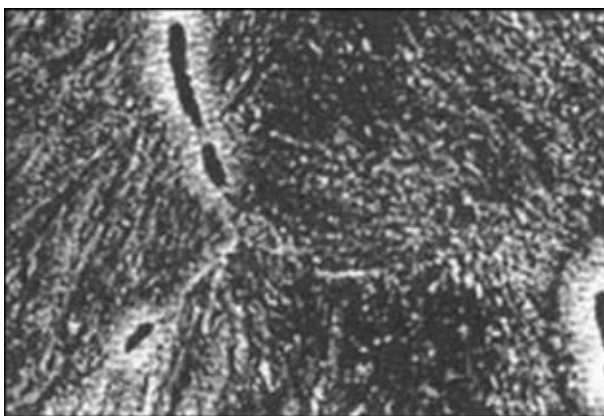


Figure 1. Appearance of cavities on initial stage of tempering crack formation in HAZ metal ( $\times 2000$ )



responding growth of creep deformations due to residual elastic deformations after welding have certain effect here. Series of works [1, 2 etc.] studied such a mechanism of strain ageing of material in the near-weld zone connected with development of diffusion plasticity (creep) deformations in relaxation of residual elastic deformations after welding. Certain degradation of properties of studied steel is possible in power engineering, where 10GN2MFA type steel is widely used (steam generators, circulation pipeline of WWER-1000 etc.) at total duration of holding of welded assemblies at high temperatures (above 580 °C) in process of manufacture and repair (in particular, when technological process of welding is alternated with intermediate tempering).

This work makes an effort of obtaining of grounded solution for given problem based on modelling of mechanism of pore formation in material creep.

Pore formation in creep results in reduction of net sections of structural elements, that naturally increases net stresses approximating them to critical ones. This sufficiently simple idea is used in development of corresponding solutions in material creep [3, 4 etc.] as well as at instantaneous plastic deformations [4–7 etc.]. Extent of reduction of net sections (1–S) of structural element in zone of potential crack formation (see Figure 1) can be approximately evaluated using data (see Figure 2) and applying dependence

$$\frac{1}{(1 - S)} \alpha_\sigma = \frac{\sigma_{cr}}{\sigma_{test}}, \quad (2)$$

where  $S$  is the relative sectional area of structural element occupied by pores;  $\alpha_\sigma$  is the stress concentration related with notch;  $\sigma_{test}$  are the testing stresses;  $\sigma_{cr}$  are the critical stresses at testing temperature (~20 °C).  $\sigma_{cr} < 625$  MPa on results of tests (after high tempering at  $T \leq 550$  °C) that allows getting an inequality from (2):

$$S = 1 - \frac{\sigma_{test} \alpha_\sigma}{\sigma_{cr}} > 1 - \frac{\sigma_{test}}{625}. \quad (3)$$

Data, given in Table 1, show that a mechanism of section loss in near-boundary zone becomes sufficiently apparent due to pore formation at relaxation of the residual welding stresses in a process of high tempering under condition of approximately similar level of embrittlement of grain boundary in HAZ metal on mechanism of grain-boundary diffusion at 700–550 °C of two-hour holding.

Experimental data on relaxation of residual welding stresses in HAZ metal near fusion boundary in arc welding of studied steel (Figure 3) are

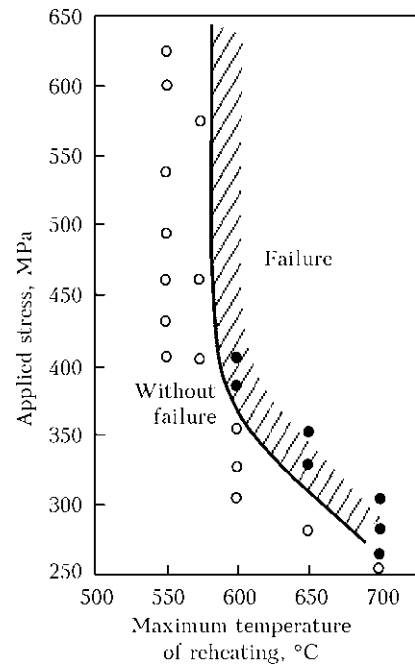


**Figure 2.** Effect of applied stresses and maximum temperature of reheating on tempering crack formation in specimens from 10GN2MFA steel with notch after simulation of heat cycle:  $T_{max} = 1300$  °C;  $\Delta t_{800-500} = 100$  s;  $\Delta G \approx 0.8-1.4$  (1)

given in work [2]. It follows from them that the residual stresses in considered zone reduced from corresponding yield point  $\sigma_y(T)$  up to values indicated in Figure 3 and Table 2, respectively, depending on temperature of two-hour high tempering. Rates of deformations of diffusion plasticity

$\dot{\epsilon}_{ij}^c = \frac{d\epsilon_{ij}^c}{dt}$  were calculated on these data [8]

for four variants of temperatures of two-hour holding using sufficiently popular formulation:

$$\dot{\epsilon}_{ij}^c = \Omega_1(\sigma_i)\Omega_2(T)(\sigma_{ij} - \delta_{ij}\sigma). \quad (4)$$

Here  $\epsilon_{ij}^c$  are the components of tensor of creep deformations ( $i, j = x, y, z$ );  $\sigma_i$  is the intensity of stresses;  $(\sigma_{ij} - \delta_{ij}\sigma)$  is the stress deviator [8];  $\Omega_1(\sigma_i)$  is the stress function;  $\Omega_2(T)$  is the temperature function. At uniaxial tension in  $x$ -direction  $\sigma_i = |\sigma_{xx}|$ ;  $\sigma = \sigma_{xx}/3$ .

Differential equation concerning the rate of stress relaxation at given constant temperature  $T$  will be obtained at isothermal holding under

**Table 1.** Estimation of relative area of section of structural element occupied by pores depending on tempering parameters

$T, \text{ }^\circ\text{C}$	$\sigma_{test}, \text{ MPa}$	$S$
700	275	>0.56
650	325	>0.48
600	375	>0.40
550	625	>0

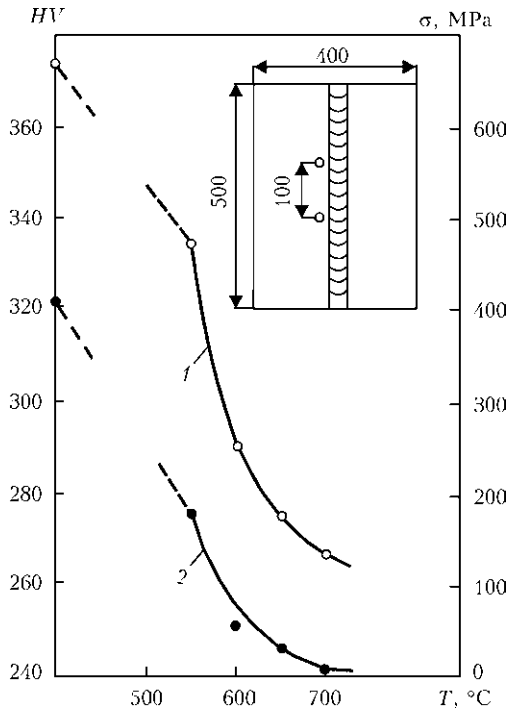


**Figure 3.** Effect of temperature of two-hour high tempering after welding on value of residual stresses (1) and hardness (2) in weld zone (on insert is a sample of joint with weld)

condition that  $\Omega_1(\sigma_i) = \sigma_i^n$  ( $n = 4-5$ ) and

$\dot{\epsilon}_{xx}^c = \frac{1}{E} \frac{d\sigma_{xx}}{dt}$ , where  $E$  is the elasticity modulus:

$$\frac{d\sigma_{xx}}{\sigma_i^{n+1}} = \frac{2}{3} E\Omega_2(T)dt; \quad \sigma_{xx} > 0. \quad (5)$$

Solving of (5) under condition that  $\sigma_{xx}$  are set at  $t = 0$  and  $t = 2$  h allows obtaining the values of function  $\Omega_2(T)$ , indicated in Table 2:

$$\Omega_2(T) = \frac{3}{2E(T)nt} \left[ \frac{1}{\sigma_{xx}^n(t)} - \frac{1}{\sigma_{xx}^n(0)} \right], \quad (6)$$

$$\dot{\epsilon}_{xx}^c(\sigma_{xx}) = \frac{2}{3} \sigma_{xx}^{n+1}(t)\Omega_2(T), \quad 1/h. \quad (7)$$

If Rice–Tracy law of pore growth is used [5]

$$\frac{dl}{dt} = lK_1\dot{\epsilon}_{xx}^c \exp\left(K_2 \frac{\sigma_m}{\sigma_i}\right), \quad (8)$$

where  $l$  is the relative length of linear dimension of structural element occupied by pores;  $K_1 =$

$= 0.28$ ;  $K_2 = 1.5$ , then considering (7) the following will be obtained at constant temperature:

$$\frac{dl}{l} = K_1\Omega_2(T) \left[ \exp\left(K_2 \frac{\sigma_m}{\sigma_i}\right) \right] \frac{2}{3} \sigma_{xx}^{n+1}(t)dt, \quad (9)$$

from which

$$\ln \frac{l^{(k+1)}}{l^{(k)}} = K_1\Omega_2(T) \frac{2}{3} \int_{t_k}^{t_{k+1}} \sigma_{xx}^{n+1}(t') \exp\left(K_2 \frac{\sigma_m}{\sigma_i}\right) dt', \quad (10)$$

where  $l^{(k)}$ ,  $l^{(k+1)}$  are the dimensions corresponding to points of time  $t_k$  and  $t_{k+1}$ .

At uniaxial tension  $\sigma_m/\sigma_i = 0.3$  and, respectively,

$$l^{(k+1)} = l^{(k)} \exp\left[ K_1\Omega_2(T) \frac{2}{3} e^{0.45} \int_{t_k}^{t_{k+1}} \sigma_{xx}^{n+1}(t') dt' \right] \quad (11)$$

after integration in (11) will obtain

$$l^{(k+1)} = l^{(k)} \exp\left[ K_1\Omega_2(T) \frac{2}{3} e^{0.45} (\bar{\sigma}_{xx}^{n+1}) \Delta t_{k+1} \right], \quad (12)$$

where  $\bar{\sigma}_{xx}^{n+1}$  is the average  $\sigma_{xx}^{n+1}$  value in  $\Delta t_{k+1} = t_{k+1} - t_k$  interval.

Since the kinetics of stress change  $\sigma_{xx}(t)$  in  $\Delta t_k$  interval at  $t_k = 0$  and  $t_{k+1} = 2$  h can arbitrarily change in the limits from  $\sigma_{xx}(0) = \sigma_y(T)$  up to  $\sigma_{xx}(t) \approx 0$  at  $t = 2$  h in the real welded joint (depending on conditions of fastening and geometry of joint) then  $\bar{\sigma}_{xx}^{n+1} = [0.5\sigma_y(T)]^{n+1}$  at  $n = 5$  can be used for evaluation of growth of initial linear dimensions of porosity  $l_0$ , related with heating and stress relaxation.

It can be seen on results of calculation (see Table 2) that relation  $l(t)/l_0$  can significantly change depending on temperature under specified conditions.

When it is considered that  $l_0$  value taking into account stage of heating and instantaneous plasticity deformations at stage when  $\sigma_{xx}(t) > \sigma_y(T)$  can be significant, and value of loss of net section  $S$  is related with  $l(t)$  by dependence

$$S = 1 - 2l(t) = 1 - 2l_0w \quad (13)$$

**Table 2.** Temperature function  $\Omega_2(T)$  for variants of two-hour high tempering

$T, ^\circ\text{C}$	$E \cdot 10^{-3}, \text{MPa}$	$\sigma_y(T), \text{MPa}$	$\sigma, \text{MPa} (t = 0)$	$\sigma, \text{MPa} (t = 2 \text{ h})$	$\Omega_2(T), \text{MPa}^{-(n+1)} \cdot \text{h}^{-1} (n = 5)$	$l(t)/l_0 = w (t = 2 \text{ h})$
700	1.60	120	120	12	$3.77 \cdot 10^{-12}$	1.10847
650	1.65	250	250	35	$1.73 \cdot 10^{-14}$	1.03939
600	1.70	300	300	60	$1.13 \cdot 10^{-15}$	1.00756
550	1.75	330	330	180	$0.43 \cdot 10^{-17}$	1.00005



( $x$  values are given in Table 2), then necessary data (see Table 1) on  $l_0$  are determined from condition  $l_0 = \frac{1-S}{2\omega}$  (13), from which at

$$T = 700 \text{ }^\circ\text{C}, l_0 \approx 0.44/2.29 = 0.198;$$

$$T = 650 \text{ }^\circ\text{C}, l_0 \approx 0.52/2.10 = 0.25;$$

$$T = 600 \text{ }^\circ\text{C}, l_0 \approx 0.6/2.09 = 0.298;$$

$$T = 550 \text{ }^\circ\text{C}, l_0 \approx 1.0/2.0001 = 0.5.$$

Such tendency of  $l_0$  dependence on temperature of two-hour high tempering is sufficiently logic since provides theoretic confirmation of existing anxieties relatively to effect of mode of reheating for welded structures from steel of 10GN2MFA type [2].

Therefore, performed calculations allow stating that the welded joints from heat-resistant low-alloy steel of 10GN2MFA type have high susceptibility to strain ageing at tempering temperatures above 600 °C. Efficiency of heat treatment that provides relaxation of high residual stresses related with manufacture and, in particular, repair of critical parts from this steel (for example, in power engineering, equipped with corresponding equipment of Russian production) rapidly reduces at tempering temperatures below

600 °C. Hence, corresponding attention should be made to problems of determination of allowable boundaries of respective repairs and development of adequate technological modes of post-weld heat treatment. This will allow significantly reducing costs for equipment operation.

1. Nakamura, H., Naiki, T., Okabayashi, H. Stress relaxation cracking in the HAZ. *IIW Doc. IX-648-69, X-531-69*.
2. Hrivnak, I. (1984) *Weldability of steels*. Ed. by E.L. Makarov. Moscow: Mashinostroenie.
3. Kachanov, L.M. (1956) *Fundamentals of theory of plasticity*. Moscow: Gostekhizdat.
4. Kachanov, L.M. (1961) *Time of fracture under creep conditions. Problems of continuum mechanics*. Moscow: AN SSSR.
5. Karzov, G.P., Margolin, B.Z., Shvetsova, V.A. (1993) *Physico-mechanical modeling of fracture processes*. St.-Petersburg: Politekhnik.
6. Makhnenko, V.I., Velikoivanenko, E.A., Rozyinka, G.F. et al. (2012) Consideration of pore formation at estimation of limiting state in zone of pressure vessel wall thinning defect. *The Paton Welding J.*, **12**, 2-8.
7. Ruggieri, C. (2004) Numerical investigation of constraint effects on fracture in tensile specimens. *J. Braz. Soc. of Mech. Sci. & Eng.*, **16**(2), 190-199.
8. Makhnenko, V.I. (2006) *Resource of safety service of welded joints and assemblies of current structures*. Kiev: Naukova Dumka.

Received 24.12.2012

## NEWS

### *System of Monitoring the Technical State of Pipelines Based on Software and Hardware Means*

Decision on extension of operating life should be taken in a differentiated manner, allowing for the features of operation of each individual section and its technical condition. This condition, as well as transition from traditional standard repair and maintenance of the pipeline to operation based on the technical condition, predetermined the block diagram of the monitoring system suggested by the E.O. Paton Electric Welding Institute together with the Institute of Geography and G.S. Pisarenko Institute for Problems of Strength, which includes the database on the condition of individual pipeline sections and analytical block for taking the respective decisions.

The database is formed on the basis of the data obtained from technical documentation and during inspections, and is designed for storage of all the currently available data on pipelines, including the data on crossings, pipe laying, soil types, electrochemical protection potentials, state of insulating coating, detected defects, use of pipeline fittings, working parameters, topographic maps of pipeline corridors, etc. Database interface enables the user to view various data types, making enquiries, and editing the available data.

The core of the analytical block is the model of assessment of relative risk, allowing for the consequences of a probable accident in each specific pipeline section. This model uses database information and allows establishing an

acceptable risk level for the operator under the conditions of limited technical and financial resources.

Distinctive features of the monitoring system are the possibility of evaluation of hazards and risk of accidents in the pipeline taking into account:

- prediction of residual life based on statistical methods of processing of results of examination in test holes;
- determination of stress-strain state of typical pipeline elements by FEA, also in the presence of surface noncrack-like defects;
- assessment of the condition of insulating coating based on application of above-route method;
- assessment of near surface part of the lithosphere in pipeline route regions.

Based on continuous collection, accumulation, processing and analysis of information on the actual condition of the pipeline, the system allows determination of the possibility of further operation of both the individual sections, and the pipeline as a whole, and taking the appropriate preventive and corrective actions in time. As a result, the level of safe operation of the real pipelines is significantly increased due to prompt acquisition of visual reference information and expert evaluations based on the procedure of assessment of the residual life and problem-oriented software.



# MICROSTRUCTURE OF HAZ METAL OF JOINTS OF HIGH-STRENGTH STRUCTURAL STEEL WELDOX 1300

V.A. KOSTIN, G.M. GRIGORENKO, T.G. SOLOMIJCHUK, V.V. ZHUKOV and T.A. ZUBER

E.O. Paton Electric Welding Institute, NASU

11 Bozhenko Str., 03680, Kiev, Ukraine. E-mail: office@paton.kiev.ua

Investigation of weldability of high-strength WELDOX 1300 steel with more than 1300 MPa yield limit is conducted under joint Ukrainian-Polish project, in order to assess the prospects for its application in crane construction in Ukraine. The objective of the work consisted in investigation of initial microstructure of WELDOX 1300 steel in as-delivered condition, influence of welding thermal cycle parameters on it, as well as plotting the thermokinetic diagram of austenite decomposition in this steel. This will allow optimization of arc welding modes to ensure high performance of the metal of weld and welded joint as a whole. The work was performed with application of procedures of light metallography, scanning microscopy, simulation of austenite transformation in Gleeble 3800 system, and computational methods of investigation. It was established that the microstructure of high-strength WELDOX 1300 steel in as-delivered condition consists of bainite-martensite mixture with a large number of finely-dispersed (50–100 nm) differently directed acicular precipitates of carbides of niobium NbC, titanium TiC, and iron Fe<sub>3</sub>C. A diagram of austenite transformation in this steel was plotted, and characteristic temperatures with new phase formation were determined. It is shown that preheating temperature should not be lower than 150 °C, in order to prevent cold cracking in welding WELDOX 1300 steel. Results of this work can be used in development of new welding technologies. 10 Ref., 4 Tables, 7 Figures.

**Keywords:** *new steels, carbonitride strengthening, welding thermal cycle, Gleeble 3800, microstructure, bainite, martensite, acicular ferrite*

One of the main problems of development of modern mechanical engineering is improvement of technico-economic indices of machines, mechanisms and engineering facilities based on lowering of their specific metal content, and improvement of operational reliability and fatigue life. When solving this problem, new superstrong steels (with more than 1000 MPa yield limit) with increased values of mechanical and toughness properties have an important role. The need for steels with such high values of strength is connected to a certain extent to the need for fabrication of metal structures of high-capacity cranes (250 t and higher).

Abroad the telescopic booms of truck cranes are usually made of STE 960 steel. In Ukraine the analogs of this steel are 12KhGH3MAFD and 15KhGN2MAFYuch steels. At present investigation of weldability of high-strength steel WELDOX 1300 with more than 1300 MPa yield limit was started under joint Ukrainian-Polish project in order to assess the prospects for its application in local crane construction.

As a rule, high-strength steels are used to manufacture booms and rotary platforms in crane structures. Individual parts of these structures

are connected to each other using arc welding processes. The thus formed welded joints should be characterized by equivalent strength and high impact toughness.

The weakest area in welded joints of high-strength steels is the HAZ, as the structure and properties of metal in it can undergo significant changes under the impact of the welding thermal cycle (WTC). This occurs both as a result of grain growth, and because of formation of quenching structures, lowering their brittle fracture resistance.

It is well-known that steel microstructure and the nature of its change in the metal of weld and HAZ essentially influence mechanical properties, ductility, toughness, and cold resistance of the welded joint as a whole. However, the data available in publications on the features of structural changes in WELDOX 1300 steel are scarce and unsystematic [1–3].

In this connection, the objective of this work consisted in investigation of initial microstructure of WELDOX 1300 steel in as-delivered condition, and influence of WTC parameters on it, as well as in plotting a thermokinetic diagram of austenite decomposition of this steel, that will allow establishing the optimum welding modes, providing high performance of the welded joint and studying the features of microstructure for-



**Table 1.** Composition of studied steel WELDOX 1300, wt.%

Object of study	C	Si	Mn	Cr	Ti	Ni	Mo	Nb	V	Cu	N	S	P
Steel WELDOX 1300 (UK_Special Data Sheet)	0.25	0.50	1.40	0.80	0.02	2	0.70	0.04	0.08	0.10	0.01	0.005	0.020
Steel WELDOX 1300	0.241	0.204	0.92	0.48	0.004	1.27	0.35	0.021	0.02	0.02	–	0.005	0.009

**Table 2.** Carbon equivalent values for WELDOX 1300 steel

Sheet thickness, mm	Certificate		Experiment	
	CEV, %	CET, %	CEV, %	CET, %
8	0.63	0.40	–	–
10	0.65	0.42	0.65	0.42

*Note.*  $CEV = C + Mn/6 + (Cr + Mo + V)/5 + (Ni + Cu)/15$ ;  
 $CET = C + (Mn + Mo)/10 + (Cr + Cu)/20 + Ni/40$ .

mation in the metal of weld and HAZ of this steel.

Composition of studied WELDOX 1300 steel in as-delivered condition and its comparison with those stated in the certificate (WELDOX\_1300\_UK\_Special Data Sheet: 2005-10-150) are given in Table 1.

High-strength steel WELDOX 1300 contains a large number of alloying elements, so that weldability is an urgent problem for it. Calculated and experimental values of carbon equivalent, depending on sheet thickness, are given in Table 2.

By the level of carbon equivalent this steel can be classified as steel with limited or poor weldability [4].

Mechanical properties of WELDOX 1300 steel stated in the certificate and determined experimentally, and weld metal properties are given in Table 3.

Investigations showed that the yield limit (about 1200 MPa) and ultimate strength (about 1600 MPa) of studied steel WELDOX 1300 are

approximately by 50–100 MPa lower than those stated in the certificate. As a result, characteristics of relative elongation (about 15 %) and reduction in area (61 %) increase 2 times at increase of impact toughness values.

Metallographic examination was performed using light microscope Neophot-32 at  $\times 500$  magnification and Auger-microprobe 9500F with high resolution field emission cathode in scanning electron microscope mode. Microstructure was revealed by etching in nital (4 % solution of nitric acid in alcohol). Vickers hardness measurement was conducted in the LECO hardness meter M-400 at 1 kg load. Calculation of structural components was performed by the field method to GOST 8233–56.

Initial microstructure of WELDOX 1300 steel is a bainite-martensite mixture (Figure 1, *a*), which consists approximately from 60–65 % of bainite and 35–40 % of martensite. Vickers hardness of base metal is equal to *HV1*-3780–3880 MPa.

Microstructural features of WELDOX 1300 steel in as-delivered condition were studied using Auger-microprobe 9500F with high resolution field emission cathode. It was shown that initial structure of WELDOX 1300 steel consists of uniformly distributed grains of bainite and martensite (9–10 grain point; Figure 1, *b*) with a large quantity of finely-dispersed carbide precipitates. Bainite packets are located mainly along the grain boundary, whereas martensite ones are in the grain bulk, that is related to development of austenite decomposition kinetics from the

**Table 3.** Mechanical properties of WELDOX 1300 steel and weld metal

Object of study	$\sigma_{0.2}$ , MPa	$\sigma_t$ , MPa	$\delta_5$ , %	$\psi$ , %	KCV, J/cm <sup>2</sup> , at T, °C	
					–40	–60
WELDOX 1300 (UK_Special Data Sheet)	1300	1700	8	37.9	27	27
WELDOX 1300 (base metal)	1157	1605	16.0	61.2	33	–
	1205	1604	15.6	61.4		
	1253	1602	14.6	60.5		
WELDOX 1300 (weld metal)	818*	1047*	13.3*	43.7*	21**	–
	763*	1009*	10.0*	46.2*		
	801**	953**	3.7**	9.8**		

\* Testing was conducted on samples with preheating temperature of 150 and \*\*120 °C.

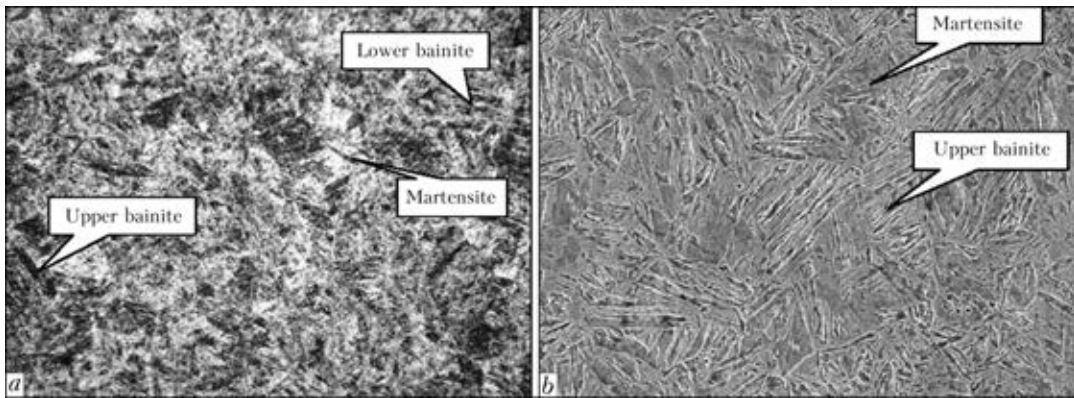


**Figure 1.** Microstructure of WELDOX 1300 steel in as-delivered condition: *a* – light microscopy ( $\times 500$ ); *b* – scanning microscopy ( $\times 2000$ )

boundaries towards the center of primary austenite grains.

Nature of carbide arrangement (Figure 2) in the bulk of bainite needles is indicative of the fact that lower bainite structure predominantly forms in these regions that is characterized by a favourable combination of strength and toughness properties. It is found that carbides have an acicular structure with needle dimensions of 50–100 nm. Proceeding from the data of X-ray structural analysis it was found that carbides of iron  $\text{Fe}_3\text{C}$  (in the amount of 0.52 %) and niobium  $\text{NbC}$  (0.04 %), and nitrides of aluminium  $\text{AlN}$  (0.01 %) and boron  $\text{BN}$  (0.01 %) form in the initial metal of WELDOX 1300 steel. Obtained data are in good agreement with those presented in [1]. Comparing the composition and nature of carbide precipitation in high-strength steels WELDOX 1300 and WELDOX 900, and using the method of electrolytical precipitation of carbides as a result of anode dissolution, the authors of the above work found that in WELDOX 900 steel strengthening is provided by nitrides of aluminium  $\text{AlN}$  and boron  $\text{BN}$ , whereas niobium carbides  $\text{Nb}_4\text{C}_{3.92}$  additionally form in WELDOX 1300 steel. Absence of iron carbides in the metal studied by the authors is, probably, related to dissolution of carbides of this type at anode dissolution.

To study the influence of WTC on HAZ metal structure, dilatometric investigations were performed and thermokinetic diagram of austenite transformation in WELDOX 1300 steel was plotted. Investigations were performed in Gleeble 3800 system, which allows simulation of thermodeformational cycle of welding on small diameter samples. For this purpose, samples of 6 mm diameter and 86 mm length were heated in a high-speed dilatometer up to 1350 °C at the rate of 150 °C/s, and then cooled in keeping with welding thermal cycles. During investigations the rate of metal cooling  $w_{6/5}$  was changed

from 1.3 up to 63 °C/s in the temperature range of 600–500 °C, that reproduces the main modes of arc welding of high-strength steels.

Processing of the results of dilatometric analysis and diagram plotting were performed by the generally accepted procedure. Quantitative analysis of the ratio of transformation products was conducted by dilatometric curves by the segment method [5].

In samples of WELDOX 1300 steel, in which structural transformations occur, the change of dimensions of dilatometric samples proceeds non-monotonically – metal expansion at the stage of its heating slows down (or is even replaced by compression), because of its contraction during  $\alpha \rightarrow \gamma$  transformation. At the cooling stage, contrarily, metal contraction is interrupted, because of its expansion in the temperature range of bainite-martensite transformations, which are completely over at temperatures below 150 °C and lead to development of high structural deformations.

Influence of cooling rate on austenite transformation temperature and HAZ metal microstructure is usually represented by thermokinetic diagram of austenite transformation. Proceeding from the results of dilatometric and metallographic analysis of simulator-samples, a ther-

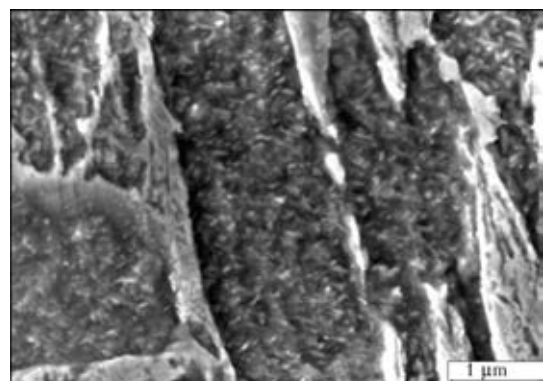


**Figure 2.** Microstructure of bainite grains

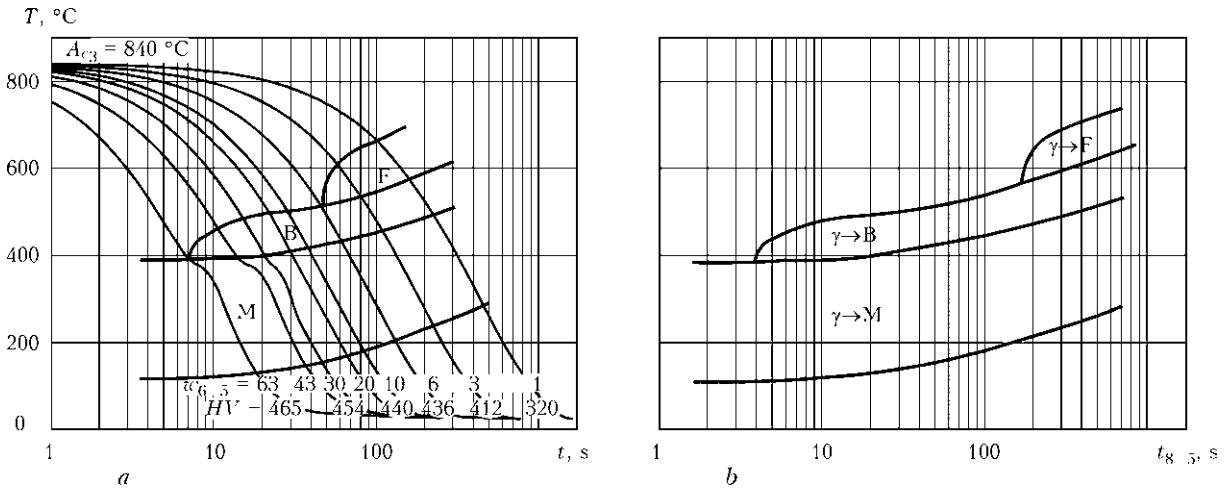


**Figure 3.** Thermokinetic diagrams of austenite decomposition for WELDOX 1300 steel: *a* – traditional; *b* – in temperature–cooling time  $t_{8/5}$  coordinates

mokinetic diagram of austenite transformation of WELDOX 1300 steel was plotted (Figure 3).

Austenite transformation in the studied range of cooling rates (from 1.3 up to 63 °C/s) occurs in the ferritic, bainitic and martensitic regions (Figure 3, *a*). At low cooling rates from 1.3 up to 6 °C/s, ferrite (F), bainite (B) and martensite (M) transformations will take place in HAZ metal of WELDOX 1300 steel. Solid solution alloying by molybdenum (0.8 %) and nickel (2 %) causes higher austenite stability, that results in the temperature of the start of ferrite transformation (at cooling rates of 3–5 °C/s) in this steel reaching extremely low values ( $F_s$  – of about 610–550 °C). With increase of cooling rate the quantity of ferrite gradually decreases and at 6 °C/s it disappears completely, and the structure consists of bainite and martensite.

Further increase of cooling rate up to 63 °C/s promotes intensive martensite transformation due to suppression of bainite transformation.

In the entire considered range of cooling rates ( $w_{6/5} = 1.3\text{--}63$  °C/s) temperature of the start  $M_s$  and end  $M_e$  of martensite transformation gradually decreases, with  $M_s$  temperature decreasing to a smaller degree (from 520 to 390 °C) than  $M_e$  temperature (from 290 to 110 °C) (Figure 3, *b*). Sample hardness rises from *HV* 320 up to *HV* 465.

At higher cooling rates ( $w_{6/5} > 63$  °C/s) a purely martensitic structure forms, and tempera-

ture of the start and end of structural transformations and hardness remain practically the same. With increase of the rate of cooling of WELDOX 1300 steel, the start and end of martensite transformations change in temperature range of 610–290 and 490–130 °C, respectively, and this leads to increase of martensite fraction in it from 35–40 up to 90–95 %. This steel is characterized by completion of the processes of austenite transformation – no residual austenite forms.

Increased content of alloying elements in WELDOX 1300 steel leads to a marked increase of  $M_s$  temperature of 520–390 °C (Figure 3, *b*). Comparison of calculated value ( $M_s = 480$  °C) of temperature of the start of martensite transformation with experimental data showed their quite good agreement in the region of low cooling rates:

$$M_s \text{ (}^\circ\text{C)} = 650 - 361C - 39Mn - 35V - 20Cr - 17Ni - 10Cu - 5Mo - 5W + 16Co + 30Al. \quad (1)$$

Thus, in order to obtain an equivalent joint of base and HAZ metal, it is necessary for cooling rate  $w_{6/5}$  to be higher than 6 °C/s. This cooling rate is in good agreement with the cooling rate recommended for welding high-strength steel with yield limit above 700 MPa, which, in the opinion of authors of [6], should be equal to  $10 \leq w_{6/5} \leq 20$  °C/s.

Having determined the optimal cooling rate of welded joint of WELDOX 1300 steel, appropriate process and modes of welding were se-

**Table 4.** Composition of weld metal of WELDOX 1300 steel and welding wire, wt.%\*

Object of study	C	Si	Mn	Cr	Ti	Ni	Mo	S	P
Flux-cored wire MEGAFIL-1100M	0.07	0.50	1.50	0.80	–	2.70	0.80	0.015	0.015
WELDOX 1300 weld	0.241	0.204	0.92	0.48	0.01	1.27	0.35	0.005	0.01

\*Nb, V ≈ 0.02 %, N = 0.06 %.

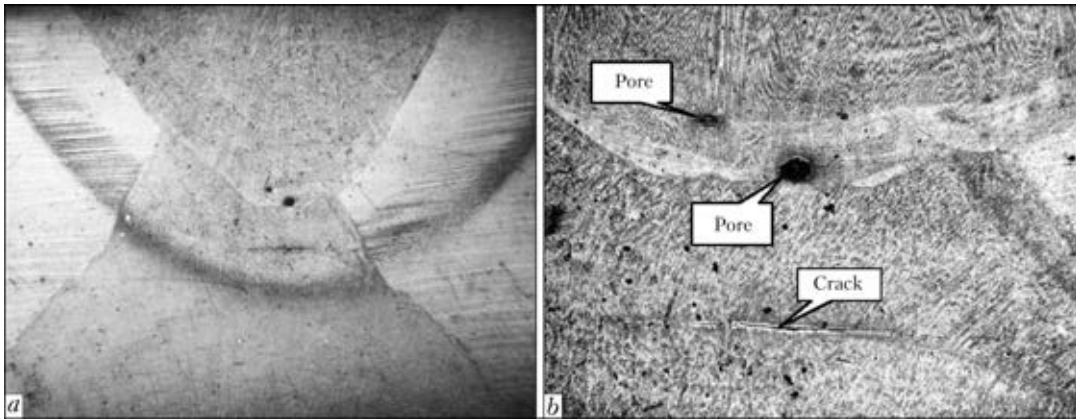


**Figure 4.** Macrostructure of weld on WELDOX 1300 steel: *a* – general view ( $\times 10$ ); *b* – cold cracks and pores in HAZ metal region ( $\times 50$ )

lected. Mechanized arc welding was conducted in argon with addition of  $\text{CO}_2$  gas (in the proportion of 82/18), respectively, with application of martensite type flux-cored wire MEGAFIL-1100R in the following mode:  $I_w = 250$  A,  $U_w = 30$  V,  $v_w = 14$  m/h.

Composition of weld metal and flux-cored welding wire is given in Table 4.

In order to avoid the possibility of cold cracking in welding WELDOX 1300 steel, preheating of plates to be welded was applied. Preheating temperature [7], which was calculated by equation (2), was equal to  $120$  °C:

$$T = 350\sqrt{[CE_{\text{tot}}] - 0.25}, \text{ } ^\circ\text{C}; \quad (2)$$

$$CE_c = \%C + \%Mn/6 + (\%Ni + \%Cu)/15 + (\%Cr + \%Mo + \%V)/5, \quad (3)$$

where  $CE_{\text{tot}}$  is the total carbon equivalent which is determined by expression  $CE_{\text{tot}} = CE_c + CE_s$ ;  $CE_c$  is the carbon equivalent dependent on metal composition, calculated by formula (2);  $CE_s$  is the carbon equivalent dependent on metal thickness, which is calculated by formula  $CE_s = 0.0058CE_c$  ( $\delta$  is the thickness of metal of welded part, mm).

Macrostructure of welded joint of WELDOX 1300 steel is given in Figure 4, *a*. Investigations showed that at preheating temperature of  $120$  °C individual microcracks of limited length (up to  $100$   $\mu\text{m}$ ) form in the zone of lower weld reheating (Figure 4, *b*). In our opinion, this circumstance accounts for lowering of weld metal ductility observed in joints of WELDOX 1300 steel in welding with preheating up to  $120$  °C. This leads to lower values of yield limit (801 MPa), strength (953 MPa) and ductility (3.7 and 9.8 % for relative elongation and reduction in area, respectively) of weld metal of steel WELDOX 1300 (see Table 3).

Increase of preheating temperature up to  $150$  °C leads to complete absence of cracks or

defects in the welded joint of WELDOX 1300 steel and to increase of yield limit (up to 1050 MPa) and ductility (13.3 and 43.7 % for relative elongation and reduction in area, respectively) of weld metal of WELDOX 1300 steel. Comparatively low values of mechanical properties of welds on WELDOX 1300 steel, compared to base metal properties, are related to absence of welding wires of sufficient strength in the world practical experience that would promote ensuring equivalent strength and cold resistance of welded joints of WELDOX 1300 steel.

Formation of cold cracks in the zone of crossing of two welds (Figure 4, *a*) is, apparently, related to the processes of carbide phase dissolution at reheating, at which the carbide forming elements (vanadium, molybdenum, niobium), but primarily carbon, go into the solid solution, causing considerable embrittlement of the matrix in this region. At cooling, increase of martensite lattice parameters leads to increase of local internal stresses, and their interaction with residual welding stresses leads to microcrack formation. This is indicated by the results of investigations, performed using computational methods by simulation of the processes of carbide phase dissolution in weld metal and HAZ during welding of WELDOX 1300 steel. This was performed using a computer program simulating phase transformations in metal systems at heating and cooling.

Calculation results on kinetics of the change of volume fraction and dimensions of carbide and nitride phases in the regions of HAZ metal of WELDOX 1300 steel, heated up to  $1400$  and  $1200$  °C with subsequent cooling at the rate of  $10$  °C/s, are shown in Figure 5.

Analysis of obtained results shows that depending on the applied WTC, processes of dissolution of carbide and nitride phases can proceed in characteristic regions of HAZ metal, strengthening WELDOX 1300 steel in as-delivered condition.

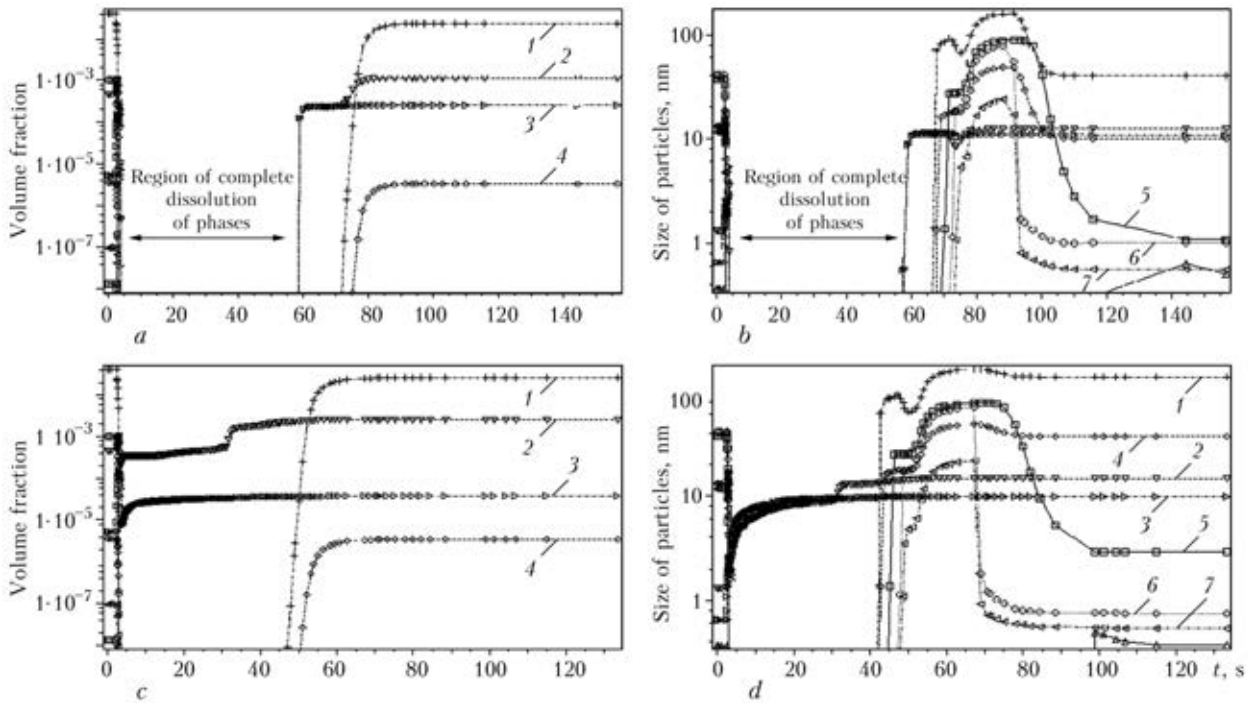


**Figure 5.** Design kinetics of variation in time of volume fraction (*a, c*) and dimensions (*b, d*) of carbide and nitride phases in HAZ regions of WELDOX 1300 steel heated up to 1400 (*a, b*) and 1200 (*c, d*) °C with subsequent cooling at  $w_{6/5} = 10$  °C/s: 1 – NbC; 2 – TiN; 3 – TiC; 4 – Fe<sub>3</sub>C; 5 – Me<sub>23</sub>C<sub>6</sub>; 6 – Me<sub>7</sub>C<sub>3</sub>; 7 – Me<sub>6</sub>C<sub>3</sub>

At maximum heating temperature of HAZ metal region (coarse-grained) complete dissolution of carbides of strengthening phases, namely TiC, NbC, Fe<sub>3</sub>C and nitride AlN can take place (Figure 5, *a, b*). In the fine-grained region, in which heating temperature does not exceed 1200 °C, nitrides and carbides of titanium TiC and TiN do not dissolve during the entire welding cycle (Figure 5, *c, d*).

It is well-known [8] that titanium nitrides TiN are almost insoluble in austenite. Computer simulation results obtained by us are in good agreement with the experimental results, given in [9], in which the temperatures of particle dissolution in austenite are 1350 (AlN), 1150 (NbC) and 1250 °C (TiC), respectively.

Investigation of microstructure of welded joint of WELDOX 1300 steel was conducted in

the central part of outer weld and its HAZ. Cast structure of the studied weld consists of columnar crystallites of different width. In the weld central part crystallite width changes from 20 up to 70 μm, and in the weld root the crystallites are much narrower: their width is equal to 10–15 μm.

Nature of Vickers hardness distribution across the section of welded joint of WELDOX 1300 steel is shown in Figure 6.

Upper weld microstructure (Figure 7, *a*) consists of dispersed interlaced ferrite needles or plates, oriented at angles of 60 and 90° relative to each other, with finely-dispersed carbide precipitates located along their boundaries. In its appearance such a structure is similar to acicular ferrite structure, forming in weld metal in welding of high-strength low-alloyed steels.

It is known that acicular ferrite forms as a result of transformation of inner regions of

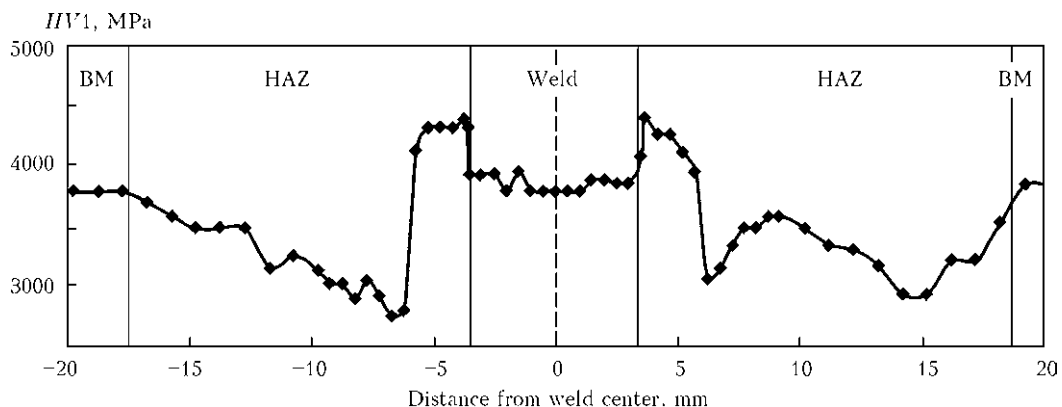


**Figure 6.** Hardness distribution across the section of the WELDOX 1300 steel welded joint

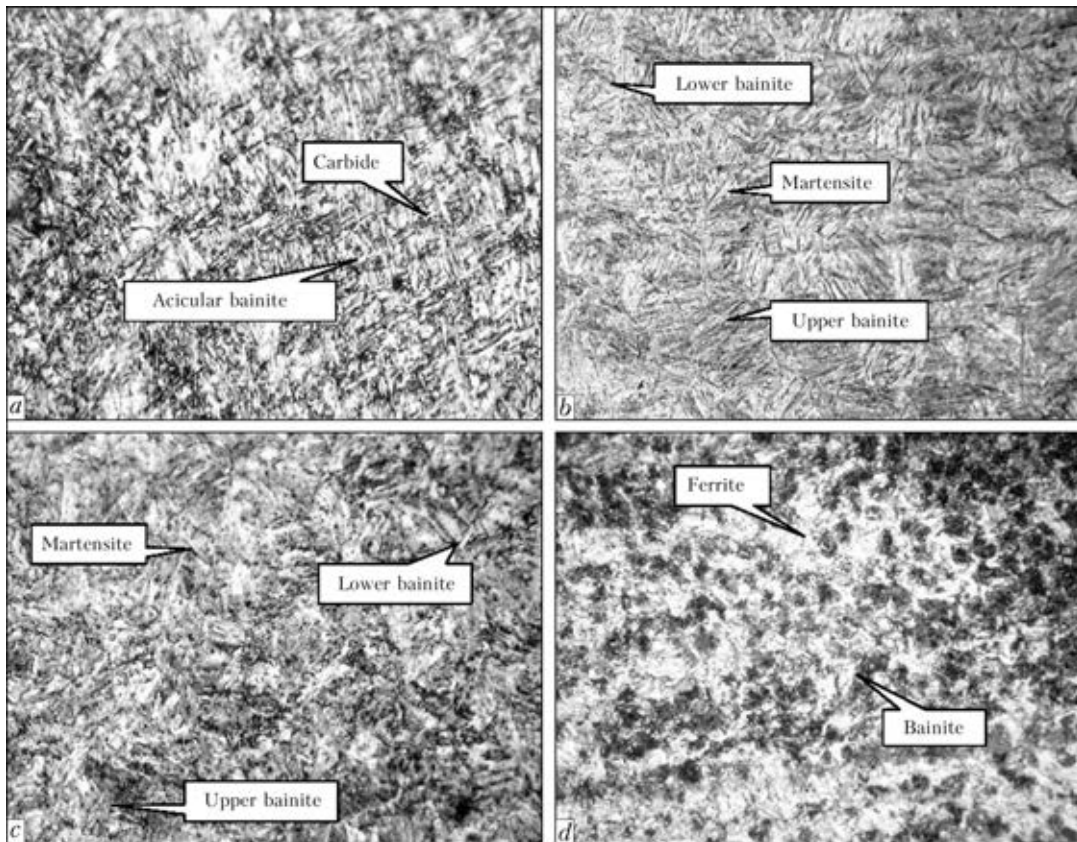


**Figure 7.** Microstructure ( $\times 1000$ ) of weld metal and HAZ of WELDOX 1300 steel made with application of MEGAFIL-110R wire: *a* – weld; *b* – coarse-grained region; *c* – fine-grained region; *d* – incomplete recrystallization region

austenite grains in the temperature range, which is only slightly higher than that of bainite transformation. Acicular ferrite is characterized by quite distinct features: these are fine elongated grains ( $1\text{--}3\ \mu\text{m}$ ) of a not quite regular shape with length to width ratios from 2:1 to 4:1. In upper weld microstructure the needles are much longer with 10:1 and greater ratio of length to width. In addition, Vickers hardness of such a structure is equal to  $HV1\text{--}3780\text{--}3950$  MPa, whereas hardness of «regular» acicular ferrite in the metal of welds of low-alloyed steels is equal to  $HV1\text{--}2400\text{--}2500$  MPa.

In this connection, the upper weld structure can be characterized as «acicular bainite», with needle arrangement in the form of «basket weave» characteristic of acicular ferrite [10].

Microstructure of coarse-grained region of HAZ metal (Figure 7, *b*) consists of structures of upper and lower bainite and martensite. In this region of welded joint hardness increase up to  $HV1\text{--}4320\text{--}4400$  MPa is observed. Fine-grained region also consists of bainite-martensite structure (Figure 7, *c*). Hardness of this region is somewhat lower than that of the coarse-grained region and is equal to  $HV1\text{--}3950\text{--}4130$  MPa. Hardness lowering in incomplete recrystallization region to  $HV1\text{--}2740$  MPa is related to the fact that a softer structural component, namely

ferrite, forms in the structure of this zone (Figure 7, *d*). Apparently, the rate of metal cooling in incomplete recrystallization region did not exceed  $6\ \text{°C/s}$  (see Figure 3, *a*), and this is exactly what led to formation of a large quantity (more than 50 %) of ferrite grains.

Lower hardness of welded joints of WELDOX 1300 steel made by flux-cored wire MEGAFIL-1100R in the atmosphere of shielding gases Ar +  $\text{CO}_2$  is due to the action of a number of factors, namely: formation of grains with ferrite structure of lower hardness ( $HV1\text{--}2740\text{--}3000$  MPa) in incomplete recrystallization region; dissolution of dispersed phases ( $\text{Fe}_3\text{C}$ , NbC, TiC), which levels the effect of carbide and carbonitride (dispersion) hardening; dissolution and transition of carbide-forming elements and carbon into the solid solution that increases the risk of cold cracking.

## Conclusions

1. Studying the microstructure of high-strength steel WELDOX 1300 in as-delivered condition showed that the initial steel microstructure consists of bainite-martensite mixture (about 60 % of bainite and 40 % of martensite). Bainite needles contain a large number of finely-dispersed ( $50\text{--}100\ \text{nm}$ ) differently oriented acicular pre-



cipitates of carbides of niobium NbC, titanium TiC and iron Fe<sub>3</sub>C (cementite).

2. A diagram of austenite transformation in new structural steel WELDOX 1300 was plotted, and it was found that at up to 6 °C/s cooling rates austenite transformation partially occurs in the diffusion region with formation of ferrite grains, whereas at increase of this cooling rate transformation runs in the region of intermediate and quenching structures.

3. Temperature of the start M<sub>s</sub> and end M<sub>e</sub> of austenite transformation gradually decreases, M<sub>s</sub> temperature decreasing to a smaller degree (from 520 to 390 °C) than M<sub>e</sub> temperature (from 290 to 110 °C). With increase of cooling rate of WELDOX 1300 steel, the start and end of bainite-martensite transformations changes in the temperature range of 610–290 and 490–130 °C, respectively, and leads to increase of martensite fraction in it from 35–40 up to 90–95 %, respectively.

4. It is found that the cause for low mechanical properties of welded joints of WELDOX 1300 steel is associated with formation of cold cracks in the region of reheating of the lower weld as a result of dissolution of carbide and nitride phases (Fe<sub>3</sub>C, TiN, TiC). Preheating temperature of 120 °C is insufficient to prevent cold cracking. At preheating temperature of 150 °C no mi-

crocracks or defects form in the weld metal of WELDOX 1300 steel.

- Ozgovicz, W., Kurc, A., Nawrat, G. (2008) Identification of precipitations in anodically dissolved high-strength microalloyed Weldox steels. *Archives of Materials Sci. and Eng.*, **31**, 95–100.
- Welding Hardox and Weldox. <http://www.ssab.com>
- Ozgovicz, W., Kalinowska-Ozgovicz, E. (2008) *Investigations on the impact strength of constructional high-strength Weldox steel at lowered temperature*. Vol. 32, 89–94.
- (1974) *Reference book of welder*. Ed. by V.V. Stepanov. Moscow: Mashinostroenie.
- Steven, W., Mayer, G. (1953) Continuous-cooling transformation diagrams of steels. Pt 1. *J. Iron and Steel Inst.*, **174**, 33–45.
- Zhdanov, S.L., Mikhoduj, L.I., Strizhak, P.A. et al. (1994) Structural transformations in welding of 17Kh2M steel and properties of welded joints. *Avtomatich. Svarka*, **9/10**, 10–13.
- Seferian, D. (1963) *Welding metallurgy*. Moscow: Metallurgizdat.
- Gorbachev, I.I., Popov, V.V. (2009) Analysis of solubility of carbides, nitrides and carbonitrides in steels by computer-assisted methods of thermodynamics. Pt 3: Solubility of carbides, nitrides and carbonitrides in Fe-Ti-C, Fe-Ti-N and Fe-Ti-C-N systems. *Fizika Metallov i Metallovedenie*, **108(5)**, 513–524.
- Hrivnak, I. (1969) The study of the system Fe-V-C-N with a view to the precipitation hardening process. *Czech. J. Physics*, **19**, 287.
- Grabin, V.F., Denisenko, A.V. (1978) *Metals science of low- and medium-alloy steels*. Kiev: Naukova Dumka.

Received 25.12.2012

## NEWS

### *Testing of Compensation Devices in Systems of Transportation of Heat Carriers*

At the E.O. Paton Electric Welding Institute the equipment has been designed and procedure has been developed for testing the telescopic compensators of heat systems, allowing evaluation of efficiency and serviceability of accepted design solutions; evaluating their service life under the conditions of loadings, simulating the complex of loads exceeding the planned term of service of products. Simultaneously, the testing of two compensators are carried out, which were assembled and mounted on the stand so that one of them was fixed in a stretched state, and another one – in a compressed state. Owing to this scheme the volume of internal cavity of the compensator remains unchanged in testing during the process of movement of branch pipe relative to a casing. Stand is equipped by a hydraulic system for

creation of excessive pressure of a required value inside the compensators, water heat source, and also a power system, providing a reciprocal movement of a mobile part of compensators at a preset speed, here the cyclic movement of a pipeline area is simulated. Compensators can be tested of different designs of diameter 200–800 mm at the following parameters: amplitude of movement is up to 250 mm; speed of movement is 0.5–6.0 cm/min; pressure of operating medium – preset; temperature of operating medium – up to 170 °C.

Using these tests, the optimizing of design of compensating devices and their welded elements, as well as evaluation and checking of their serviceability are made.



# SIMPLIFIED ANALYTICAL MODELING OF DYNAMIC BEHAVIOR OF THE KEYHOLE FOR DIFFERENT SPATIAL LASER INTENSITY DISTRIBUTIONS DURING LASER DEEP PENETRATION WELDING\*

J. VOLPP, M. GATZEN and F. VOLLERTSEN

BIAS – Bremer Institut fuer Angewandte Strahltechnik GmbH  
2 Klagenfurter Str., 28359, Bremen, Germany. E-mail: volpp@bias.de

During laser deep penetration welding a characteristic keyhole is created, when the intensity of laser beam exceeds material depending limit. The generated system of keyhole and surrounding melt pool is highly dynamic. Dynamics in the weld pool and in keyhole are mainly responsible for keyhole instabilities that can cause keyhole collapses during the welding process. This can lead to unwanted enclosures or pores that reduce the quality of welded joint. For better understanding of the complex system, a simplified analytical model of the keyhole is used providing a description of the keyhole geometry. It also calculates the influence of different spatial laser intensity distributions on keyhole dynamics and resultant tendency to form pores. The model is used to calculate the temperature on the keyhole wall from energy equation containing laser beam energy absorption, heat conduction and evaporation losses. The surface temperature is needed to calculate the keyhole radius by solving the pressure equilibrium equation. This contains the recoil pressure at the end of the Knudsen layer on the keyhole surface, which keeps the keyhole open against the surface tension pressure of the surrounding liquid material. In the second step, a dynamic equation that describes the keyhole behavior is used. The dynamic calculation is based on the force balance in the keyhole. To observe the influence of different spatial laser intensity distributions the Gaussian and top hat distribution are implemented in calculation. It can be found that the keyhole geometry is influenced by different laser intensity distributions and pressure gradient changes significantly leading to highly different dynamic behaviors. 18 Ref., 2 Figures.

**Keyword:** laser welding, deep penetration, keyhole, radiation intensity, spatial radiation, analytical model, keyhole geometry, weld metal, pore formation

Pores are one of the failures occurring in laser deep penetration welding that reduce weld quality. Pores can be formed due to chemical reasons [1], laser power instabilities [2], changes in absorptivity or process instabilities [3]. Weld pool and keyhole dynamics can cause the keyhole to collapse. A high amplitude of the oscillating keyhole walls leads to a closing of the keyhole. Gas enclosures are formed usually in the lower part of the keyhole [4]. The captured gas cannot escape to the surface and forms a bubble in the weld pool. After solidification of the weld pool a pore is formed [5]. Although keyhole dynamics have been a field of interest and a lot of research has been done, the complex system is still not completely understood. Experimental observa-

tions found process oscillations in the range from 1 [6] to 8 kHz [7], and it was concluded that these high frequencies must origin from keyhole oscillations.

There were also mathematical approaches describing the process in the keyhole. In several former works numerical approaches were used to describe the complex system. Ki et al. [8] presented the model including all important known physical effects taking place in the keyhole and weld pool. For observing oscillations in kilohertz ranges, a numerical calculation requires small time steps and high calculation time [9]. Therefore, an analytical description is desired. Analytical models need shorter calculation times but require simplifications. It is, for example, not possible to solve the heat conduction equation for arbitrary shapes. Research has been done in analytical modeling of the keyhole for quasi-static calculations [10] as well as for dynamic behavior calculations [11]. Most former works used the Gaussian beam as a beam source for calculations. But industrially used laser sources provide quite different intensity distributions.

\*Based on Proceedings of the 6th International Conference on Mathematical Modelling and Information Technologies in Welding and Related Processes (29 May–1 June, 2012, Katsiveli, Ukraine).



Kaplan [12] started to also consider the axial change of the intensity profile of the laser beam [13]. Not only the intensity value [14] and power oscillations [15] but also the spatial laser intensity distribution has been identified as being an influencing factor. The absorbed energy, temperature in the keyhole and pressure in it depend on the intensity and intensity profile of the beam [16]. Therefore, the influence of different intensity distributions of the laser beam are observed in this work with the aim of finding a way to reduce pores.

Based on these existing analytical models the influence of the Gaussian and top hat laser intensity distribution on keyhole geometry [10] and dynamics [11] is observed to obtain a better understanding of the keyhole process.

**Analytical model of the keyhole.** *Modeling quasi-static keyhole.* When the keyhole has formed due to high intensity of the laser beam a quasi-static condition is achieved. A cylindrical keyhole for thin sheets can be assumed that is completely penetrating the material. The macroscopic shape is conserved when the beam is moved relatively to the material. Due to the vaporization process an ablation or recoil pressure  $p_{abl}$  in the keyhole is built up that opens the keyhole and counteracts against the pressure of the surface tension  $p_\gamma$  of the surrounding melt pool. Mathematically the pressure balance equation can be expressed as

$$\Delta p = p_\gamma - p_{abl}. \tag{1}$$

Hydrodynamic and hydrostatic pressures can be neglected [17] as their dimension is much smaller than the one of the surface tension calculated with the Laplace description:

$$p_\gamma = \frac{\gamma}{r_{kap}}. \tag{2}$$

Surface tension pressure depends on the radius  $r_{kap}$  and the surface tension coefficient  $\gamma$ .

The ablation pressure  $p_{abl}$ , caused by vaporization of material on the keyhole wall in the so called Knudsen layer, can be calculated as

$$p_{abl} = mn(T_s)u^2(T_s), \tag{3}$$

where  $m$  is the atomic mass;  $n$  is the particle density;  $u$  is the velocity of evaporated particles. Particle density and velocity of evaporated particles are dependent on keyhole surface temperature  $T_s$  that can be calculated solving the energy equation as

$$q_{abs} = q_\lambda + q_{abl}. \tag{4}$$

The absorbed part of the energy  $q_{abs}$ , provided by the laser beam, can be calculated using

$$q_{abs} = \frac{1}{2\pi r d} \int i(r) r dr d\varphi, \tag{5}$$

where  $d$  is the sheet thickness;  $r$  and  $\varphi$  is the radial and azimuthal coordinate. Laser intensity distribution  $i$  in this equation is the parameter that can be varied.

Energy losses are mainly vapor losses ablating from the keyhole

$$q_{abl} = mn(T_s)u(T_s)H_v \tag{6}$$

and heat conduction losses

$$q_\lambda = \frac{T_s - T_0}{2} \rho c_p u_0 K_1(\text{Pe}) / K_0(\text{Pe}). \tag{7}$$

Here  $H_v$  is the latent heat;  $T_0$  is the ambient temperature;  $\rho$  is the density of the liquid material;  $c_p$  is the heat capacity;  $u_0$  is the welding speed;  $K_1$  and  $K_0$  is the modified Bessel functions of first and zero order depending on the Peclet number  $\text{Pe} = u_0 r_{kap} / 2\kappa$ , where  $\kappa$  is the thermal diffusivity. Equation (7) is the solution of the heat conduction equation describing losses through heat conduction assuming a simplified cylindrical heat source [10].

Calculating the surface temperature  $T_s$  at the wide range of radii, the pressure equilibrium equation  $\Delta p = 0$  can be solved, and quasi-static radii of the cylindrical keyhole can be determined.

*Modeling dynamic behavior of the keyhole.* To model the dynamic behavior of the keyhole differential equations are necessary. The cylindrical keyhole calculated above is assumed to oscillate only in the radial direction, and the intensity distribution is the parameter in the model. Including the composition of all forces  $F$  acting in the keyhole, the dynamic equation of radius can be written as follows:

$$\ddot{r} = \dot{b} = \frac{F}{m_{m.p}}, \tag{8}$$

where  $\ddot{r}$  is the radius normalized (to the beam radius) keyhole radius;  $\dot{b}$  is the rate of radius change;  $m_{m.p}$  is the melt pool mass. According to [11] the dynamic equation of velocity  $b$  is

$$\begin{aligned} \dot{b} = & 2\pi d(rp + 1) + 12\pi \frac{d^2}{r_0^2} r \times \\ & \times \frac{(1 - r^2)}{(c - r)^2(c^2 - r^2)} - fb, \end{aligned} \tag{9}$$

where  $c$  is the factor that accounts for the acceleration due to melt pool deformation at the top surface. First and second term in (9) describe velocities induced by ablation pressure, surface tension and melt pool deformation at the surface. The last term accounts for the viscous velocity dissipation, where  $f$  is the dissipation factor that causes damping of the system.

The dynamic pressure is described by [11]

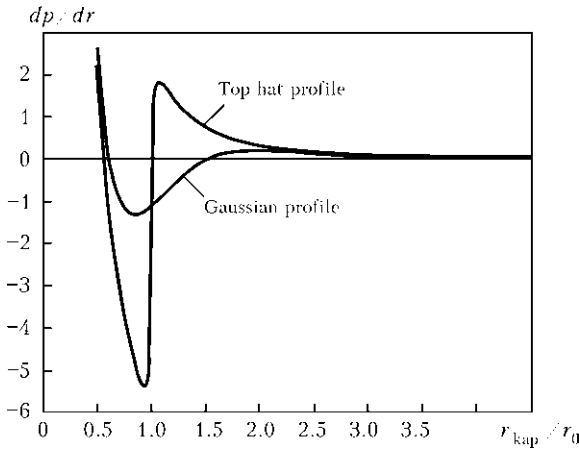


**Figure 1.** Pressure gradient for the Gaussian and top hat laser profile

$$\dot{p} = \sqrt{\frac{m_{m.p}}{\gamma}} \times \left( 2 \frac{v_a}{d} \left( \frac{p_0}{p_{eq}} - p \right) + \frac{c_0}{\pi d \rho_0 r_0^2} i(r, r_{kap}, r_0) - 2 p_0 r_{kap}^2 \frac{b}{r^3} \right) \quad (10)$$

Here  $\dot{p}$  is the pressure in the keyhole normalized to the quasi-static equilibrium pressure  $p_{eq}$ . The first part of the right hand side of (10) describes the pressure change due to vapor escaping through keyhole opening, where  $v_a$  is the assumed velocity of the exiting vapor;  $p_0$  is the ambient pressure. The pressure change due to laser evaporation is found in the second term, where  $c_0$  is the constant relating to laser power;  $r_0$  is the beam radius. The third term in (10) describes the pressure change due to adiabatic volume change of the keyhole. This set of differential equations can be solved, and the response on special perturbations can be calculated.

**Evaluation.** For evaluating the model, two different laser intensity profiles are examined. First, the Gaussian beam is considered:

$$i_{Gs}(r) = \frac{P_{abs}}{\pi r_0^2} e^{-(r/r_0)^2}, \quad (11)$$

second, the top hat profile is used:

$$i_{t.h}(r) = \frac{P_{abs}}{\pi r_0^2} \left( \frac{1}{2} - \frac{1}{\pi} \arctg \left( \frac{r - r_0}{\alpha} \right) \right), \quad (12)$$

where  $P_{abs}$  is the absorbed laser power;  $\alpha$  is the factor determining the steepness of the function.

Mathworks® Matlab (Vers. R2009a) is used to calculate the quasi-static keyhole geometry, and Simulink (Vers. 7.3) is used to calculate the dynamic behavior of the keyhole geometry and pressures. For the calculations the set of following typical parameters is used:  $P_{abs} = 900$  W;  $r_0 = 100$   $\mu$ m;  $\alpha = 1$   $\mu$ m;  $u_0 = 1$  m/min;  $d = 1$  mm;  $c_0 = 0.2$ ;  $f = 0.1$ ;  $c = 3$ ;  $v_a = 4$  m/s;  $r_{start} = 1.2$ ;  $p_{start} = 1$ . Radius  $r_{start}$  and pressure  $p_{start}$  are normalized to calculated quasi-static values of radius and pressure.

**Results of modeling. Quasi-static keyhole.**

For the Gaussian and top hat profile, the pressure gradient for the wide range of  $r_{kap}$  normalized to  $r_0$  is calculated (Figure 1).

Both curves equal zero 2 times, but only the second zero is stable. A small deviation of the first zero would lead to a collapse of the keyhole. The resulting keyhole radius obtained by the Gaussian beam is slightly smaller than that produced by the top hat distribution. Although the radius is similar, the restoring forces are different. The forces can be correlated to the pressure gradient when the radius deviation occurs. Figure 1 shows that higher pressure gradient is calculated for the top hat than for Gaussian beam.

**Dynamic behavior.** Different restoring forces in the keyhole of different incident laser beams lead to different dynamic behavior. Both radii are deviated, and the dynamic behavior is calculated by the model. Time  $t$  has to be normalized to

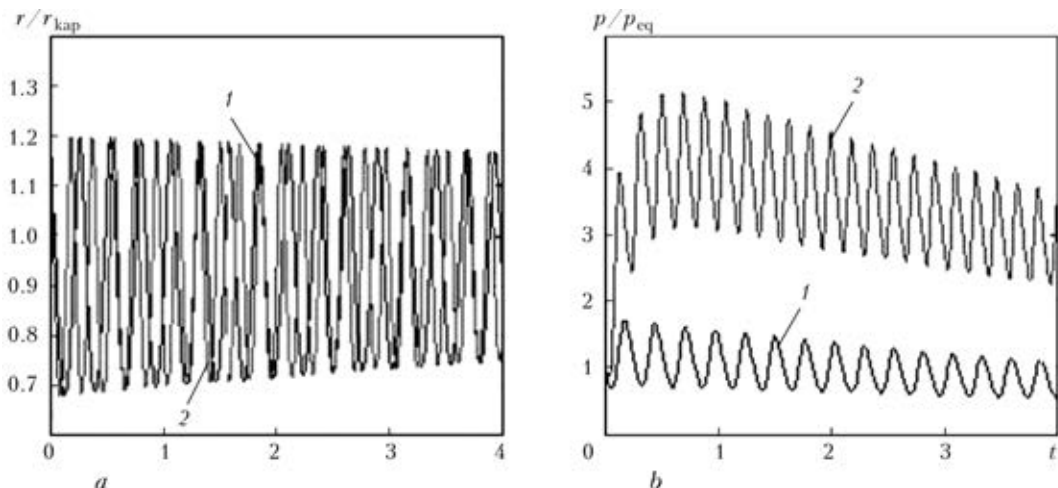


**Figure 2.** Keyhole radius (a) and pressure (b) oscillations for the Gaussian (1) and top hat (2) laser intensity distribution



$$t' = t \sqrt{\frac{m_{m.p.}}{\gamma}}. \quad (11)$$

Figure 2, *a* shows the oscillating radius around the equilibrium with different frequencies for different intensity distributions. They are found to be approximately 1.6 and 3.2 kHz for the Gaussian and top hat intensity distribution, respectively.

In Figure 2, *b* the pressure balance is shown. Pressure rises in both cases to different starting values and oscillates with different frequencies for different incident beams. Down slope of the curves is caused by the damping of the oscillation by surrounding material.

**Results.** It can be seen from the results of the modeling that different spatial laser intensity distributions have different effects on both keyhole geometry and dynamics. Impact on the keyhole pressure and also the keyhole radius is rather small. Radial dependency of the pressure gradient is much more significant. Particularly the explicit steepness of the intensity change with radius for the top hat distribution is assumed to cause a notably higher pressure gradient in the region of the stable quasi-static keyhole radius. As the pressure gradient influences the force balance, different dynamic behaviors are expected for different spatial laser intensity distributions. Fabbro et al. [18] was able to measure these pressure oscillations resulting from radius dynamics. The frequency of pressure and radius oscillations are especially influenced by different beam profiles. The higher frequency for the top hat distribution can be explained by the higher amplitude of the pressure oscillation that results in a stronger restoring force and, hence, higher velocities. This also results from the higher radial pressure gradients caused by the top hat distribution. Found frequency values are in the same range as they were experimentally measured in works [6] or [7]. It seems that the top hat distribution is more beneficial to producing stable keyhole than the Gaussian beam. Recoil pressure seems to damp the oscillations much more quickly that leads to smaller influence of the surrounding melt pool. Higher pressure gradient seems to inhibit the keyhole collapse.

### Conclusion

Using the analytical model for calculating quasi-static keyhole and dynamic behavior, the effect of different spatial laser intensities on the keyhole geometry and dynamics can be shown. Calculations of the used model show small influence of the different laser intensity profiles on keyhole geometry. Higher pressure gradient is calculated

for the top hat intensity distribution than for the Gaussian beam. For the observed radius perturbation different oscillation frequencies and amplitudes are found for the top hat and Gaussian intensity profile due to different pressure gradients. Using this model the top hat distribution seems to result in more stable keyhole.

**Acknowledgements.** The authors appreciate the funding of the Project VO 530/40-1 from DFG (Deutsche Forschungsgemeinschaft) sincerely.

1. Tsukamoto, S., Arakane, G., Kojima, K. et al. (2007) Effect of alloying elements on porosity formation in laser welding of heavy section steel plates. *IW Doc. IV-941-07*.
2. Szymanski, Z., Hoffman, J., Kurzyńska, J. (2001) Plasma plume oscillations during welding of thin metal sheets with a CW CO<sub>2</sub> laser. *J. Phys. D: Appl. Phys.*, **34**, 189–199.
3. Matsunawa, A., Kim, J.D., Katayama, S. et al. (1996) Experimental and theoretical studies on keyhole dynamics in laser welding. In: *15th ICALEO Proc.* (14–17 Oct. 1996, Detroit, USA), **81**, 58–67.
4. Berger, P., Hugel, H., Graf, T. (2011) Understanding pore formation in laser beam welding. *Physics Procedia*, **12**, 241–247.
5. Liu, L., Song, G., Liang, G. et al. (2005) Pore formation during hybrid laser-tungsten inert gas arc welding of magnesium alloy AZ31B — Mechanism and remedy. *Materials Sci. and Eng. A*, **390**, 76–80.
6. Semak, V., Hopkins, J., McCay, M. et al. (1995) Melt pool dynamics during laser welding. *J. Phys. D: Appl. Phys.*, **28**, 2443–2450.
7. Klassen, M. (2000) *Prozessdynamik und resultierende Prozessinstabilitäten beim Laserstrahlschweißen von Aluminiumlegierungen*: PhD thesis, University of Bremen.
8. Ki, H., Mohanty, P., Mazumder, J. (2002) Modeling of laser keyhole welding. Pt I: Mathematical modeling, numerical methodology, role of recoil pressure, multiple reflections, and free surface evolution. *Metallog. and Mater. Transact.*, **33**, June.
9. Pitz, I., Otto, A., Schmidt, M. (2011) Accelerated simulation of laser beam forming by means of moving meshes. In: *IWOTE Proc.* (Bremen, April 6–7, 2011).
10. Kroos, J., Gratzke, U., Simon, G. (1993) Towards a self-consistent model of the keyhole in penetration laser beam welding. *J. Phys. D: Appl. Phys.*, **26**, 474–480.
11. Pleteit, H. (2001) *Analyse und Modellierung der Keyhole-Dynamik beim Laserstrahlschweißen von Aluminiumlegierungen*: PhD thesis, University of Bremen.
12. Kaplan, F. (2011) Influence of the beam profile formulation when modeling fiber-guided laser welding. *J. Laser Appl.*, **23**(4), Nov.
13. Marten, O., Wolf, S., Hansel, K. et al. (2010) Qualifizierung von Fokussier- und Abbildungssystemen für die industrielle Laserbearbeitung mit brillanten Strahlquellen im Multikilowattbereich. In: *Laser-Anwenderforum Proc.* (Bremen, 24–25 Nov., 2010).
14. Khan, M., Romoli, L., Dini, G. et al. (2011) A simplified energy-based model for laser welding of ferritic stainless steels in overlap configurations. *CIRP Annals E*, **60**(1), 215.
15. Schmidt, M., Otto, A., Kageler, C. et al. (2008) Analysis of YAG laser lap-welding of zinc coated steel sheets. *Ibid.*, **57**(1), 213.
16. Hugel, H., Graf, T. (2009) *Laser in der Fertigung: Strahlquellen, Systeme, Fertigungsverfahren*. Stuttgart: Vieweg+Teubner.
17. Klein, T., Vicanek, M., Kroos, J. et al. (1994) Oscillation of the keyhole in penetration laser beam welding. *J. Phys. D: Appl. Phys.*, **27**(10), 2023–2030.
18. Fabbro, R., Slimani, S., Coste, F. et al. (2005) Study of keyhole behaviour for full penetration Nd:YAG CW laser welding. *Ibid.*, **38**, 1881–1887.

Received 16.01.2013



# INFLUENCE OF WELDING PROCESSES ON THE STRUCTURE AND MECHANICAL PROPERTIES OF WELDED JOINTS OF ALUMINIUM ALLOY 1460

L.I. MARKASHOVA, A.G. POKLYATSKY and O.S. KUSHNARYOVA

E.O. Paton Electric Welding Institute, NASU

11 Bozhenko Str., 03680, Kiev, Ukraine. E-mail: office@paton.kiev.ua

An essential difference in formation of structural-phase state of weld metal of aluminium alloy 1460 at application of various technological conditions of welding is shown. In nonconsumable electrode argon-arc welding the weld metal is characterized by an essential increase of the dimensions of phase precipitates in inner grain bulk, formation of massive extended eutectics of intergranular type, as well as a pronounced coarsening of granular structure, that is related to active development of the processes of collective recrystallization under the impact of temperature mode of welding. Structural-phase state of weld metal under the conditions of friction stir welding is characterized by a more marked dispersion of phase precipitates and their uniform distribution, as well as grain refinement as a result of dynamic recrystallization, due to intensive impact of deformation processes localized in the welding zone. 11 Ref., 6 Figures.

**Keywords:** *aluminium alloy 1460, nonconsumable electrode argon-arc welding, friction stir welding, phase precipitates, dislocation strengthening, strength characteristics*

Engineering demand for various materials is determined, as a rule, by the possibility of providing the required set of service characteristics of metals and alloys of a certain class, as well as their welded joints. This is particularly true for super-light materials, including Al-Li alloys, used in aircraft and aerospace engineering, where it is necessary to guarantee not only a high adaptability to fabrication, but also the required level of strength, ductility and crack resistance under complex service conditions, also at cryogenic and elevated temperatures [1, 2]. Considering that practically all the properties of any materials are determined mainly by their structural-phase state that undergoes essential changes under different conditions of thermodeformational impact, it is rational to study the most significant structural components formed in the welded joint metal under the influence of the used technological conditions. It is particularly urgent for welded joints of complex-alloyed aluminium alloys, which are characterized by an abrupt change of not only the structures, but also phase precipitates (PP) during various technological operations, also under the impact of welding processes.

In addition, at selection of the most optimum processes of aluminium alloy welding it is believed to be interesting to assess the role of the main structural components (PP, dislocation

density, substructures) in variation of welded joint strength and crack resistance that is exactly the objective of this work.

**Material and procedures.** In this work welded joints of sheet (rolled) high-strength Al-Li alloy 1460 2 mm thick were studied with application of two welding processes. The first process is automatic nonconsumable electrode argon-arc (TIG) welding at the speed of 20 m/h in MW-450 system (Fronius, Austria) at 140 A current, using Sv1201 welding wire as filler material. The second process is friction stir welding (FSW) performed in the laboratory unit designed at PWI. In the last case a special tool with a conical tip and edge of 12 mm diameter was used to produce butt joints, its rotation speed being 1420 rpm, and linear speed of its displacement along the butt was 14 m/h. Samples for research performance were prepared from the base metal and weld metal of joints.

Basic experimental information about the nature of the main structural components, having a considerable influence on service properties of welded joints, particularly, structural-phase transformations, which occur at the change of welding processes, was obtained with application of optical and transmission microdiffraction electronic microscopy (JEOL JEM-200CX) at accelerating voltage of 200 kV. Thin foils for transmission studies were made by a two-step method — preliminary electric polishing with subsequent multiple ion thinning by ionized flows of argon in a specially developed unit [3]. The latter allowed not only widening the inves-

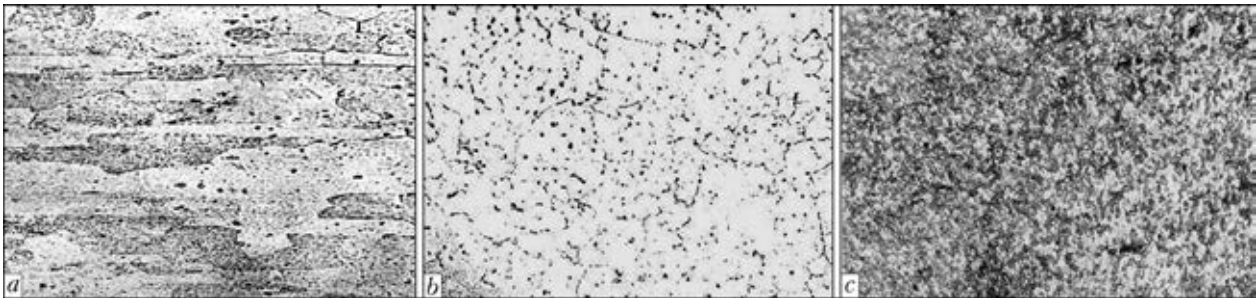


**Figure 1.** Microstructures ( $\times 400$ ) of base metal of 1460 alloy (*a*) and welds made by TIG welding (*b*) and FSW (*c*)

tigation fields (increasing the statistics), but also making all the structural-phase components of analyzed material «transparent» for the electrons.

**Investigation results.** The structure, as well as fine structure of base metal and welds of welded joints of high-strength Al–Li alloy 1460 made by TIG welding and FSW was studied.

**Base metal.** As shown by optical and electron microscopy investigations, base metal of 1460 alloy is characterized by a structure with grain size  $d_{gr} = 10\text{--}40\ \mu\text{m}$  (Figure 1, *a*), high (of the order of  $1\text{--}3 \cdot 10^{11}\ \text{cm}^{-2}$ ) and relatively uniform (along certain directions) dislocation density  $\rho$  (Figure 2).

Here formation of a more fine-grained cellular structure (Figure 2, *a, c*) of dimensions  $d_c \sim 0.15\text{--}0.40\ \mu\text{m}$  and substructure of dimensions  $d_s$  in the range of  $0.7\text{--}3.2\ \mu\text{m}$  (Figure 2, *d*) is observed in some base metal grains. Obtained photos reveal the orientation of structural components (grains, subgrains) with different dislocation density that is characteristic for band structures forming under the conditions of oriented deformation (for instance, rolling). As regards PP, in the base metal PP of Al–Li, Al–Cu and similar types are relatively uniformly distributed both in the inner volumes and along matrix grain boundaries, but do not have any

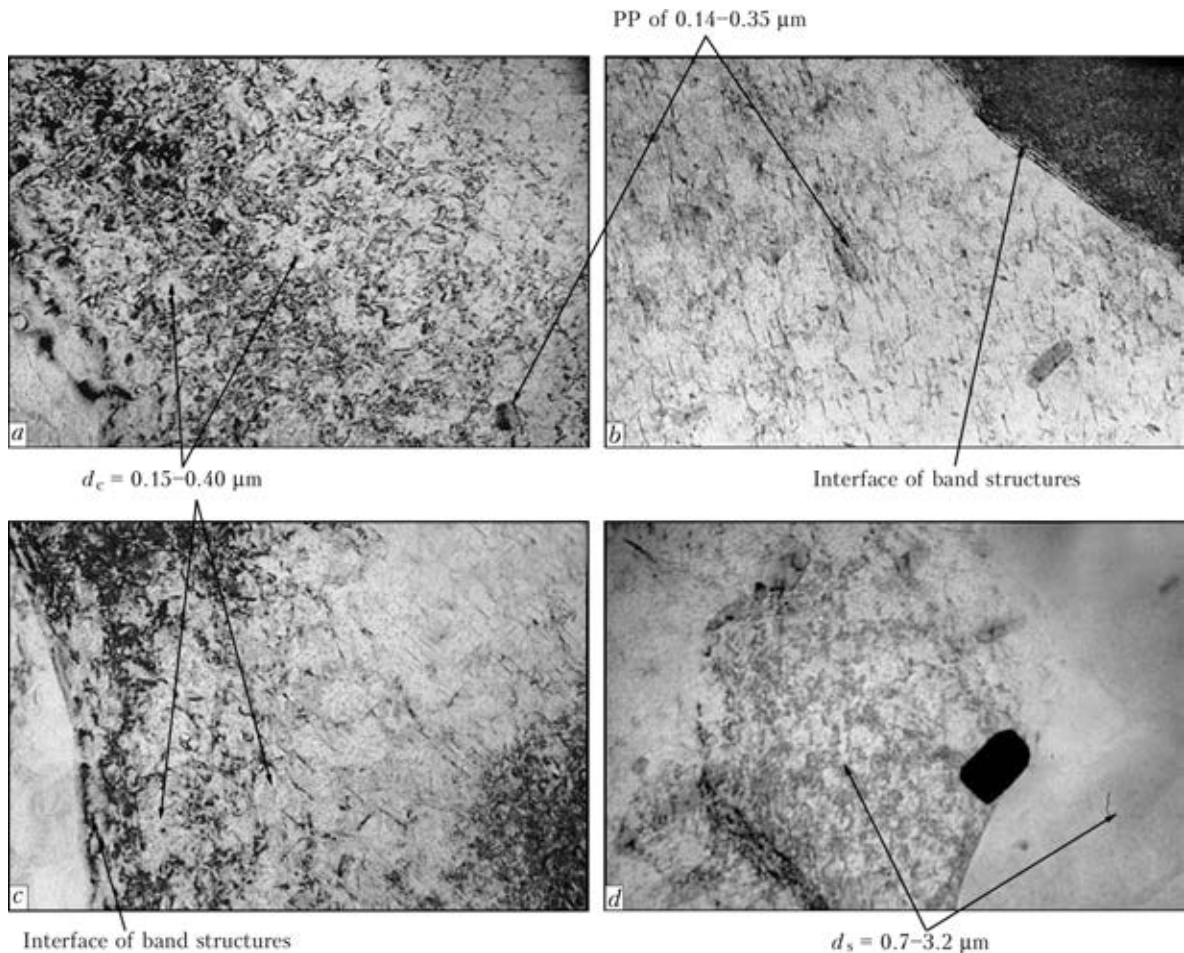


**Figure 2.** Microstructures of base metal of aluminium alloy 1460: *a, b* – distribution of dislocations and PP in inner grain volumes (*a* –  $\times 20000$ , *b* –  $\times 37000$ ); *c, d* – same along grain boundaries (*c, d* –  $\times 30000$ )



clearcut orientation. Dimensions of such PP are equal to approximately 0.14–0.35  $\mu\text{m}$  (see Figure 2, *a, b*).

*Structural-phase state of weld metal in TIG welding.* The structure, as well as fine structure of weld metal of high-strength Al–Li alloy 1460 after TIG welding is characterized by lowering of dislocation density by two orders of magnitude to  $\rho \sim 2\text{--}6 \cdot 10^9 \text{ cm}^{-2}$  (Figure 3), compared to the level of density in the base metal. In addition, rectilinearity of individual dislocations at their uniform distribution, absence of dislocation clusters, and overall rather considerable coarsening of the structure (by almost 2 times) (see Figure 1, *b*) is indicative not only of active development of the processes of collective solidification (through migration of primary grain boundaries), but also of equilibrium of coarse-grained structure of weld metal, forming under the conditions of fusion welding.

A feature of the structure of metal of welds made by TIG welding also is the nature of PP, their dimensions and distribution in different weld zones. A characteristic feature of phase formation under TIG welding conditions is formation of two PP types. With the first type PP are formed along grain boundaries (phases of inter-

granular type), and they are eutectic formations of thickness up to  $\delta \sim 0.2\text{--}0.5 \mu\text{m}$  at their considerable extent (approximately 2.0–2.5  $\mu\text{m}$ ) (Figure 3, *a, b*). The second type of PP are phases of intragranular type (Figure 3, *c, d*), which are characterized by a globular shape and large dimensions (approximately 6 times larger than those in the base metal). In addition, the volume fraction of such intragranular PP is much smaller compared to volume fraction of those in the base (initial) metal.

*Structural-phase state of weld metal in FSW.* It is found that the metal of welds of Al–Li alloy 1460 is characterized by distinct features of the main structural components, namely granular, subgranular, dislocation and phase. So, unlike the essential coarsening of the grains by the mechanism of collective recrystallization, characteristic for the conditions of fusion welding, structural transformations of another type are observed in the metal of FSW welds, namely considerable structure refinement (see Figure 1, *c*), associated with actively running processes of dynamic recrystallization, i.e. recrystallization by the nucleation mechanism. Total dislocation density increases up to  $\rho \sim 3\text{--}6 \cdot 10^{10} \text{ cm}^{-2}$  that is by an order of magnitude higher than bulk dis-

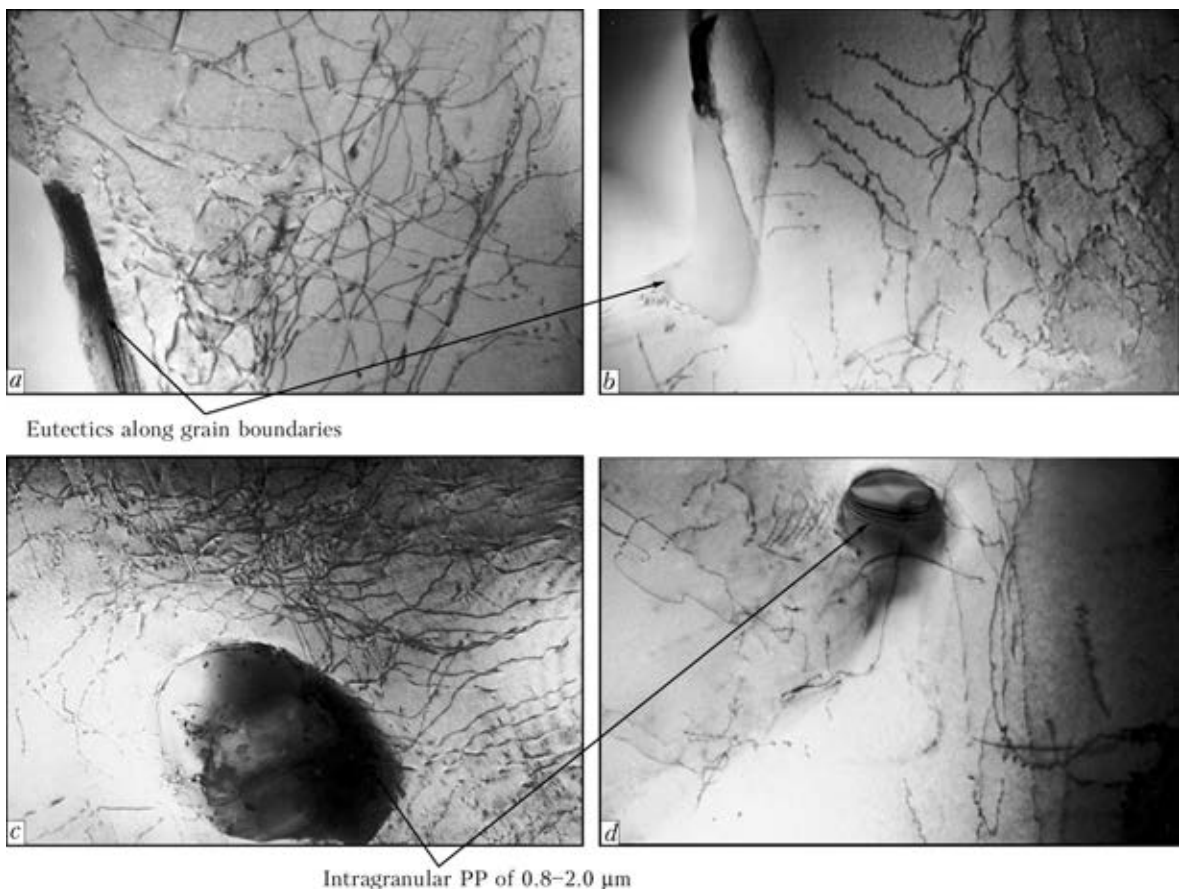


**Figure 3.** Microstructures of weld metal of alloy 1460 made by TIG welding: *a, b* – extended grain boundary eutectics (*a* –  $\times 30000$ ; *b* –  $\times 20000$ ); *c, d* – PP in inner grain volumes (*c* –  $\times 20000$ , *d* –  $\times 30000$ )

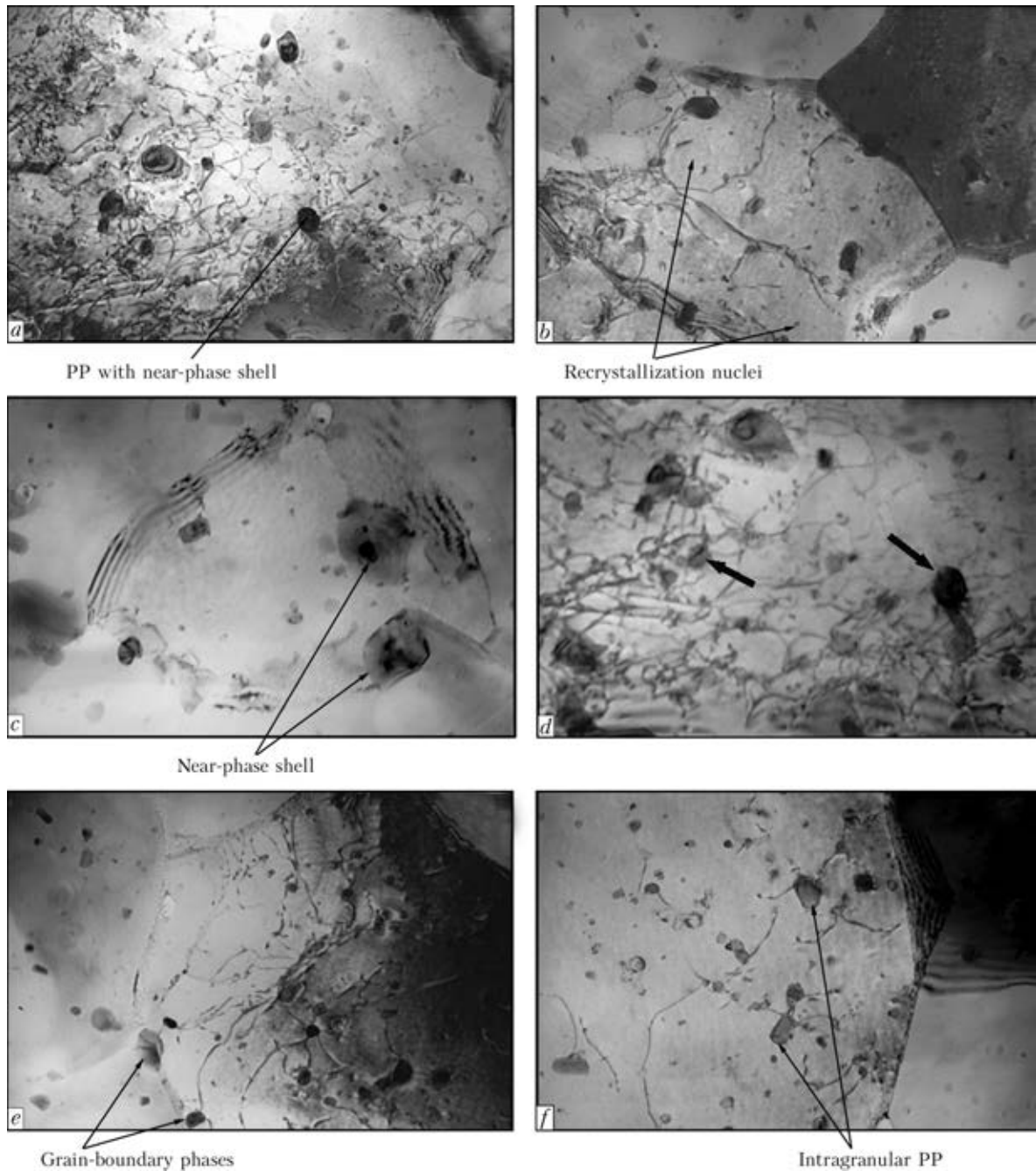


**Figure 4.** Microstructures of weld metal of 1460 alloy made by FSW: *a, d* – dislocation distribution; *b, c, f* – PP distribution in grain bulk; *e* – same, but in grain-boundary zones of weld metal (*a, c, d, f* –  $\times 30000$ ; *b, e* –  $\times 20000$ )

location density in the metal of welds in fusion welding (Figure 4, *a*). Increase of intragranular dislocation density is accompanied by active redistribution of dislocations, that is indicated by formation of substructural elements – blocks, fragments, etc. (Figure 4, *b*).

Apparently, structure refinement and activation of dislocation redistribution under FSW conditions are due to intensive deformation of weld metal heated up to plastic state and prevalence of deformation-activated processes in structural changes (dynamic recrystallization) over thermally activated processes (collective recrystallization).

The features of structural state of weld metal obtained in the solid phase by FSW (compared to metal of welds made by TIG welding) are a considerable (by 2–5 times) refinement of PP (dimensions of this PP type are in the ranges of 0.06–0.40  $\mu\text{m}$ ) and considerable increase of their quantity at uniform distribution, occurring in all the zones of weld metal – both in intragranular and in grain-boundary volumes (see Figure 4). The latter is, apparently, related to breaking up of intravolume and grain-boundary eutectic coarse phase, characteristic for weld metal obtained by TIG welding. It should be noted that the majority of PP forming in the weld metal

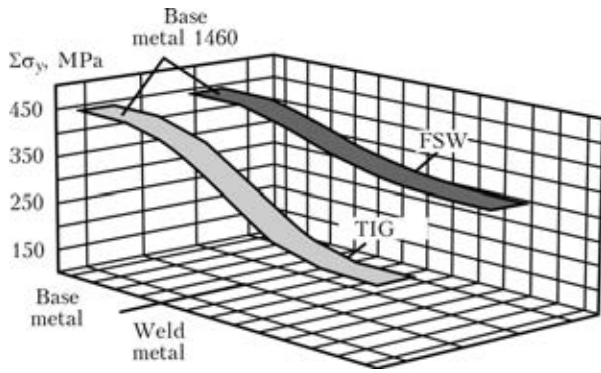


**Figure 5.** Total integral value of yield limit  $\Sigma\sigma_y$  of aluminium alloy 1460 in different zones of the joint (base metal and metal of welds made by TIG welding and FSW)

under FSW conditions are surrounded by a near-phase shell (see Figure 4, c), that is indicative of intensive alloying of the local near-phase space in matrix grain bulk.

**Analytical assessment of the change of welded joint properties.** Proceeding from comprehensive experimental investigations of structural-phase components forming in the metal under different thermodeformational conditions, analytical assessment of their specific (differentiated) contribution to the change of general (integrated) values of such a mechanical characteristic as yield limit  $\sigma_y$  of base and weld metal after cardinally differing welding processes, namely TIG (argon-arc) welding and solid-phase FSW was performed.

Analytical assessments of  $\sigma_y$  were performed by Archard equation, including known Hall-Petch, Orowan and other dependencies [4–11]:

$$\Sigma\sigma_y = \Delta\sigma_0 + \Delta\sigma_{s,s} + \Delta\sigma_{gr} + \Delta\sigma_s + \Delta\sigma_d + \Delta\sigma_{d,s}$$

where  $\Delta\sigma_0$  is the metal lattice resistance to free dislocation motion (lattice friction stress or Peierls–Nabarro stress);  $\Delta\sigma_{s,s}$  is the solid solution strengthening by alloying elements and impurities (solid solution strengthening);  $\Delta\sigma_{gr}$ ,  $\Delta\sigma_s$  is the strengthening due to the change of grain and subgrain size (Hall–Petch dependencies, granular and subgranular strengthening);  $\Delta\sigma_d$  is the dislocation strengthening due to interdislocation interaction;  $\Delta\sigma_{d,s}$  is the strengthening due to dispersed particles by Orowan (dispersion strengthening).

General value of yield limit  $\Sigma\sigma_y$  is given in Figure 5, specific contribution  $\Delta\sigma_y$  of various structural components to the above-mentioned characteristic of base metal and weld metal, produced by various welding processes, is shown in Figure 6.

It is found that in the base metal of 1460 alloy the most significant contribution among the structural-phase components determining the yield limit values, should be made by: dislocation component ( $\Delta\sigma_d = 127$  MPa), subgrain ( $\Delta\sigma_s = 151$  MPa) and grain strengthening ( $\Delta\sigma_{gr} = 62$  MPa) (Figure 6, a), that, taken as percentage of the general value of yield limit, is equal to 14, 28 and 33 %, respectively (Figure 6, b).

In fusion welding the contribution of the above components decreases significantly, as dislocation density in the metal of such welds drops abruptly, whereas grain size increases considerably, resulting in the assessed characteristics of

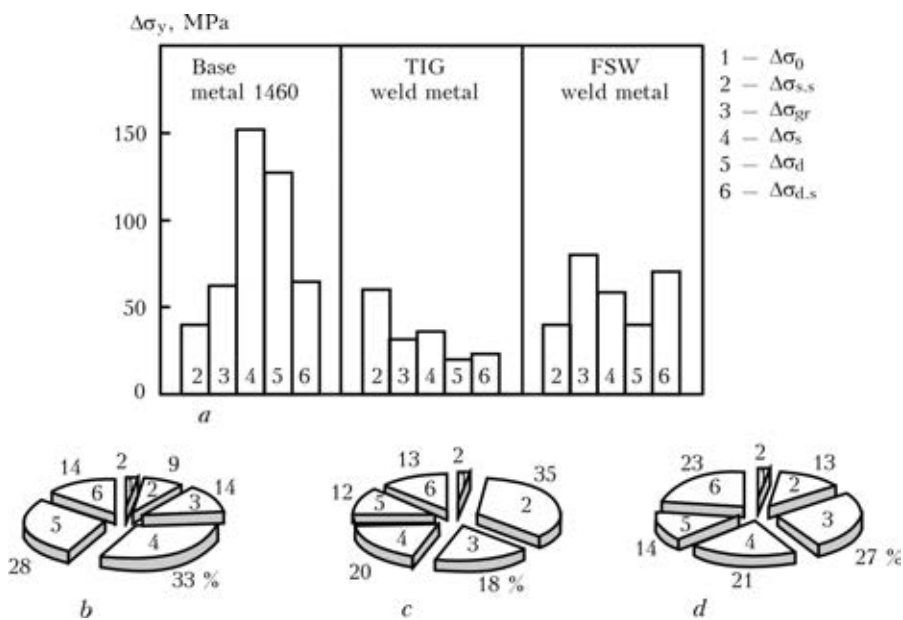


**Figure 6.** Histogram of differentiated contribution of structural-phase components of  $\Delta\sigma_y$  into calculated value of yield limit (a), and sector diagrams (b–d) of structural contribution (solid solution, grain, subgrain, dislocation, dispersion) into the total value of yield limit  $\Sigma\sigma_y$  in base metal (b) and metal of welds made by TIG welding (c) and FSW (d)



weld metal decreasing by 2–5 times in fusion welding compared to base metal, namely to the following values:  $\Delta\sigma_d = 20$ ,  $\Delta\sigma_s = 36$ ,  $\Delta\sigma_{gr} = 31$  MPa. Percentagewise, the contribution of the respective structures is equal to 12, 20 and 18 %, respectively (Figure 6, a, c). Here, solid solution strengthening  $\Delta\sigma_{s,s}$  in the above type of weld metal is equal approximately to 60 MPa, i.e. 35 %.

In welds produced in the solid phase by FSW, compared to welds made by fusion welding, a significant increase of the yield limit values will be promoted by: significant refinement of the structure ( $\Delta\sigma_{gr} = 80$  MPa), formation of substructure ( $\Delta\sigma_s = 58$  MPa), increase of dislocation density (dislocation strengthening  $\Delta\sigma_d = 40$  MPa) and significant increase of bulk density of dispersed and uniformly distributed PP ( $\Delta\sigma_{d,s} = 70$  MPa), that percentagewise in the general (integral) value of  $\Sigma\sigma_y$  is equal to, respectively, 27, 21, 14 and 23 % (Figure 6, a, d). Under FSW conditions this allows leveling the gradients of strength characteristics (in this case – the yield limit) between the base, i.e. metal welded and weld metal to values of the order of 156 MPa that is much less than the gradient (of the order of 285 MPa) usually found in fusion welding.

## Conclusions

1. Integrated methods of investigation of welded joints of complex-alloyed aluminium alloy 1460 were applied to determine the changes of key structural-phase components, affecting the mechanical characteristics of welded joints at the change of conditions of technological modes of welding processes – from TIG welding to FSW (solid phase welding).

2. Under the conditions of fusion welding, the metal of welds is characterized by a coarse-grained structure, lowering of total bulk density of dislocations, formation of globular intragranular and extended intergranular PP of eutectic type that is due to prevalence of thermal activation of relaxation processes.

3. Weld metal structure in FSW features an abrupt refinement of the grain that is associated with activation of the nucleation processes, increase of the total dislocation density, as well as

significant PP dispersion at their uniform distribution in intragranular and grain boundary volumes, that is ensured by prevalence of thermodeformational conditions at formation of structural-phase state of weld metal.

4. Analytical assessment of the general (integral  $\Sigma\sigma_y$ ) value of the yield limit showed that in the metal of welds made by FSW a total increase of  $\Sigma\sigma_y \sim 40$  % is observed due to refinement of grain ( $\Delta\sigma_{gr} \leq 27$  %) and subgrain ( $\Delta\sigma_s \leq 21$  %) structures and PP dispersion ( $\Delta\sigma_{d,s} \leq 23$  %), that considerably reduces the gradient of mechanical characteristics between the base metal and weld metal. Contrarily, lowering of yield limit value  $\Sigma\sigma_y$  of weld metal in fusion welding, which is due to coarsening of the grain structure and lowering of general density of dislocations promotes at increase of the gradient by the indices of yield limit between the base metal and metal of welds of the welded joint.

1. Fridlyander, I.N. (2000) Aluminium alloys in flying vehicles in the periods from 1970 to 1999 and from 2000 to 2015. In: *Proc. of 5th Session of Sci. Council on Advanced Materials of IAAS on Problems of Current Materials Science*. Kiev: Naukova Dumka.
2. Fridlyander, I.N. (1998) Aluminium alloys in aeronautical engineering. In: *Proc. of 3rd Session of Sci. Council on Advanced Materials of IAAS on Problems of Current Materials Science*. Kiev: Naukova Dumka.
3. Darovsky, Yu.F., Markashova, L.I., Abramov, N.P. et al. (1985) Procedure of thinning of dissimilar welded joint specimens for electron microscopic examinations. *Automatich. Svarka*, **12**, 60.
4. Suzuki, H. (1967) *About yield strength of polycrystalline metals and alloys*. Moscow: Metallurgiya, 255–260.
5. Ashby, M.F. (1972) On Orowan stress. In: *Physics of strength and ductility*. Moscow: Metallurgiya.
6. Goldshtejn, M.I., Litvinov, V.S., Bronfin, B.M. (1986) *Physics of metals of high-strength alloys*. Moscow: Metallurgiya.
7. Conrad, H. (1973) Model of deformation strengthening to explain the grain size influence on metal yield stress. In: *Ultrafine grain in metals*. Ed. by L.K. Gordienko. Moscow: Metallurgiya, 206–219.
8. Armstrong, R.V. (1973) Strength properties of ultrafine grain metals. *Ibid.*, 11–40.
9. Petch, N.J. (1953) The cleavage strength of polycrystalline. *J. Iron and Steel Inst.*, **173**(1), 25–28.
10. Orowan, E. (1954) *Dislocation in metals*. New York: AIME.
11. Ashby, M.F. (1983) Mechanisms of deformation and fracture. *Adv. Appl. Mech.*, **23**, 117–177.

Received 15.01.2013



# MATHEMATICAL MODELLING OF STRUCTURAL TRANSFORMATIONS IN HAZ OF TITANIUM ALLOY VT23 DURING TIG WELDING\*

S.V. AKHONIN, V.Yu. BELOUS, A.F. MUZHICHENKO and R.V. SELIN

E.O. Paton Electric Welding Institute, NASU

11 Bozhenko Str., 03680, Kiev, Ukraine. E-mail: office@paton.kiev.ua

Issues of weldability of multi-component titanium alloys are covered in many studies. As experimental investigations are time- and labour-consuming, it seems reasonable to use mathematical methods for evaluation of the effect of parameters of the welding thermal cycle on structural transformations occurring in the HAZ. In the present study the effect of the thermal cycle of argon-arc welding on shape and size of the weld, length of HAZ and kinetics of structural transformations in the HAZ metal is investigated by the mathematical modelling methods by an example of TIG welding of high-strength titanium alloy VT23. Calculations using the 3D mathematical model of the thermal processes occurring in titanium during welding, based on the differential thermal conductivity equation, were carried out by employing the finite element method application package. The calculations made it possible to determine size and shape of the weld and HAZ, in which the polymorphic transformations take place to form the  $\alpha$ -,  $\alpha'$ - and  $\beta$ -phases. The calculations showed that the  $\alpha'$ -phase may form in the weld metal at the highest cooling rates. The low-ductility  $\omega$ -phase does not form at the investigated process parameters and welding speeds of 10 m/h because of comparatively low cooling rates within the 500–600 °C temperature range. The results obtained can be applied in development of the technology for welding of advanced titanium alloys. 4 Ref., 6 Figures.

**Keywords:** TIG welding, mathematical modelling, titanium alloy, cooling rate, polymorphic transformations

Tungsten electrode arc welding in the atmosphere of inert gases (TIG), such as argon and helium, is still the most common, relatively simple and versatile method for fabrication of structures from titanium alloy. It makes it possible to perform welding in various spatial positions and sufficiently quickly readjust the equipment when type of the joint and thickness of the metal

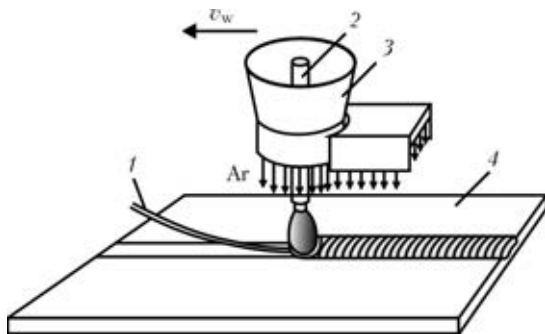


**Figure 1.** Flow diagram of the process of TIG welding of titanium: 1 – filler wire; 2 – tungsten electrode; 3 – protecting nozzle; 4 – workpiece

welded are changed. One of the ways of widening the technological capabilities of narrow-gap TIG welding of heavy sections and cladding operations is to use the external controlling magnetic field for deflection of the welding arc [1]. Experimental investigations of the thermal processes occurring in the welded joint during welding of titanium by the magnetically controlled arc are labour-consuming and costly because of a large quantity of parameters of the welding process, especially in a case of welding of high-strength titanium alloys. Therefore, the authors performed analytical investigation of thermal conditions in welding of plates of titanium alloy VT23 by mathematical modelling of the process.

Modelling allowed investigating the effect of such process parameters as welding speed and heat input on shape of the base metal penetration zone and HAZ, on values of the maximal cooling rates in different regions of the HAZ metal, and temperature gradients in cooling [2].

Flow diagram of the process of cladding of titanium parts is shown in Figure 1.

Calculations of the thermal conditions accompanying the process of melting of the metal surface were made by using the mathematical model based on the differential thermal conductivity equation in the 3D Cartesian coordinate system.

The finite element 3D model of the thermal processes of square-groove cladding of titanium

\*The article is based on the presentation made at the 6th International Conference «Mathematical Modelling and Information Technologies in Welding and Related Processes» (29 May–1 June, 2012, Katsiveli, Ukraine).

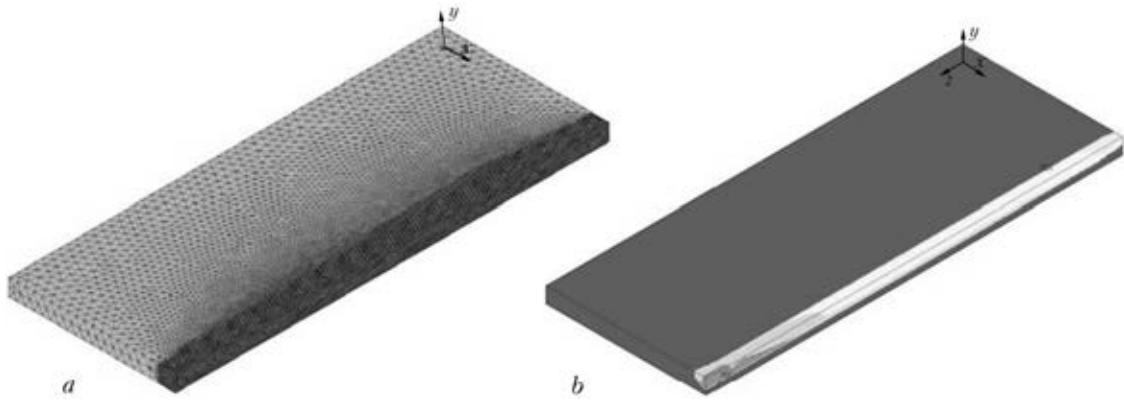


**Figure 2.** Finite element model used in calculations (a), and result of calculations of thermal fields (b)

plates with a moving heat source is shown in Figure 2, a. Here the results are given for half of the welded joint.

The following parameters were selected as the initial data for the calculations:  $v_w = 10$  m/h,  $I_w = 220$  A,  $U_a = 12$  V.

The calculated thermal fields (Figure 2, b) in a clad part were obtained with allowance for the above initial and boundary conditions by using the ANSYS software module. The calculation results were used to plot the isothermal lines of maximal temperatures, from which geometry and size of the penetration zone, HAZ and polymorphic transformation zone (Figure 3, a), as well as distribution of maximal cooling rates and temperature gradients in cross section of the welded joint were determined. Comparison of the calculation results on shape of the penetration zone with the experimental data showed the satisfactory agreement between them (see Figure 3).

Welded joints on high-strength titanium alloy VT23 are sensitive to the cooling rate [3]. The

results obtained allow evaluating the probable phase composition of the cooling weld and HAZ metals. The diagram (Figure 4) shows the temperature of beginning of the  $\beta \rightarrow \alpha''$  martensitic transformation (560 °C), the lines of beginning and end of high-temperature diffusion decomposition of the  $\beta$ -phase, and the line of beginning of precipitation of the low-temperature  $\alpha_1$ -phase. The line of the  $\beta \rightarrow \omega$  transformation is marked in a cooling rate range of 59–11 °C/s.

Analysis of the obtained calculation data showed that in cooling from a temperature of 1667 to 890 °C the highest cooling rates are noted in the weld metal, where they may amount to 400 °C/s. In the fusion zone the cooling rates may reach 130 °C/s, and in the major part of the HAZ metal the cooling rate is not in excess of 30 °C/s.

Upon reaching a temperature of 900 °C, the cooling rate in the weld decreases to 130 °C/s, and that of the region corresponding to the

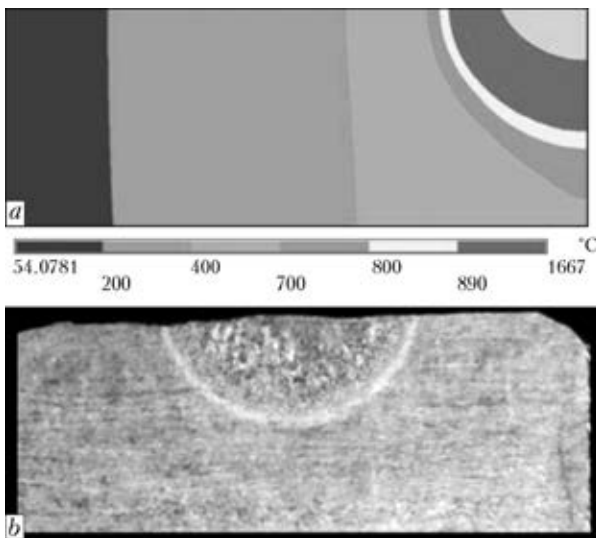


**Figure 3.** Isothermal lines of maximal temperatures obtained as a result of calculation (shown is half of the welded joint) (a), and transverse macrosection of cladding using tungsten electrode (b)

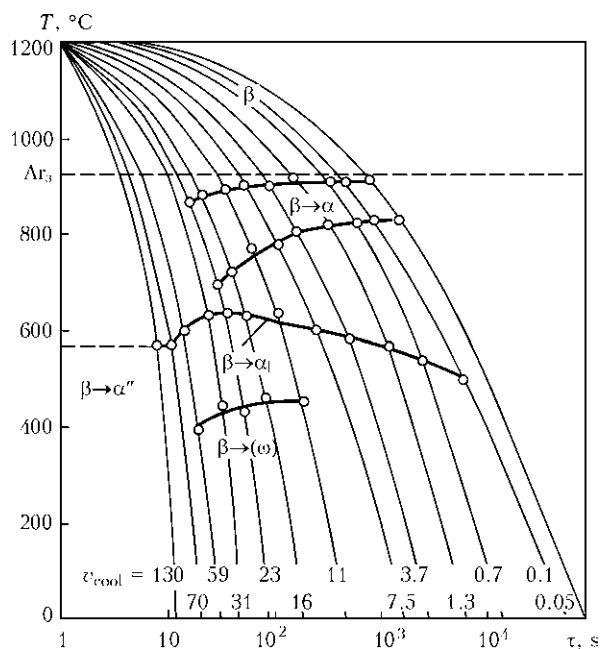


**Figure 4.** Diagram of anisotropic transformations of titanium alloy VT23 [3]

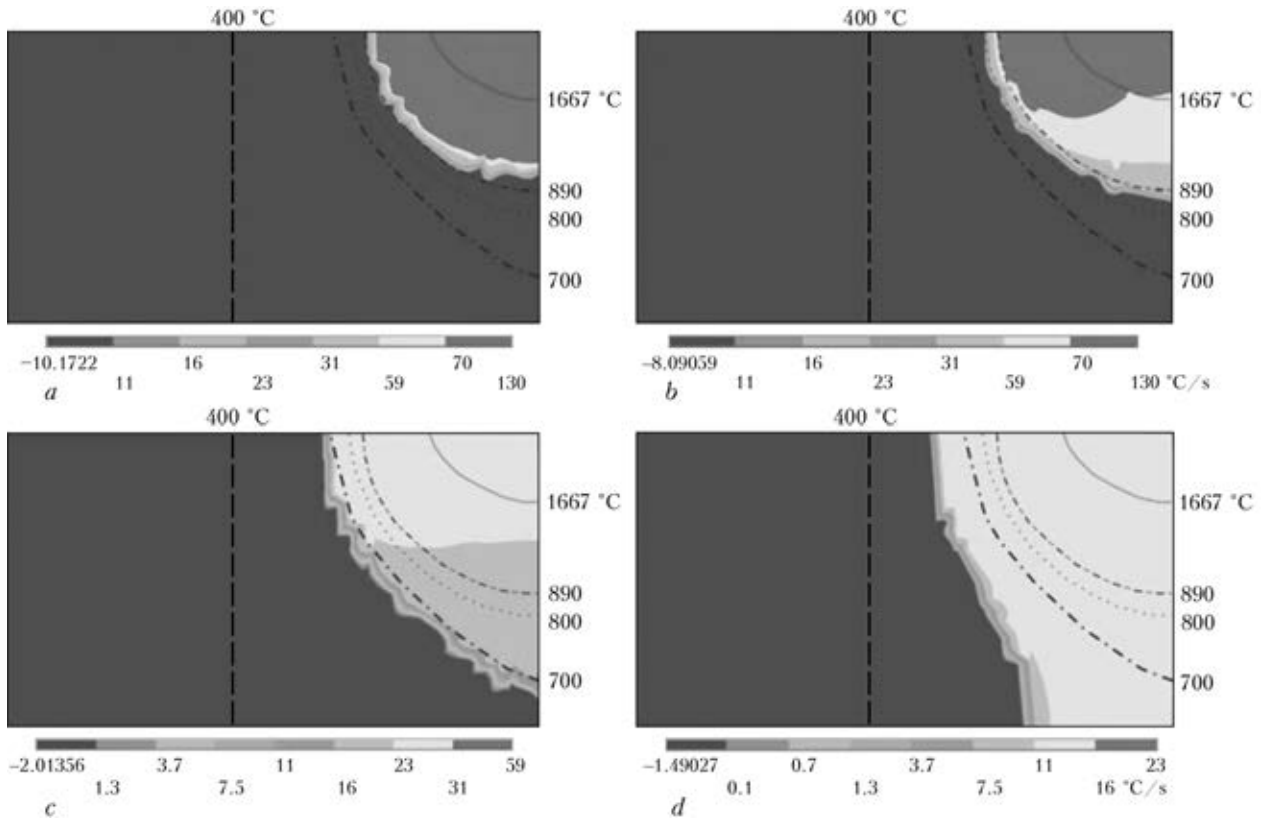


**Figure 5.** Distribution of maximal cooling rates across the welded joint on titanium alloy VT23 in temperature range of 1000–890 (a), 890–800 (b), 700–600 (c) and 600–500 (d) °C at  $v_w = 10$  m/h,  $I_w = 220$  A and  $U_a = 12$  V (dashed lines – characteristic isothermal line of maximal temperatures)

coarse-grained zone increases to 70 °C/s. In cooling from 890 to 800 °C, the cooling rate in the weld is 70–130 °C/s. The  $\alpha''$ -phase laminae form in this case. In cooling in this temperature range (890–800 °C) the upper part of the welded joint metal has the highest cooling rate. Therefore, the largest size of precipitates of the high-temperature  $\alpha$ -phase might be expected in this zone (Figure 5, a, b). It should be noted that the maximal temperature gradient at a temperature of 890 °C is in the HAZ metal, rather than in the upper part of the cooling weld metal (Figure 6). In a temperature range of 700–600 °C the cooling rate in the upper part of the welded joint metal is still highest and amounts to 23–31 °C/s (Figure 5, c), while in cooling from 600 to 500 °C the cooling rate in general becomes levelled

across the HAZ metal and equals 11–16 °C/s. In this case, decomposition of the  $\beta$ -phase enriched with  $\beta$ -stabilisers occurs to precipitate the so-called low-temperature  $\alpha_1$ -phase [4], which differs from the high-temperature one in that it contains more alloying elements and is much finer. Low ductility of the  $\alpha_1$ -phase is responsible for a substantial decrease in ductility of the welded joints on alloy VT23 made at the above process parameters.

Cooling in a temperature range of 500–400 °C/s takes place against a background of levelling of the cooling rates in the weld and HAZ metals. In this case the cooling rates are 3.7–7.5 °C/s, being almost uniform over the entire HAZ metal. No decomposition of the  $\beta$ -phase to form the  $\omega$ -phase occurs in this temperature

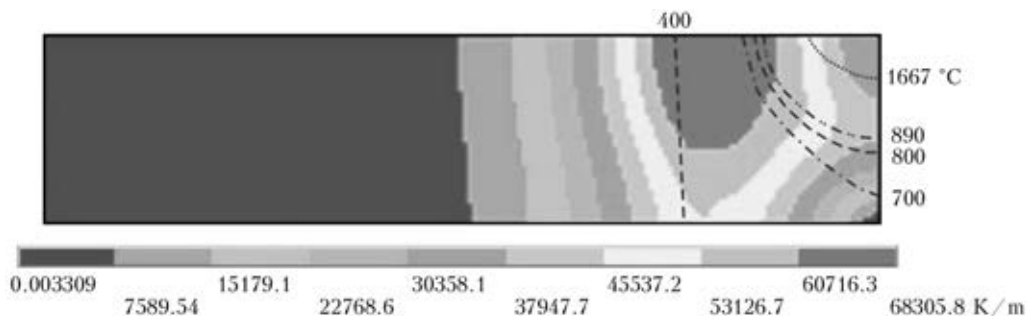


**Figure 6.** Distribution of temperature gradients across the welded joint on titanium alloy VT23 at 890 °C



range because of the comparatively low cooling rates.

No cooling rates below 0.05 °C/s were detected in the welded joint. Therefore, the weld and HAZ metals consist of a mixture of the  $\alpha$ - and  $\beta$ -phases, their proportion being different for different regions of the welded joint.

### Conclusions

1. The mathematical model was developed to describe the thermal processes occurring in titanium during TIG welding. The model made it possible to determine size and shape of the weld and HAZ, in which the polymorphic transformations take place to form the  $\alpha$ -,  $\alpha'$ - and  $\beta$ -phases.

2. The calculations showed that the  $\alpha'$ -phase may form in the weld metal having the highest cooling rates.

3. The low-ductility  $\omega$ -phase does not form in the weld or HAZ metal of the welded joints on titanium alloy VT23 made at the above process

parameters because of comparatively low cooling rates in a temperature range of 500–600 °C.

4. Decrease in ductility of the welded joints on titanium alloy VT23 is related to the  $\alpha_1$ -phase, which forms in the  $\beta$ -solid solution regions enriched with alloying elements in cooling at a rate of 70–0.1 °C/s.

1. Gurevich, S.M., Zamkov, V.N., Blashchuk, V.E. et al. (1986) *Metallurgy and technology of welding of titanium and its alloys*. Kiev: Naukova Dumka.
2. Akhonin, S.V., Belous, V.Yu., Muzhychenko, A.F. (2009) Narrow-gap TIG welding of titanium alloys with electromagnetic redistribution of thermal energy of the arc. In: *Proc. of 4th Int. Conf. on Laser Technologies in Welding and Materials Processing* (26–29 May, 2009, Katsiveli, Crimea, Ukraine), 11–13.
3. Lyasotskaya, V.S., Lyasotsky, I.V., Meshcheryakov, V.N. et al. (1986) Phase transformations in continuous cooling in VT6ch and VT23 alloys. *Tsvet. Metallurgiya*, **2**, 88–93.
4. Lyasotskaya, V.S. (2003) *Heat treatment of titanium alloy welded joints*. Moscow: Ekomet.

Received 24.01.2013

## NEWS

### *Asynchronous Welding Generator for 315 A*

Asynchronous welding generator is designed for operation in the field in mobile welding plants as welding current source and auxiliary AC generator. Asynchronous welding generator provides:

- smooth local and remote adjustment of welding current in one range by standard electric control signal of 0–10 V;
- correction of external static and dynamic characteristics depending on the grade of applied electrodes and technological features of welding;
- one- and three-phase AC mains of 220/380 V voltage and 50 Hz frequency;
- source of reduced alternating voltage, for instance of 24 or 36 V with 50 Hz frequency.

A new ingenious control system ensuring a high welding quality at lower electrode metal spatter is applied in the

developed asynchronous welding generator. It is possible to manufacture asynchronous welding generator not only for manual arc welding, but also for other welding processes, for instance CO<sub>2</sub> welding, as well as for air-plasma cutting, without any significant additional expenses.

Asynchronous welding generators are greatly superior to traditional valve generators by a number of technical and technological characteristics. Developed asynchronous welding generators are manufactured on the base of batch-produced asynchronous electric motors of appropriate power, which is the basis of their high reliability, relative simplicity and low cost.

Return on investment period is 2 years.



# EFFECT OF SIZE OF THE GAP AND INITIAL STATE OF THE BRAZING FILLER ALLOY ON FORMATION OF STRUCTURE OF THE TITANIUM ALLOY BRAZED JOINTS

S.V. MAKSYMOVA, V.F. KHORUNOV and V.V. VORONOV

E.O. Paton Electric Welding Institute, NASU

11 Bozhenko Str., 03680, Kiev, Ukraine. E-mail: office@paton.kiev.ua

Brazing filler alloys of the Ti–Zr–Ni–Cu system in both amorphous and crystalline states are widely applied in brazing of titanium and its alloys. It is reported that brazing with amorphous filler alloys creates special conditions for formation of the joints, the issue of the effect of size of the brazing gap being neglected. This issue was investigated in this study. Special samples of titanium alloy OT4 (Ti–3Al–1.5Mn) were brazed in vacuum with the fixed variable gap by using filler alloy Ti–23Cu–12Zr–12Ni in the amorphous and crystalline states to conduct comparative metallographic examinations. It was found that microstructure and chemical composition of the phases solidifying in a wide region of the seam of the joints brazed by using amorphous filler alloy Ti–23Cu–12Zr–12Ni are similar to those of the wide seams brazed with the cast filler alloy of the same composition. Primary solid solution grains and eutectic were clearly detected in structure of the seams. In the capillary gaps the seam is a diffusion zone with common base metal grains enriched with the filler alloy components, in case of brazing using both amorphous and crystalline filler alloys. Occurrence of the diffusion processes at interface between the phases is proved by the X-ray spectral analysis results. At a concentration of zirconium in the seam equal to 16.39 wt.% its concentration at a distance of approximately 100  $\mu\text{m}$  deep into the base metal decreases to 1.22 wt.%, and at a distance of 150  $\mu\text{m}$  zirconium is not detected at all. As shown on the basis of the results of metallographic examinations and X-ray spectrum microanalysis of the titanium joints, the decisive factor in formation of microstructure of the seams is size of the brazing gap, which determines the morphological state of the seam. 8 Ref., 5 Tables, 8 Figures.

**Keywords:** titanium alloy, brazing filler alloy, gap size, joint, amorphous and crystalline state, brazed seam, microstructure

As a rule, filler alloys in both amorphous and crystalline states are widely applied in brazing of titanium alloys. The key advantage of filler alloys with the amorphous structure is that they can be produced in the form of plastic homogeneous (in chemical composition) thin strips (30–50  $\mu\text{m}$ ) even from the alloys containing brittle intermetallic or eutectic phases [1]. This allows making inserted elements of any shape, strictly proportioning the amount of a filler alloy and brazing of very thin materials (e.g. heat exchangers, where thickness of a separating plate is about 0.08 mm). Owing to a high chemical homogeneity, brazing filler alloys with the amorphous structure have narrow melting temperature ranges, this ensuring good wetting of the surfaces being brazed, reducing the probability of lacks of penetration and, hence, providing a high corrosion resistance and strength of the brazed joints [2]. Such filler alloys include alloys of the Ti–

Zr–Ni–Cu system, which are widely applied in brazing of titanium and its alloys [3–6].

The purpose of this study was to investigate the effect of size of the brazing gap on formation of structure of the titanium alloy seams by using filler alloys in the amorphous and crystalline states.

To produce the brazed joints, titanium pseudo  $\alpha$ -alloy OT4 (Ti–3Al–1.5Mn) was used as a base metal. Structure of this alloy consists of the  $\alpha$ -phase and an insignificant amount of the  $\beta$ -phase (1–5 %). It can be readily processed in the hot and cold states, and is used in the form of plates, bands and strips.

Brazing filler alloy Ti–23Cu–12Zr–12Ni was used in the amorphous (plastic strip 30  $\mu\text{m}$  thick) and crystalline (cast ingot was crushed and used in the form of lumps) states. The filler alloy was melted in a laboratory electric-arc furnace on a water-cooled bottom plate in an atmosphere of purified argon. Each ingot was remelted not less than five times to blend its chemical composition. Titanium sponge (99.9 %), zirconium iodide (99.9 %), electrolytic nickel (99.9 %) and electrolytic copper (99.9 %) were used as source ma-



**Table 1.** Chemical composition of structural components of the cast filler alloy, wt.%

Investigated region	Ti	Zr	Cu	Ni
Fine grains (dark)	76.70	8.33	9.92	5.05
Phase along boundaries (light)	53.05	14.41	18.80	13.74
Eutectic	59.48	5.78	26	8.74

terials. Chemical composition of the alloys was controlled by fluorescent X-ray spectrum analysis using spectrometer VRA-30.

Before brazing, the titanium plates (2 mm thick) were mechanically cleaned and assembled in such a way that the gap between the plates had on one side a tantalum foil 150 μm wide (to fix the maximal size of the gap), and that the capillary gap formed on the opposite side between the plates. After that they were tacked with the resistance machine using the tantalum strip.

Overlap joints with a fixed variable gap (Figure 1) were brazed for metallographic examinations.

The brazing filler alloy in the amorphous state in the form of a strip was placed between the titanium alloy plates (Figure 1, *a*), and that in the cast state in the form of separate lumps was located on the plate to be brazed near the gap (Figure 1, *b*). In heating, the filler alloy with the cast structure melted and flowed into the brazing gap due to the capillary forces. Brazing of samples was performed in the vacuum furnace at a temperature of 1000 °C, the holding time being 10 min, and the degree of vacuum in the working space being  $(2-5) \cdot 10^{-3}$  Pa. Cooling of the samples in a temperature range of 1000–600 °C was carried out at a rate of 35–40 °C/min. Metallographic examinations were conducted by using scanning electron microscope CamScan-4 (Great Britain) fitted with energy-dispersive analyser ENERGY 200 with software INCA, and JEOL JSM 840 fitted with X-ray microanalyser of the Link system with wave spectrometer Ortec.

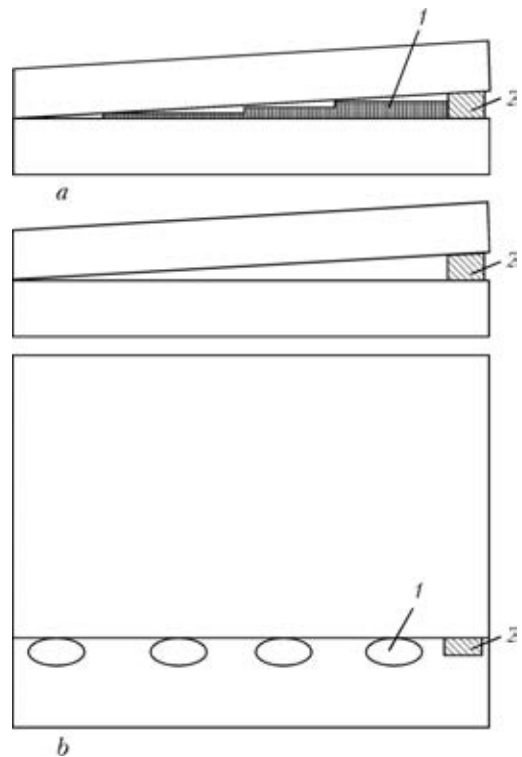


**Figure 1.** Schematics of samples for conducting metallographic examinations using filler alloy in the amorphous (*a*) and cast (*b*) states: 1 – filler alloy; 2 – inserted element for fixation of gap

Investigations of chemical heterogeneity of the rapidly quenched Ti–23Cu–12Zr–12Ni strip in the initial state prove the homogeneous distribution of the alloying elements in its width along the scanning line (Figure 2, *a, b*) [7, 8]. Structure of this alloy in the crystalline state consists of three phases (Figure 2, *c*; Table 1).

Visual examination of the brazed samples confirmed good wetting of the material being brazed, formation of smooth fillets and absence of defects. The joints brazed by using the rapidly quenched filler alloy in the amorphous state are characterised, as a rule, by formation of fillets of insignificant sizes.

At constant temperature-time parameters of the brazing process the character of solidification of the molten filler alloy in fillet regions and

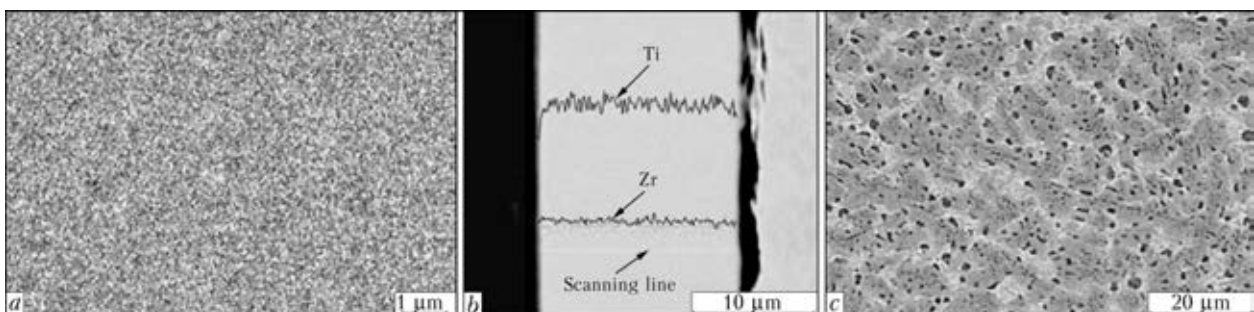


**Figure 2.** Microstructures of filler alloy in the amorphous (*a*) and crystalline (*c*) states, and character of distribution of alloying elements in the amorphous filler alloy (*b*)

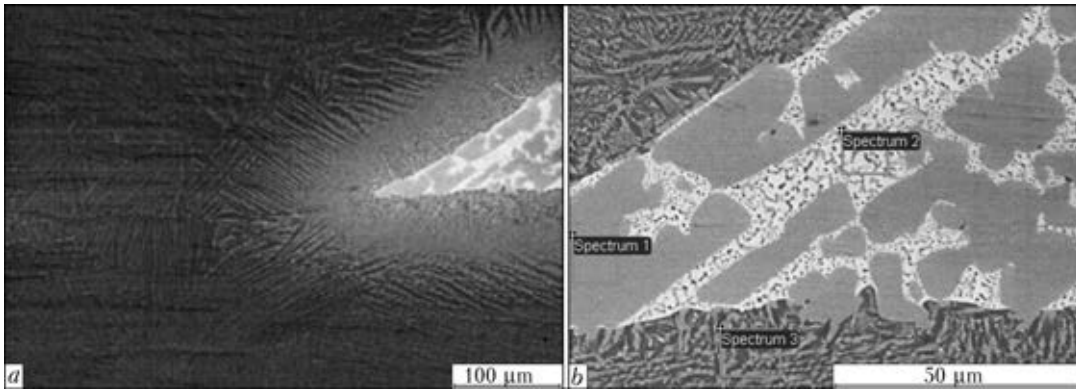


**Figure 3.** Microstructures of the reverse (*a*) and direct (*b*) fillets of the brazed joint made by using filler alloy with the crystalline structure

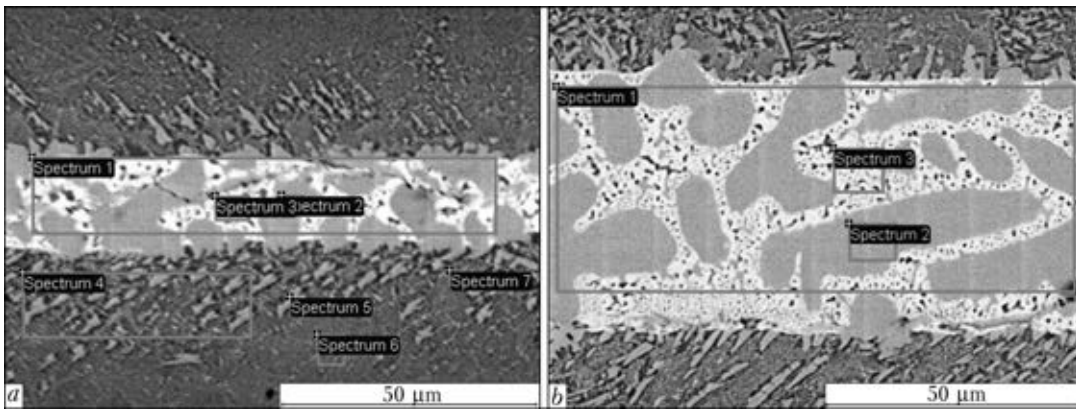


**Figure 4.** Microstructure of region of the brazed seam made by using filler alloy with the amorphous (*a*) and crystalline (*b*) structure

wide gaps, and morphological peculiarities of structure formation are close to each other.

For example, the full fillets, i.e. direct and reverse (Figure 3, *a, b*), were observed in brazing using the cast filler alloy. Metallographic examinations and investigation of chemical heterogeneity showed that the amount of structural components and their chemical composition in the fillet region and in the wide gap are practically identical (Table 2). In these regions the ratio of the amount of the molten filler alloy metal to the surface of contact with the base metal is sufficiently high, this decelerating the levelling diffusion processes. The seam metal solidifies in ac-

cordance with the main principles of solidification of cast metals and alloys.

The same structural components (Figure 4, *a*) were detected in wide-gap (40–10 μm) brazing with the rapidly quenched filler alloy in the amorphous state as in wide-gap brazing with the filler alloy in the crystalline state (Figure 4, *b*). The first to solidify was the primary phase in the form of titanium-base (54.61–54.59 wt.%) dendrites containing copper, nickel and zirconium (27.71, 7.91 and 9.49 wt.%, respectively) (spectrum 2 in Figure 4, *a, b*; Table 2). Then a lower-melting point phase, i.e. eutectic, with an increased zirconium content (23.12–24.40 wt.%) solidified in the dendrite spacings. A more detailed investigation of the eutectic region showed that one of the components was a complex-composition light phase enriched with zirconium (27.9 wt.%) and containing the rest of the filler alloy components (spectrum 3 in Figure 5; Table 3).

The second component of the eutectic was a dark phase, which solidified in the form of fine 0.4–1.6 μm inclusions (see spectra 4 and 5 in Figure 5; Table 3). The concentration of zirconium in this phase decreased to 19.50–20.87 wt.%.

It should be noted that the brazed seams and fillet regions contain insignificant amounts of

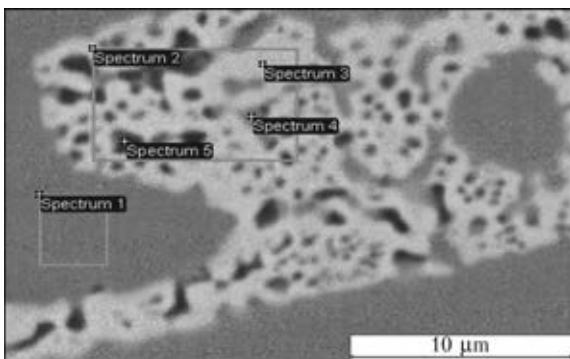


**Figure 5.** Microstructure of eutectic region of the brazed seam made by using filler alloy with the crystalline structure



**Table 2.** Chemical heterogeneity of regions of the brazed joints, wt.%

Spectrum number	Al	Ti	Mn	Ni	Cu	Zr
Fillet region (filler alloy with crystalline structure, Figure 3, b)						
1	0.44	57.06	–	6.40	30.75	5.34
2	1.51	44.81	0.73	13.37	15.82	23.76
3	2	73.08	0.47	5.29	11.74	7.42
Seam (filler alloy with amorphous structure, Figure 4, a)						
1	0.87	50.23	–	10.43	22.90	15.58
2	0.38	54.59	–	7.91	27.71	9.41
3	1.35	46.20	0.47	12.86	14.72	24.40
4	1.81	76.08	0.55	4.47	9.93	7.17
5	0.73	60.90	–	7.01	25.82	5.54
6	1.86	77	0.38	4.56	10.16	6.04
7	1.87	75.34	1.06	5.50	6.01	10.22
Seam (filler alloy with crystalline structure, Figure 4, b)						
1	0.64	51.25	0.20	10.63	22.35	14.94
2	0.33	54.61	0.13	8.50	28.84	7.59
3	1.11	46.01	0.47	13.61	15.69	23.12

**Table 3.** Chemical heterogeneity of the eutectic region of the seam brazed by using filler alloy with the crystalline structure

Spectrum number	Al	Ti	Mn	Ni	Cu	Zr
1	0.43	54.94	0.04	8.52	28.53	7.54
2	1.06	47.85	0.58	13.62	13.53	23.36
3	1.08	39.68	0.45	16.54	14.35	27.91
4	0.60	46	0.31	13.24	20.35	19.50
5	1.15	52.39	0.38	12	13.23	20.87

which occur during brazing at interface between the phases and lead to liquation chemical heterogeneity and formation of non-equilibrium structures, as solidification of metal of the brazed seam and fillet region takes place under non-equilibrium conditions.

At constant brazing parameters (identical temperature, holding time, heating and cooling rates) a decrease in width of the brazing gap (to 4–5 μm) leads to identical changes in morphological structure of the seams brazed by using filler alloy with the amorphous (Figure 6, a, c) and crystalline (Figure 6, b, d) structure.

There were no eutectic regions in the classical meaning of this word. A flat front of solidification of the seam with formation of the two-phase structure was observed (Figure 6, a, b; Table 4). Decrease in the gap reduced the ways of diffusion

aluminium and manganese, which are components of the titanium alloy being brazed. This can be explained by the mutual diffusion processes between the base material and filler alloy,

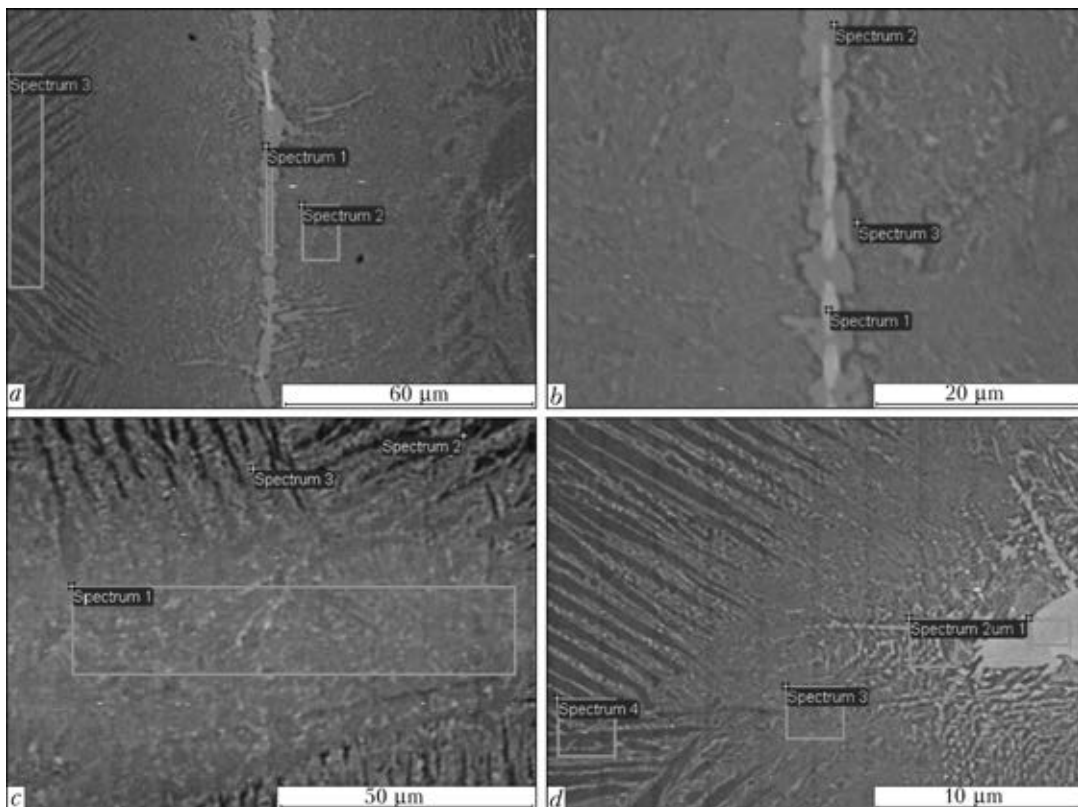


**Figure 6.** Microstructures of the seams made with decrease in the brazing gap by using filler alloy with the amorphous (a, c) and crystalline (b, d) structure



**Table 4.** Chemical heterogeneity of the seams with decrease in the brazing gap, wt.%

Spectrum number	Al	Ti	Mn	Ni	Cu	Zr
Filler alloy with amorphous structure (Figure 6, a)						
1	0.64	55.03	–	6.53	26.66	11.15
2	1.86	75.93	0.55	4.49	8.49	8.68
3	3.40	85.98	0.56	2.64	5.03	2.38
Filler alloy with crystalline structure (Figure 6, b)						
1	1.73	39.04	0.39	12.80	17.44	28.60
2	0.40	54.99	–	7.34	27.73	9.53
3	2.79	84.16	0.39	1.41	2.72	8.52
Filler alloy with amorphous structure (Figure 6, c)						
1	2.11	79.60	0.50	3.19	7.93	6.67
2	3.33	91.69	–	–	2.47	2.51
3	2.02	79.52	1.36	4.90	6.81	5.40
Filler alloy with crystalline structure (Figure 6, d)						
1	0.58	56.51	–	6.58	30.16	6.15
2	2.01	76.25	–	4.08	11.16	6.50
3	2.13	80.63	0.51	3.48	8.86	4.39
4	3	89.08	–	1.53	4.43	1.96

in the molten filler alloy, thus promoting leveling of its chemical composition in width of the seam.

Further decrease in the brazing gap when using the filler alloy with the amorphous structure led to narrowing of the seam, and the diffusion zone of common base metal grains, which is the seam, was observed in the capillary (practically zero) gap. The common base metal grains contained an increased amount of aluminium, i.e. 2.11 wt.%, and a decreased amount of components of the filler alloy (see spectrum 1 in Figure 6, c; Table 4). This structure was caused by the fact that the filler alloy and base metal had a common metallic base, i.e. titanium. Owing to

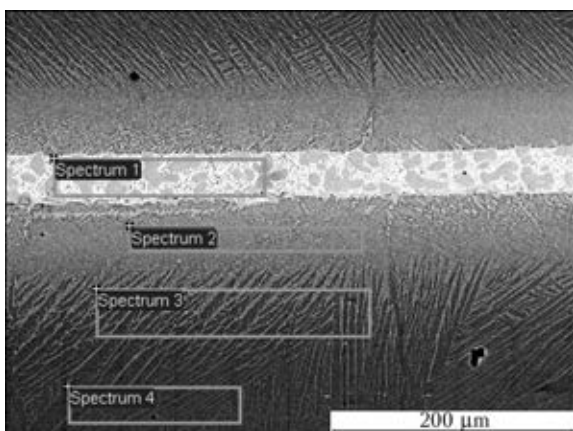


**Figure 7.** Microstructure of the joint brazed with the amorphous filler alloy

**Table 5.** Chemical heterogeneity of the joint brazed with the amorphous filler alloy, wt.%

Spectrum number	Al	Ti	Mn	Ni	Cu	Zr
1	0.68	49.61	–	12.15	21.17	16.39
2	1.92	78.40	–	4.97	9.16	5.56
3	3.22	89.10	0.74	2.60	3.13	1.22
4	3.67	95.41	0.91	–	–	–

the diffusion processes the concentration of components of the filler alloy in this zone was greatly decreased: zirconium – down to 6.67, copper – to 7.93, and nickel – to 3.19 wt.%. Metallographic examinations and X-ray spectrum microanalysis confirmed this formation of the brazed seam also in the case of using filler alloy in the crystalline state.

The cast filler alloy melted during brazing, flowed into the almost zero gap due to the capillary forces and formed the reverse fillet. There was no seam as it is in this region of the joint. Instead we saw a diffusion zone in the form of common, intergrown base metal grains based on titanium (see Figure 6, d) and enriched with zirconium, i.e. 4.39 wt.% (spectrum 3 in Figure 6, d; Table 4), like in the case of using filler alloy with the amorphous structure.

In the base metal the concentration of zirconium decreased with increase in distance from the seam. For example, in the seam the concentration of zirconium was 16.39 wt.%, whereas with distance from the seam (in the normal direction, at a distance of about 100 μm) its concentration decreased to 1.22 wt.%, and no zirconium was detected at a distance of 150 μm (spectrum 4 in Figure 7; Table 5).

The data of X-ray spectrum analysis are indicative of a high diffusion activity of zirconium and its ability to penetrate to a large depth into the titanium alloy, which is explained by an unlimited solubility of titanium and zirconium over the wide concentration ranges. The examination results indicated that the diffusion zone always contains components of the filler alloy, but in small concentrations.

As established on the basis of the results of metallographic examinations and X-ray spectrum analysis, structure of the seam metal in the brazed titanium joints made by using the given filler alloy (constant parameters of vacuum brazing) depends on the width of the brazing gap. The smaller the brazing gap, the closer is the structure of the seam to that of the base metal.

Morphological peculiarities and chemical composition of the phases solidifying in a wide

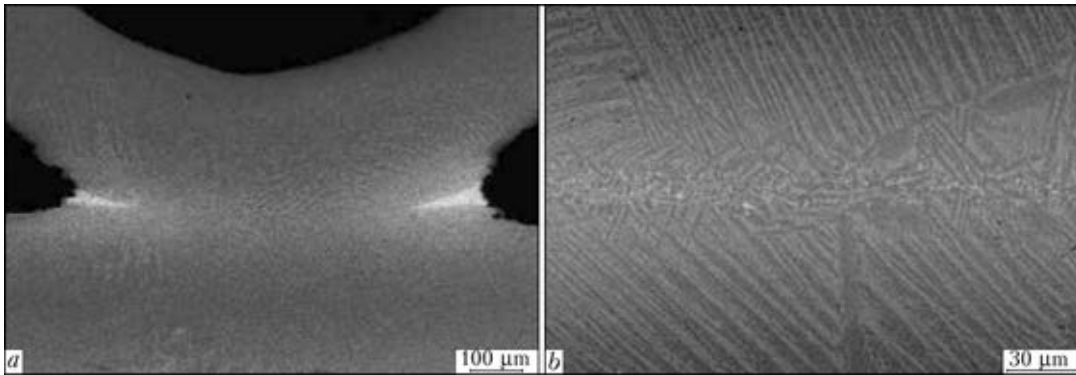


**Figure 8.** Microstructures of brazed fragment of the lamellar-ribbed titanium heat exchanger: *a* – general view of the joint with fillet regions; *b* – central zone of the seam

region of the seam of the joints brazed by using filler alloy Ti–23Cu–12Zr–12Ni in the amorphous state are similar to those of the wide brazed seams made by using filler alloy in the cast state. Volume solidification of metal similar to solidification of metal in an ingot is dominant in big gaps.

Brazed joints on thin-walled elements of a complex geometric shape (Figure 8, *a*, *b*) illustrating the above morphological peculiarities of structure formation are a typical example of formation of the brazed seams with a variable gap (filler alloy 30 μm thick, amorphous state). It should be noted that the use of the Ti–Zr–Ni–Cu system filler alloys in the amorphous state in the form of thin plastic strips is important for brazing of thin-walled elements of heat-exchanging titanium devices, when it is necessary to keep strictly to the brazing gap parameters and produce simultaneously (in one heating cycle) a large number of the dense brazed seams.

Therefore, it was established from the results of metallographic examinations of the titanium alloy brazed joints with a variable gap that vacuum brazing using filler alloy Ti–23Cu–12Zr–12Ni in the amorphous and crystalline states provides good formation of the brazed joints, dense sound seams and absence of any defects. The plastic thin (30–50 μm) filler alloys in the amorphous state provide the stable width of the brazing gap.

Microstructure and morphological peculiarities of the seams brazed at constant temperature-time parameters of the brazing process depend on the width of the brazing gap, rather than on

the aggregate state of the filler alloy. Examinations of the brazed joints with a variable gap showed that a microstructure characteristic of the cast metal with the eutectic component forms in wide gaps and fillet regions containing a high amount of the filler alloy when using filler alloy both in the amorphous and in the crystalline state. In the capillary gaps the seam is a diffusion zone with common base metal grains enriched with the filler alloy components, which forms in brazing using filler alloy in the amorphous and crystalline states.

1. Kovneristy, Yu.K. (1992) *Amorphous vitreous metallic materials*. Moscow: Nauka.
2. Kalin, B.A., Sevryukov, O.N., Fedotov, B.T. (1996) Amorphous strip filler alloys for brazing. Experience of development of the production and application technology. *Svarochn. Proizvodstvo*, **1**, 15–19.
3. Kalin, B.A., Fedotov, V.T., Sevryukov, O.N. et al. (2001) Rapidly quenched filler alloy for brazing of metal structures. *Perspekt. Materialy*, **6**, 82–87.
4. Kalin, B.A., Sevryukov, O.N., Fedotov, V.T. (1996) Brazing of thin-sheet structures of titanium alloys with amorphous filler alloys STEMET. *Svarochn. Proizvodstvo*, **9**, 23–24.
5. Khorunov, V.F., Maksymova, S.V. (2005) Production and application of rapidly quenched filler alloys. *Ibid.*, **12**, 25–30.
6. Kalin, B.A., Sevryukov, O.N., Fedotov, V.T. et al. (2001) New amorphous filler alloys for brazing of titanium and its alloys. *Ibid.*, **3**, 37–39.
7. Shpak, A.P., Kunitsky, Yu.A., Lysov, V.I. (2002) *Cluster and nanostructural materials*. Vol. 2. Kiev: Akadempriodika.
8. Maksymova, S.V. (2007) Amorphous filler alloys for brazing of stainless steel and titanium, and structure of brazed joints. *Adgeziya Rasplavov i Pajka Materialov*, **40**, 70–81.

Received 13.12.2013

# NEW ELECTRODES FOR REPAIR SURFACING OF RAILWAY FROGS\*

I.K. POKHODNYA, I.R. YAVDOSHCIN, N.V. SKORINA and O.I. FOLBORT

E.O. Paton Electric Welding Institute, NASU

11 Bozhenko Str., 03680, Kiev, Ukraine. E-mail: office@paton.kiev.ua

Analysis of technical characteristics of TsNIIN-4 electrodes used for repair of railway frogs showed a necessity in modernization of indicated electrodes and development of new sparsely-alloyed electrodes of similar designation on a basis of low-carbon wire Sv-08. The results of work on selection of optimum composition for gas-slag-forming system of coating and system for alloying of deposited metal as well as technical characteristics of modified electrodes TsNIIN-4M and new sparsely-alloyed electrodes ANN-10 are represented. Technical and economical advantages of new electrodes in comparison with TsNIIN-4 electrodes are shown. Specifications for TsNIIN-4M and ANN-10 grade electrodes were developed, agreed and registered in the «Ukrmetrteststandart» and technological process of their industrial production was created. Results of work on production of pilot-industrial batches of new electrodes and their testing are stated. Development of modern ANN-10 and TsNIIN-4M electrodes allows refusing from application of expensive high-alloy wire Sv-10Kh14G14N4T that reduces a prime cost of the electrodes and increases their competitiveness in the market of welding consumables. 6 Tables, 1 Figure.

**Keywords:** *electrodes, arc surfacing, railway frog, hardness of deposited metal*

TsNIIN-4 electrodes are the most widespread electrodes for manual arc surfacing of railway frogs, rails and points in Ukraine and CIS countries. The electrode cores from high-alloy wire of Sv-10Kh14G14N4T grade are used for their manufacture. Price of the latter is sufficiently high and makes 8–9 USD per kilogram for Ukrainian consumers considering transport expenses and customs duties. The cores from Sv-10Kh14G14N4T wire have a tendency to buckling (bend out) in a process of heat treatment that increases reject of electrodes on geometry. High price of materials (electrode wire, manganese and metallic chromium) included in the coating increases price of the electrodes even greater up to 12–13 thou USD per ton.

High-alloy wire has higher electric resistance than wire from low-carbon steel. Therefore, current used for surfacing by TsNIIN-4 electrodes is limited in order to prevent electrode overheating, that, in turn, reduces surfacing efficiency.

Surfacing by TsNIIN-4 electrodes can be performed only at reversed polarity direct current, and this fact in some cases results in magnetic blow and formation of defects caused by it.

Aim of the present work lies in development of electrodes based on domestic welding wire Sv-08A and refuse from application of Sv-10Kh14G14N4T wire. Investigations on selection of optimum thickness of electrode coating and content of alloying additives in it were carried out for providing necessary chemical composition of deposited metal in changing of Sv-10Kh14G14N4T wire on Sv-08A wire.

Adjustment of gas-slag-forming part of the coating was carried out for improvement of welding-and-technological properties of the electrodes. Considering high content of metallic powders (65 wt.%) which are «thinning» materials impairing plasticity of an electrode compound in the coating, organic and mineral plasticizing agents were additionally introduced in the coating composition. This insured improvement of the electrode compound plasticity and provided possibility of quality deposition of electrode compound over the core, small polythickness of the coating and good marketable state of the electrodes. Thus, composition of coating of modified electrodes TsNIIN-4M was formed.

Testing of welding-and-technological properties of the modified electrodes showed that they provide stable arcing at direct as well as alternating current. At that, if TsNIIN-4 electrodes

\* The paper is prepared on results of execution of Purpose Complex Program of the NAS of Ukraine «Problems of Resource and Safety Operation of Structures, Constructions and Machines» (2010–2012).

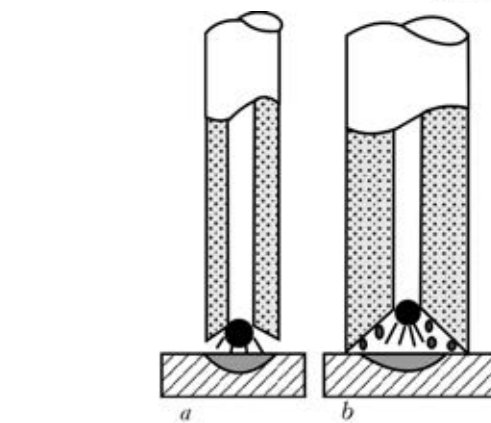
**Table 1.** Welding-and-technological properties of 4.0 mm diameter electrodes

Parameter	TsNIIN-4	TsNIIN-4M
Maximum allowable current, A	140	210
Nominal arc voltage, V	28	25
Possibility of AC surfacing	Only DCRP	DC, AC
Coating diameter, mm	6.0	8.2
Coefficient of coating weight, %	50	135
Linear speed of melting at maximum current, cm/min	24.1	20.3
Efficiency of surfacing, kg/h	1.5	1.8

are overheated in welding at current above 140 A, then TsNIIN-4M electrodes allow performing welding at 210 A without significant overheating of the coating. Such an advantage is caused by significantly larger thickness of the coating and application of core from low-carbon wire which has smaller electric resistance in comparison with Sv-10Kh14G14N4T wire.

It should be noted that surfacing using TsNIIN-4 electrodes is to be performed by free arc in order to prevent «bridging» of inter-arc gap by large drop and sticking of electrode to the part. TsNIIN-4M electrodes allow performing touch surfacing, that significantly reduces loading on welder's arm. Thick coating in melting forms a deep crater which is touched by the electrode, that provides such a possibility of surfacing. Large depth of the crater eliminates the possibility of bridging of arc gap by drop.

Formation of fine-ripple uniform bead, easy separability of slag crust and insignificant metal spattering are provided in surfacing by modified TsNIIN-4M electrodes as experiments showed. Table 1 shows the main indices of welding-and-technological properties of the electrodes. Linear speed of melting of TsNIIN-4M electrodes is lower than that of TsNIIN-4 electrodes, as can be seen from the Table data. Larger thickness of coating of the modified electrodes explains this fact. However, efficiency of surfacing at that is



Type of melting and transfer of metal of TsNIIN-4 (a) and TsNIIN-4M (b) electrodes

20 % higher than for TsNIIN-4 electrode that is caused by high content of metallic powders in the coating of the modified electrodes and large thickness of the coating.

Hygiene indices of the electrodes were evaluated on intensity and specific emissions of solid constituent of welding fume (SCWF) (Table 2) and its chemical composition (Table 3).

As can be seen from data presented, specific emissions of SCWF is 15 % lower per 1 kg of molten electrodes and 8–10 % lower per 1 kg of deposited metal in surfacing by TsNIIN-4M than by TsNIIN-4 electrodes.

In our opinion, lower specific emissions of SCWF in welding by TsNIIN-4M electrodes are caused by peculiarities of melting and transfer of electrode metal. As earlier performed investigations showed, the increase of thickness of electrode coating and rise of content of metallic fraction (ferroalloys and metallic powders) in it promote increase of quantity of metal and slag drops coming in a pool from periphery of the electrode (Figure). These drops of metal and slag are not overheated to such high temperatures as a main drop formed on a tip of the electrode core. Therefore, processes of evaporation from the surface of periphery drops are less intensive.

Six-layer depositions were performed using reversed polarity direct current for determination

**Table 2.** Intensity and specific emissions of SCWF in surfacing by TsNIIN-4 and TsNIIN-4M electrodes (DCRP)

Electrode grade	Mode of surfacing		SCWF emission, g		
	$I_w$ , A	$U_a$ , V	Per 1 min	Per 1 kg of molten electrodes	Per 1 kg of deposited metal
TsNIIN-4	140	26–28	$\frac{1.26-1.41}{1.33-3}$	$\frac{37.9-43.5}{40.6-3}$	$\frac{52.8-55.2}{54.3-3}$
TsNIIN-4M	200	24–25	$\frac{1.46-1.53}{1.50-3}$	$\frac{33.9-35.0}{34.5-3}$	$\frac{49.3-51.7}{50.7-3}$

Note. Here and in Table 6 the maximum and minimum values are given in numerator, and average values of indices and number of experiments — in denominator.

**Table 3.** Chemical composition and hardness of metal deposited by TsNIIN-4 and TsNIIN-4M electrodes

Electrode grade	Weight fraction of elements, %							Hardness <i>HRC</i>
	C	Si	Mn	Cr	Ni	S	P	
TsNIIN-4	0.80	0.62	13	22.40	2.90	0.035	0.037	29
TsNIIN-4M	0.79	0.45	12.50	23.30	3.20	0.035	0.025	27
Requirements of normative documents	0.50–0.80	0.80	11–14	22–28.50	2–3.50	0.035	0.040	25–37

**Table 4.** Results of calculation of costs of materials for manufacture of 1 t of electrodes

Used materials	TsNIIN-4		TsNIIN-4M	
	Consumption per 1 t of electrodes, kg	Cost, UAH	Consumption per 1 t of electrodes, kg	Cost, UAH
Gas-slag-forming	176	747	154.7	712
Alloying	124.5	16,340	340.0	38,614
Plasticizing and binding agents	75	390	164.5	877
Welding wire Sv-10Kh14G14N4T	678	61,427	–	–
Welding wire Sv-08A	–	–	467.0	3526
Total	–	78,904	–	43,729

of chemical composition and hardness of metal deposited by TsNIIN-4 and TsNIIN-4M electrodes. Value of current made 140 and 200 A for TsNIIN-4 and TsNIIN-4M electrodes, respectively. Spectral method was used for analysis of chemical composition of the deposited metal. Data from Table 3 shows that modified TsNIIN-4M electrodes completely meet the requirements of normative documents for TsNIIN-4 electrodes on chemical composition and hardness of deposited metal.

Modernizing of TsNIIN-4 electrodes allowed refusing from expensive Sv-10Kh14G14N4T wire. As can be seen from Table 4, expenses on materials for manufacture of modified electrodes are lower (on 35175 UAH) than for TsNIIN-4 electrodes.

High service properties (wear resistance, hardness etc.) of the deposited metal can be provided at more sparsely alloying (less content of chromium, absence of nickel etc.) in comparison with alloying applied for TsNIIN-4 electrodes. Therefore, sparsely-alloyed electrodes ANN-10 of the same designation as TsNIIN-4 were developed

at the E.O. Paton Electric Welding Institute in parallel with modernization of TsNIIN-4 electrodes.

ANN-10 electrodes are analogues to foreign electrodes UTC BMC of German company UTP (today «Boehler Schweißtechnik Deutschland»), which have been already delivered in Ukraine more than ten years. All-Russian Institute of Railway Transport on the results of tests made back in 1996 stated that UTP BMC electrodes significantly exceed TsNIIN-4 electrodes on mechanical and technological properties and can be used in repair of railway frogs. At that, content of chromium and nickel in the metal deposited by them are significantly lower (Table 5).

Testing of pilot batch of ANN-10 electrodes, manufactured at the E.O. Paton Electric Welding Institute, showed that they are comparable with UTP BMC electrodes and exceed TsNIIN-4 electrodes on welding-and-technological properties.

Sparsely-alloyed electrodes are in order higher than TsNIIN-4 electrodes and 2–3 times than

**Table 5.** Chemical composition of metal (wt.%) deposited by TsNIIN-4, TsNIIN-4M, UTP BMC and ANN-10 electrodes

Electrode grade	C	Mn	Si	Cr	Ni	S	P
TsNIIN-4	0.5–0.8	11–14	≤0.8	22–28.5	2–3.5	≤0.035	≤0.040
TsNIIN-4M	0.5–0.8	11–14	≤0.8	22–28.5	2–3.5	≤0.035	≤0.040
UTP BMC	0.6	16.5	0.8	13.5	–	0.032	0.036
ANN-10	0.4–0.8	14.5–18.5	0.6–1.0	12–15	–	≤0.040	≤0.040

**Table 6.** Impact toughness of metal (J/cm<sup>2</sup>) deposited by sparsely-alloyed electrodes of pilot batch, TsNIIN-4 and UTP BMC electrodes of 4.0 mm diameter on specimens of type IX

Testing temperature, °C	UTP BMC	TsNIIN-4	Sparsely-alloyed electrodes
20	$\frac{36.3-71.9}{54.2.3}$	$\frac{8.8-16.7}{11.8.3}$	$\frac{111.0-115.5}{113.5.3}$
-20	$\frac{20.9-35.4}{28.5.3}$	$\frac{8.6-10.6}{9.7.3}$	$\frac{92.6-103.8}{97.3.3}$

UTP BMC electrodes on impact toughness of the deposited metal (Table 6).

Indicated effect becomes apparent at normal as well as at lower temperature (-20 °C), that is, obviously, related with more fine-grained austenite structure in comparison with UTP BMC electrodes. According to existing opinion, the metal deposited with TsNIIN-4 electrodes contains extremely high quantity of chromium, that causes low level of their mechanical properties and, first of all, impact toughness.

ANN-10 electrodes are more favorable from economical point of view since their prime cost is lower than of TsNIIN-4 and TsNIIN-4M electrodes due to smaller consumption of expensive ferroalloys and application of low-carbon wire

Sv-08A as a core instead of expensive high-alloy wire Sv-10Kh14G14N4T.

TsNIIN-4M and ANN-10 can be ordered in the PWI Scientific-and-Engineer Center on Consumables for Welding and Surfacing.

### Conclusions

1. Replacement of cores from high-alloy wire Sv-10Kh14G14N4T by low-carbon wire Sv-08A was used for modernization of composition of TsNIIN-4 electrodes' coating that allows improving technological and hygiene indices of the electrodes and reducing their prime cost by 30–35 %.

2. Sparsely-alloyed ANN-10 electrodes exceeding TsNIIN-4 electrodes on technological characteristics were developed for surfacing of railway frogs and points.

3. ANN-10 electrodes are more favorable than TsNIIN-4 from economical point of view since they have the minimum prime cost due to lower consumption of expensive ferroalloys and application of low-carbon wire Sv-08A as a core.

4. Packages of normative documents were developed for TsNIIN-4M and ANN-10 electrodes that allows starting their industrial production.

Received 24.01.2013

## NEWS

### *Diagnostics of Stressed State of Structures and Constructions Based on the Method of Electron Speckle-Interferometry*

Residual stresses are known to be the cause for many accidents occurring in operation of facilities. Such accidents involve considerable expenses for repair and reconditioning of the equipment, as well as potential hazard for human life and health.

The proposed technology improves the reliability and life of structures and constructions made from various structural materials. Instrumentation for on-line diagnostics of the stressed state and computer system of processing and analysis of the data obtained by the method of electron speckle-interferometry, operate in real time mode. The instrumentation is compact and allows determination of residual stresses under the actual service conditions for assessment of operational reliability of structures and constructions.

Equipment components: compact small-sized (17 mW) source of coherent laser radiation, polarized light guide designed for laser radiation transmission into the controlled zone;

- controlled piezooptic element designed for achieving a phase shift in processing of optical data;
- speckle-interferometer designed for strain measurement at stress relaxation in the controlled zone;
- highly-sensitive CCD-camera designed for transmission of reflected laser radiation to computer memory;
- computer designed for entering, processing and analysis of optical data derived at strain measurement in the controlled section of the structure;
- spare part kit.

# APPLICATION OF MECHANIZED WELDING WITH SELF-SHIELDING FLUX-CORED WIRE IN REPAIR OF METALLURGICAL EQUIPMENT

V.N. SHLEPAKOV<sup>1</sup>, Yu.A. GAVRILYUK<sup>1</sup>, A.S. KOTELCHUK<sup>1</sup>, V.N. IGNATYUK<sup>1</sup>, P.A. KOSENKO<sup>2</sup>  
O.N. ROKHLIN<sup>3</sup> and A.V. TOPCHY<sup>3</sup>

<sup>1</sup>E.O. Paton Electric Welding Institute, NASU

11 Bozhenko Str., 03680, Kiev, Ukraine. E-mail: office@paton.kiev.ua

<sup>2</sup>SE «Pilot Plant of Welding Consumables of the E.O. Paton Electric Welding Institute»

2 Teligi Str., 04112, Kiev, Ukraine. E-mail: ozsm@paton-ozsm.com.ua

<sup>3</sup>PJSC «Dneprovsky F.E. Dzerzhinsky Metallurgical Works»

18B Kirov Str., 51925, Dneprodzerzhinsk, Ukraine. E-mail: dmkd@dmkd.dp.ua

The state-of-the-art and characteristics of objects of repair-and-restoration welding of equipment of mine-metallurgical equipment were considered. It was established that reduction of time of welding during repair of metallurgical equipment and increase of reliability of welded structures are possible due to widening of application of mechanized welding using self-shielding flux-cored wire. The investigation of physical and chemical properties of powder mixtures, modeling the cores of self-shielding flux-cored wires, allow determining the ways of increasing the technological characteristics of those wires during development of their compositions. The results of works on improvement of technology of production of flux-cored wires, allowing application the efficient routes of drawing, suitable for manufacture of flux-cored wires of small diameter (1.6 mm) per one stage of drawing using six-fold drawing mill. The successful realization of technology of wire drawing with deposition of protective coating on its surface for protection against corrosion and prevention of wetting of core materials. The successful examples of implementation of mechanized welding using flux-cored wire on the typical objects of repair-restoration works of enterprises of mine-metallurgical complex were shown. The evaluation of technical and economical characteristics of application of welding using flux-cored wires during repair-restoration works was made by calculation of expected economic effect from the replacement of manual arc welding by the mechanized one on the example of capital repair of converter. The decrease of cost of steel being melted is achieved by decrease of conditionally-constant costs at the general decrease of terms of the converter repair. 11 Ref., 7 Figures.

**Keywords:** *repair-restoration welding, flux-cored wire, service life, equipment, mine-metallurgical complex*

In repair of metallurgical equipment, in particular, housings of blast furnaces and bodies of converters, one of the kinds of works is rewelding of cracks and making of patches with next welding, restoration of geometric sizes of worn-out parts of equipment. The mentioned structures are manufactured of low-alloyed steels. The labor-efficiency of welding works is sufficiently high and duration of welding influences the terms of repairs and idle time of equipment. The technical documentation foresees performance of welding works during manufacture and repair of mentioned structures by manual arc welding using the type E50A electrodes of 4–5 mm diameter.

To reduce the time of welding during repair of housings of blast furnaces, bodies of converters and other metallurgical equipment the works on mastering the mechanized welding under site conditions were carried out. In the process of carry-

ing out of such works a number of factors was revealed impeding application of mechanized welding in shielding gas under the site conditions. Thus, presence of draughts, metallurgy dust and slags from oxygen cutting and manual arc welding, which getting into the groove, leads to the appearance of pores and other defects in a weld, considerably impeding the application of welding with a solid wire in shielding gases. Besides, delivery of cylinders with shielding gases to the place of works performance and maintenance requires additional labor efforts.

Therefore, the development of technology of mechanized welding of joints in all spatial positions is the actual need of enterprises for increase of technical characteristics of constructions and equipment and also for extension of their service life. Considering the difficulty and conditions of performance of repair-restoration works, the most promising is the development of technology of semi-automatic welding with flux-cored wire

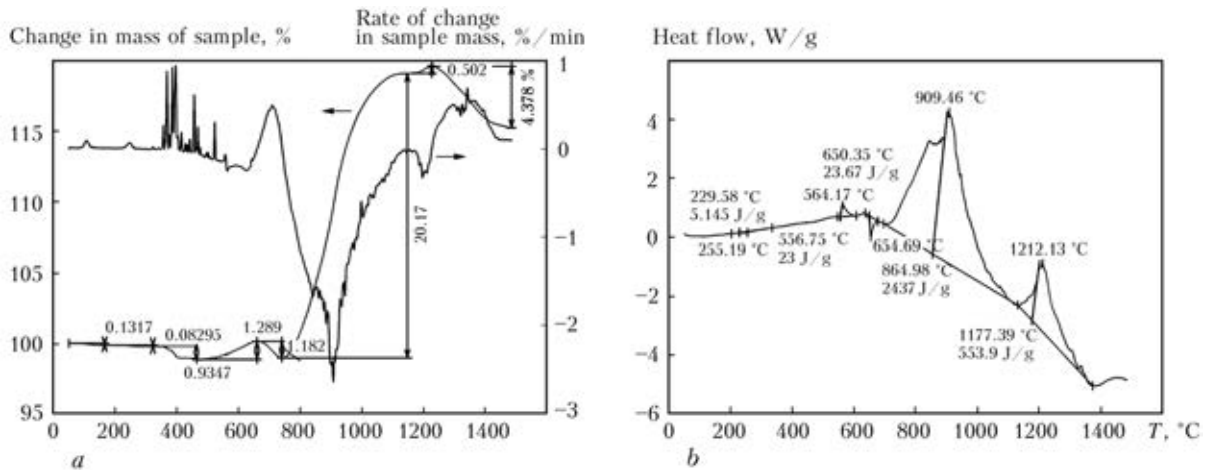


**Figure 1.** Results of thermogravimetric analysis (a) and analysis using method of differential scanning calorimetry (b) of charge of flux-cored wire of carbonate-fluorite type

of a small diameter which is the energy and resources saving process and allows providing high quality and efficiency of repair-restoration works.

The experience of implementation of mechanized and repair-restoration welding of metallurgical units using self-shielding flux-cored wire at the metallurgical plants of Ukraine proved the high efficiency of technology and increase of service reliability of metal structures [1]. Moreover, this experience revealed a need in further improvement of such welding technology [2, 3] and development of the new flux-cored wires which could allow widening the objects of application of this method, in particular, in mine-extracting and metallurgical complexes, production of building materials, mineral fertilizers.

Below some results of developments of flux-cored wires, updating of technology of their manufacture and conduction of works on their implementation on the example of metallurgical plants of companies «Dneprovsky F.E. Dzerzhinsky Metallurgical Works» and «ArcelorMittal Krivoy Rog» are given.

**Investigation of properties of flux-cored self-shielding wires.** The sheath of a flux-core wire is heated in welding mainly due to the heat, which is generated during passing of welding current and heat from the active spot of welding arc. On the stickout (at the area of a wire from the contact device of supply of welding current up to the arc) the temperature field close to quasi-stationary one is set. It allows modeling of a core of flux-cored wire as a cylinder of an infinite length, which is heated from the surface and edge, and carrying out estimations. To study processes of evaporation, dissociation, heat destruction and oxidation of components of a core of a flux-cored wire, which accompany heating and melting of powder composites during weld-

ing, the methods and technique of thermal analysis are applied: differential thermal, thermal gravimetric, differential thermal gravimetric analyses and differential scanning calorimetry [4]. The mentioned methods of thermal analysis are supplemented by mass-spectral analysis of a gas phase formed during heating and melting of powder mixtures being investigated.

Figure 1, a shows typical results of thermogravimetric analysis of charge of flux-cored wire of carbonate-fluorite type, which contains carbonates of calcium, magnesium, sodium, and also hexafluorosilicate of sodium. The curve of change of mass of sample can reveal the characteristic intervals of removal of absorbed moisture approximately to 150 °C, thermal decomposition of hexafluorosilicate of sodium with evolution of  $\text{SiF}_4$  at 380–450 °C and carbonates at 700–1450 °C with evolution of  $\text{CO}_2$ . The evolution of mentioned gases is proved by mass-spectral monitoring of composition of gas phase of heating chamber. At the temperature higher than 450 °C the increment of mass of sample is superposed on the processes of thermal destruction with evolution of gas-forming products due to development of oxidation of iron powder, ferroalloys and alloying components of charge of flux-cored wire. After 700 °C the increase of mass of sample is changed by its decrease, and in mass-spectrum the density of current of carbon gas ions is increased which is evidence of intensification of thermal dissociation of carbonates.

Figure 1, b shows results of analysis of the same sample of charge using method of differential scanning calorimetry and calculations of total effects of reactions. In the process of heating of mixtures of carbonate-fluorite type the negligible exothermal effects in the range of temperatures of 600–800 °C can be noted. The further heating is accompanied with successive change of

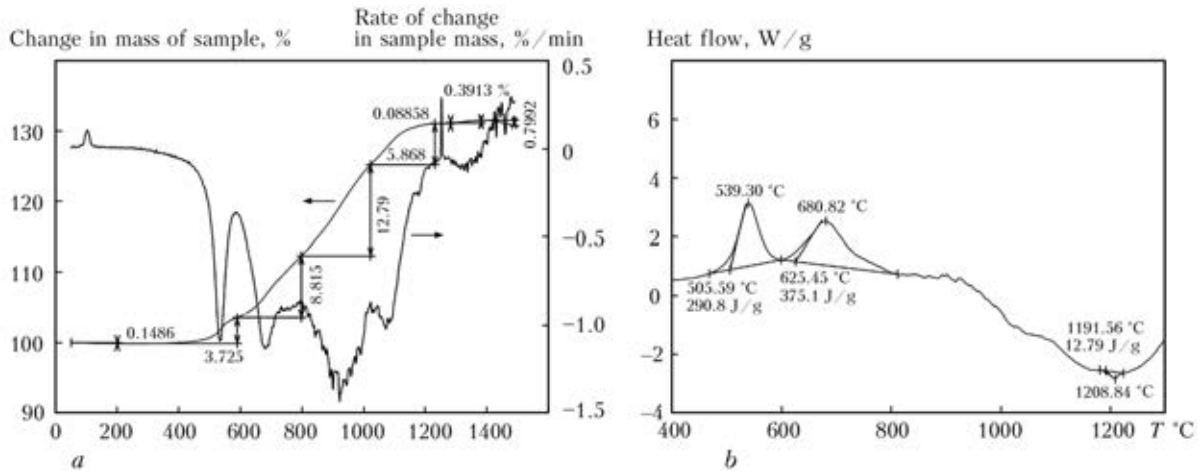


**Figure 2.** Results of thermogravimetric analysis (a) and analysis using method of differential scanning calorimetry (b) of charge of flux-cored wire of oxide-fluoride type

exothermal and endothermal effects, on which it can be judged about the simultaneous running of processes of destruction of mineral components and oxidation of metallic components. As-applied to self-shielding flux-cored wires of carbonate-fluorite type the experimental investigations, the results of which are presented in [5], allow establishing the fact that the more efficient gas shielding is provided by the core compositions, for which the processes of evolution of gases are extended throughout the whole range of temperatures from 400 °C to the temperatures of steel melting. In other words, the more stable gas shielding to environment influence is formed in welding using wires with cores generating the shielding gases at all the stages of their heating and melting.

Figure 2, a gives the typical results of thermogravimetric analysis of the flux-cored wire charge of oxide-fluoride type, which contains complex master alloys on aluminium base (in particular, master alloys Al–Li and Al–Mg). Figure 2, b shows results of analysis of the same sample of charge of flux-cored wire, carried out using method of differential scanning calorimetry and calculation of total thermal effects of reactions.

The process of heating of charges of flux-cored wires of oxide-fluoride type is characterized by exothermal effects at the temperatures of about 600 and 800 °C of considerably higher intensity, as compared to the charge of carbonate-fluorite type wire, which are accompanied by a growth in mass of sample and decrease in content of oxygen in gas phase of heating chamber, which testifies to intensive processes of oxidation of powders of aluminium and magnesium, iron powder, alloying components and ferroalloys. Slag melt for the analyzed charge is formed at the temperature close to 1200 °C with a noticeable

endothermal effect reaching its maximum at the above-mentioned temperature.

The investigation of physical and chemical properties of powder materials and their mixtures, modeling the core of flux-cored wire, which was carried out using methods of complex thermal analysis and also method of mass-spectrometry of gas phase at dynamic heating from 30 to 1500 °C, showed that the process of heating of model cores of flux-cored wires containing gas- and slag-forming components together with metallic powders is accompanied with running of reactions of destruction, gas evolution, oxidation and melting of mixtures with formation of primary melt of metallic and slag phases. The formation of slag melts even at the stage of powder core heating before the melting of wire sheath and evolution of gases (CO, SiF<sub>4</sub>) facilitates the increase in shielding functions of the wire during open arc welding. The thermal effects of thermochemical reactions, which accompany the process of heating, are running simultaneously (endothermal processes of destruction and melting and exothermal oxidation and complexation). Control of these reactions by the change of mixture composition allows controlling the rate of melting the flux-cored wire core to provide favorable characteristics of melting and transfer of electrode metal to the weld pool.

In capacity of components of flux-cored wire, facilitating the acceleration of melting and uniform evolution of shielding gas, it is rational to use mixtures of metallic powders based on aluminium and its alloys, non-metallic slag and gas-forming components of the type of carbonates, oxides and fluorides of alkali metals. The results of investigations are used in the development of small-diameter wire (1.6 mm) for welding in all spatial positions.

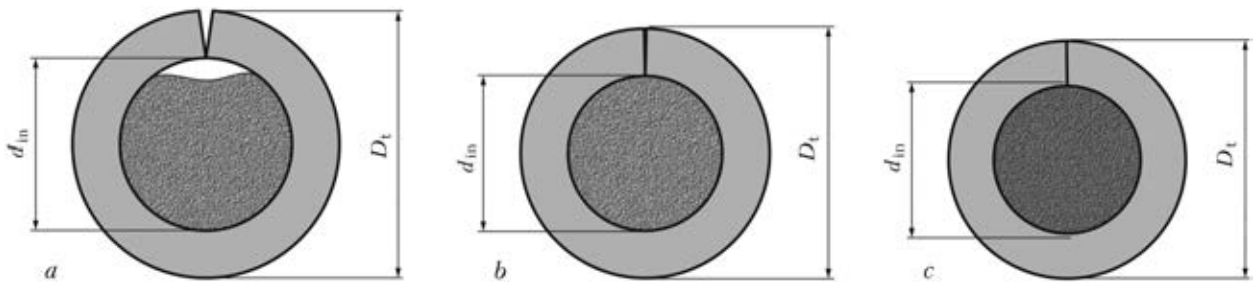


**Figure 3.** Profile of tube ( $D_t = 4.5$  mm) of flux-cored wire at outlet of forming device in traditional forming (a), and additional reducing of flux-cored wire tube ( $D_t = 4.2$  (b) and 4.0 (c) mm) by two pairs of rollers (b, c)

**Updating the technology of manufacture of flux-cored wire.** The available technological scheme of production of flux-cored wire at the PWI Pilot Plant of Welding Consumables is in compliance in general with the requirements specified to the manufacture of modern welding consumables. This scheme includes longitudinal cutting of wide steel strip into separate strips of a required size, increment of length by intermediate welding of strip ends with next heat treatment of welded joints, cleaning, degreasing and winding of strip on technological reels using the row layout without damage of edges and violation of geometry (up to 500 kg). The line of forming and drawing the flux-cored wire is equipped with a forming device and a batcher of powder mixture with the device for control of filling the wire sheath with a powder. The formed tube of wire is supplied directly to the uniflow six-fold drawing mill, arranged in one line with winding device, on which the same technological reels as for a strip are used for layer-by-layer winding. The system of control of the line provides the continuous automatic control of the whole process of the flux-cored wire manufacture.

However, the updating of technology of manufacture of flux-cored wire required certain changes into the existing scheme of forming and drawing of wire. For sealing the closing of butt of tubular profile of sheath, formed of steel strip, and fixation of wire powder core to prevent its possible shifting the additional roller reducing of flux-cored wire tube was introduced into the scheme of forming of wire sheath and filling it with powder charge. To realize this, the correction of values of successive deformations of wire tube during drawing (drawing route) was required. To increase the reliability of wire feed on the paths of welding semi-automatic machines preserving its properties under the site welding conditions caused also a need in re-examine of existing system of lubrication during drawing of wire tube. It appeared to be rational to carry out replacement of conventional drawing lubricant, which is supplied as a soap powder into the zone

of deformation of the wire tube, by the lubricants based on stearates. In addition, the final technological operation of treatment of the wire surface using protective pastes to create shielding coating was introduced into the technological process of manufacture.

The existing calibrating grooves of rollers of forming are designed by a so-called neutral diameter of sheath ring [6]. Therefore in manufacture of wire from increased thickness strip at the outlet of the forming device the tube with incomplete closing of edges is formed (Figure 3, a). To achieve the complete closing, the additional pair of rollers (Figure 3, b) is required, and considering also the necessity of packing of powder mixture before drawing, one more pair of rollers is required (Figure 3, c).

Based on the mentioned conditions the grooves of forming tool were designed and two pairs of forming rollers were manufactured, which are mounted additionally on two final positions of the forming unit (Figure 4). The experimental tests proved the rationality of using additional operations of final forming and packing of tube wire core, which allow decreasing the diameter of wire tube at the outlet of the forming unit by 15%. For initial sizes of strip of  $0.8 \pm 12$  mm, diameter of tube is decreased from 4.0–4.2 to 3.4–3.5 mm. The tube is supplied to drawing with a sealed butt of strip edges and



**Figure 4.** Two additional units of roller reducing of wire mounted on the machine of the OB1252MU type for forming the flux-cored wire tube

with an inner cavity, completely filled and packed with a charge, which practically excludes the fluctuations of composition and possible shifting of core powder along the length of wire under the influence of jerks and vibrations, especially at the stages of speed increase or stop of the line of flux-cored wire manufacture.

The achieved result allowed designing the more efficient route of drawing suitable for the flux-cored wire manufacture. The calculations made for the technology existed earlier showed impossibility of manufacture of 1.6 mm diameter flux-cored wire, foreseen by technical specifications, per one technological transition when applying the six-fold drawing. The preliminary reducing of the wire tube in unit of forming and filling opened such possibility.

The route of drawing is usually calculated coming out of deformation capabilities of composite tube of flux-cored wire and considering the mechanical properties of strip and technological conditions of drawing. These conditions should also foresee fitness of tube to coating by a primary layer of drawing lubrication, entire coating of wire by drawing lubrication at intermediate operations and preparation to protective coating deposition to its surface.

The route of drawing is usually designed according to the practice of deforming the steel or composite billets with steel shell with account for process of surface strengthening during treatment and need in preserving the deformational properties [6]. Typical organizing of the process of drawing the steel billets foresees small stepped deformations at the initial stage to orient structures in the direction of deformation. Further at the intermediate stages of drawing the levels of deformations are increased, and at the final stage of drawing the rather abrupt decrease in level of deformation is applied, because of need to provide the regulated values of tolerances for the diameter of ready products ( $\pm 0.1$  mm), which are specified by the standards on welding flux-cored wires [7, 8].

The calculations of routes of drawing under the condition of preliminary reducing of flux-cored wire tube allowed designing technology of manufacture of flux-cored wire of 1.6 mm diameter using uniflow mills of six-fold drawing available at the enterprise.

The experimental testing of drawing routes revealed necessity in correction of calculation route in the direction of increase of deformation at the stage of intermediate drawing and its decrease at the stages of primary and final drawing (during calibration). Considering the tolerances

for the size of ready-made wire specified by the standards DSTU GOST 26271 [7] and ISO 17632 [8], it occurred to be rational at the first pass to use the wire of 3.5–3.6 mm diameter, that allows making its calibration at the final stage for 1.59 mm diameter and provide manufacture of ready-made wire of a required size.

The forming of tube of flux-cored wire with sealed butt is performed from a strip passed the technological operations of cleaning and degreasing of surface, therefore, special treatment of the surface for drawing is not required. The sealing of the tube butt prevents getting of drawing lubricant into the butt gap and damage of a tool (drawing die) by strip edges. The process of drawing of flux-cored wire with the next deposition of protective coating required replacement of a soap powder applied for drawing of wire tube by a special system of lubricants. According to the existing statements of the theory and practice of drawing of steel wires such system should reliably cover the surface of wire even at the first stage of drawing, which requires application of lubricants of «strong» type with antioxidants and fine-grain fraction of a powder, which remains on the surface after drawing in a form of a thin covering layer [9–11]. At the final stage of wire drawing there is a possibility of deposition of special protective coating using lubricant, which forms a liquid phase during drawing (due to extremely low temperature of melting) and remains a fine layer of quickly-hardening protector at the wire surface [11].

To solve this task, the tests of different types of lubricants were carried out, among which three of them were selected, corresponding to the tasks and conditions of industrial drawing. For the primary drawing the lubricant was selected on the base of calcium stearate ( $C_mH_nCOOCa$ ). For the intermediate one it appeared to be rational to use powdered lubricant on the base of sodium stearate ( $C_mH_nCOONa$ ) with additions of antioxidants, while at the final stage of drawing the powdered paste of low melting temperature was selected, where the main acting filler material is a dispersed powder of tetrafluoroethylene. Getting to the zone of deformation of the wire tube this powder is poly-condensed (polymerized) under the influence of pressure, forming a dry film in the place of contact with the surface, which tightly covers it and has antifriction properties. The conditions of stable formation of such film at the surface in the zone of deformation are the presence of liquid-phase state of lubricant in the zone of deformation and local zone of increased pressure (about 0.01 MPa). Under such condi-

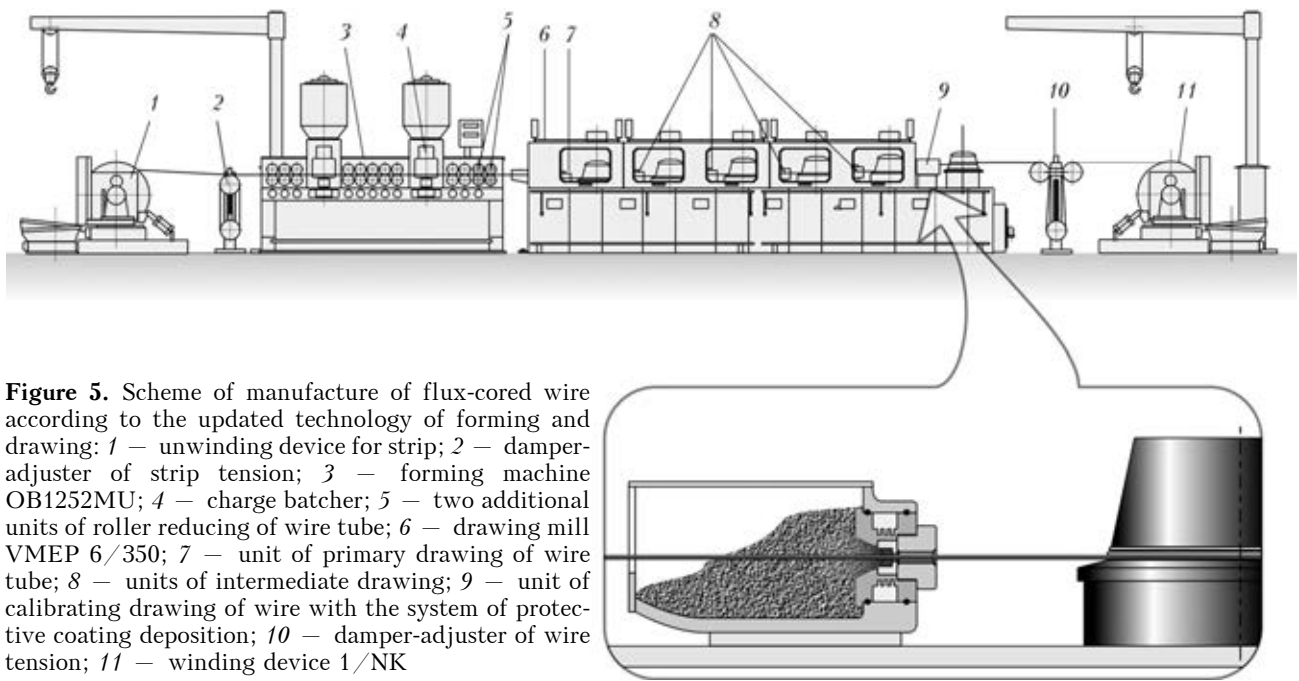


**Figure 5.** Scheme of manufacture of flux-cored wire according to the updated technology of forming and drawing: 1 – unwinding device for strip; 2 – damper-adjuster of strip tension; 3 – forming machine OB1252MU; 4 – charge batcher; 5 – two additional units of roller reducing of wire tube; 6 – drawing mill VMEP 6/350; 7 – unit of primary drawing of wire tube; 8 – units of intermediate drawing; 9 – unit of calibrating drawing of wire with the system of protective coating deposition; 10 – damper-adjuster of wire tension; 11 – winding device 1/NK

tions in the zone of deformation and calibration of the flux-cored wire the film 3–5  $\mu\text{m}$  thick is formed at its surface. The stable formation of the film takes place at use of drawing dies with a smooth change of curvature from the entry to the working zone up to exit (from  $12^\circ$  at entry, further through the calibrating zone up to  $40^\circ$  at exit).

The setting-up of technology of drawing the wire with deposition of protective coating at its surface was carried out at the PWI Pilot Plant of Welding Consumables in the line of manufacture of flux-cored wire using the forming unit OB1252MU (equipped with additional reducing rollers), drawing mill VMEP 6/350 and winding device of the 1/NK type at the speed of the wire manufacture of up to 300 m/min.

The produced samples of 1.6 mm diameter flux-cored wire of tubular design were tested according to the requirements of standards DSTU GOST 26271 [7] and ISO 17632 [8]. Moreover, the efficiency of deposited protective coating for anticorrosion protection of ready flux-cored wire at its storage in the atmosphere with controlled humidity was checked.

The scheme of manufacture of the flux-cored wire of new type according to the updated technology of forming and drawing is given in Figure 5.

**Implementation of welding with self-shielding flux-cored wire at the enterprises of mining-metallurgical complex.** At the Dneprovsky F.E. Dzerzhinsky Metallurgical Works the bodies of converters, housings of blast furnaces and other metal structures of metallurgical equipment were defined as the objects for implemen-

tation of the flux-cored wire welding. The largest volume of welding at the initial stage of works was the repair welding of objects with making welds in flat, horizontal and vertical positions (shields, strengthening girths, cover plates, etc.). In welding at the open areas it was found that application of self-shielding flux-cored wire provides a stable process even under effect of wind at the rate of up to 8 m/s without deterioration of the weld quality. This allowed including the tolerance into the welding regulations for application of wire at the rate of wind of up to 7 m/s, which several times exceeds the capabilities of use of solid wires in welding process under the site conditions.

The works on mechanized welding under the site conditions were carried out using self-shielding wire in capital repair of converter body (Figure 6). In the process of repair the cracks were rewelded and welding of patches (type of weld S-19) was performed at the remained backing (Figure 7) at the thickness of metal of up to 80 mm. The welding was performed in flat, horizontal and vertical positions.

In the process of capital repair of a body of one converter about 30 m of welds were welded, the half of which was performed by the mechanized welding with flux-cored wire PP-AN7, and the rest – by the manual arc welding using electrodes ANO-27. As a result it was managed to find that efficiency of mechanized self-shielding flux-cored wire welding is approximately 2–2.5 times higher than that of manual covered-electrode arc welding. Moreover, according to the observations over the service life of welds, their



**Figure 6.** Repair welding of metallurgical equipment at the Dneprovsky F.E. Dzerzhinsky Metallurgical Works using the self-shielding flux-cored wire

mechanical properties are higher in case of the flux-cored wire application. Thus, to the moment when some welds, made by manual arc welding, were destroyed and required repeated repair, the welds, made by mechanized flux-cored wire welding, remained sound and continued their functions. The application of mechanized welding gives an opportunity to perform welding into the narrower gap, that allows rewelding the crack at its opening for width of more than 15 mm without treatment of edges across the entire thickness of metal.

At ArcelorMittal Krivoj Rog company the repair shops mastered the technology of mechanized welding and surfacing with self-shielding flux-cored wires PP-AN7 and PP-AN19N during repair of the main units of enterprise under the site conditions. Thus, for example, in the period of regular-preventive repairs of rolling and blooming mills the Repair shop of metallurgical equipment performed the following kinds of welding-surfacing works: restoration surfacing of seats of bearings of the roller supports of conveyors of blooming mills; surfacing of rods of pushers of blooming manipulators rulers; surfacing of rollers of large and small transfer skid

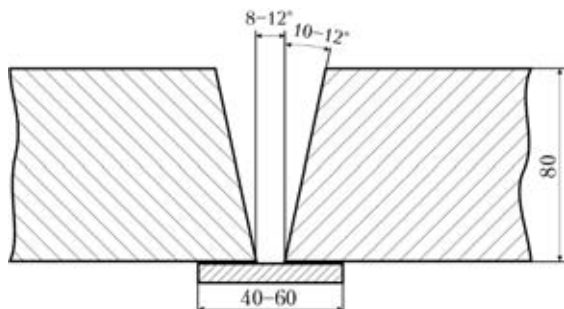


**Figure 7.** Preparation of groove edges for flux-cored wire welding in repair of converter body

fields; surfacing of pointers of distributing tables of sorting rolling shops; welding of cracks in metal structures of blooming manipulator rulers; surfacing of chutes of tribounits; surfacing of worn-out places of conveyors for cuttings collection; surfacing of  $\Pi$ -shaped straps of mill rolls 1250 and 1300; rewelding of cracks in the platforms of ingots cars.

Restoration surfacing with self-shielding wire PP-AN19N was excellent in making buffer layer before strengthening surfacing.

The most significant application for this wire for surfacing during fulfillment of repair orders in machine building production shops of mechanical repair complex became the restoration of shaft of conical crusher of a coarse crushing, belonged to the Mining Department of the Enterprise. The mass and dimensions of the as-assembled shaft with cone did not allow mounting a unit into any surfacing machines. The decision was taken to carry out the restoration of geometric sizes of cone shaft in a specially designed and manufactured device using the mechanized surfacing with self-shielding flux-cored wire. During surfacing three welding semi-automatic machines were used, the mass of deposited metal was about 1.5 t. Due to high efficiency of mechanized method of welding-surfacing as compared to the manual arc surfacing using covered electrodes it was managed to reduce the number of welders engaged in repair works, and also to reduce greatly the terms of restoration of the equipment serviceability.

As compared with the mechanized welding and surfacing with solid wires the advantage of application of self-shielding flux-cored wires is the elimination of gas-cylinder equipment in the technological process. Under confined site conditions and during short-term repairs the flux-cored wire welding becomes simply irreplaceable.

According to the results of pilot-industrial tests of mechanized welding with self-shielding flux-cored wire the decision was taken to widen the volumes of application of this method in repair-restoration works carried out on the metal structures and equipment of metallurgical enterprises. The measures on technical and technological preparation of enterprises for widening the nomenclature of objects recommended for implementation of the flux-cored wire welding were defined.

The requests remained to the designers of the flux-core wires in the necessity of mastering the technology of manufacture and industrial production of self-shielding flux-cored wires of 1.2–1.6 mm diameter.

**Technical-economical data on application of flux-cored wire welding in repair-restoration works.** The calculation of expected economic efficiency from the replacement of manual arc welding by mechanized one with flux-cored wires was carried out on the example of capital repair of converter by determination of decrease of cost of melted steel due to decrease of conventionally-constant expenses at total reduction of terms of the converter repair.

The reduction of duration of welding works  $\Delta t$  at the repair of converter at the Dneprovsky F.E. Dzerzhinsky Metallurgical Works in case of application of mechanized self-shielding flux-cored wire welding amounts to  $\Delta t = 36$  h/year. Then the reduction in cost of steel melted per year (saving) will amount to

$$E_c = B_1 B_s \Delta t = 60 \cdot 310.5 \cdot 36 = 670,680 \text{ UAH,}$$

where  $B_1 = 60$  UAH/t are the conditionally-constant expenses for melting of one ton of steel, UAH;  $B_s = 310.5$  t/h is the hour's production of steel.

The implementation of technology of welding using flux-cored wire allows improving the efficiency and labor conditions, decreasing the power consumption, improving service properties of welded joints.

### Conclusions

The results of investigations of physical and chemical properties of powder mixtures — models of cores of flux-cored wires at dynamic heating — allow determination of ways to improve technological properties of flux-cored wires and to develop new wires providing the required characteristics.

The implementation of mechanized self-shielding wire welding at the enterprises of mining-metallurgical complex proved the increase of efficiency of welding works by more than twice.

Moreover, the saving of power is provided, resistance of welded joints to formation of hot and cold cracks and service properties of welded joints due to normalization of weld and fusion zone are increased. Due to decrease of labor consumption for main and auxiliary operations the labor conditions of workers are improved which allows obtaining the significant economic effect.

1. Shlepakov, V.M., Gavrylyuk, Yu.O., Kotelchuk, O.S. et al. (2009) Technology of renovation of units and load lifting mechanisms in design position using flux-cored wire welding. In: *Problems of resource and service safety of structures, constructions and machines*. Kyiv: PWI, 634–640.
2. Ilyushenko, V.M., Voropaj, M.M., Polyakov, V.O. (2006) Technological specifics of automatic arc welding processes in repair of large-size tanks. *Ibid.*, 527–531.
3. Bolshakov, V.N. (2005) Problems of improvement of strength and reliability of furnace mantles in works of IFM. In: *Fundamental and Applied Issues of Ferrous Metallurgy*, Issue 11, 237–246.
4. Shlepakov, V.N., Kotelchuk, A.A. (2012) Investigation of thermochemical characteristics of mixtures of dispersed materials by differential thermal analysis methods. *The Paton Welding J.*, **12**, 13–16.
5. Shlepakov, V.N., Suprun, S.A., Kotelchuk, A.S. (1990) Estimating of the characteristics of flux-cored wire welding under the wind flow effect. In: *Proc. of Int. Conf. on Welding under Extreme Conditions* (Helsinki, Finland, Sept. 4–5, 1989). Oxford; New York: Pergamon Press, 171–179.
6. Pokhodnya, I.K., Alter, V.F., Shlepakov, V.N. et al. (1980) *Manufacturing of flux-cored wire*. Kiev: Vyscha Shkola.
7. *DSTU (GOST) 26271–84*: Flux-cored wires for arc welding of carbon and low alloy steels. Moscow: Standart.
8. *ISO 17632:2004(E)*: Welding consumables — Tubular cored electrodes for gas shielded and non-gas shielded metal arc welding of non-alloy and fine grain steels — Classification. Switzerland ISO copyright office.
9. Cherednichenko, G.I., Frojsheter, G.B., Stupak, P.M. (1986) *Physico-chemical and thermophysical properties of lubricants*. Leningrad: Khimiya.
10. Ishchuk, Yu.L. (1986) *Technology of plastic lubricants*. Kiev: Naukova Dumka.
11. (2001) *Lubricants for the metal forming industry*: Richards Apex. USA P.A.

Received 25.01.2013

# HYBRID LASER-PLASMA WELDING OF STAINLESS STEELS

**I.V. KRIVTSUN, A.I. BUSHMA and V.Yu. KHASKIN**  
E.O. Paton Electric Welding Institute, NASU  
11 Bozhenko Str., 03680, Kiev, Ukraine. E-mail: office@paton.kiev.ua

Welding of thin-sheet stainless steel joints receives acceptance in many industries. As a rule, argon-arc, resistance or plasma welding processes are used for these purposes. Investigation of the advanced world experience in application of welding processes shows that the intensive research is underway now on hybrid laser-plasma welding used to address the above problems. This study is dedicated to investigation of technological capabilities of this welding process. Technological investigations of hybrid laser-plasma welding of stainless steels of the austenitic and ferritic grades were carried out, and its comparison with the plasma and laser welding processes was performed. Mechanical properties of the hybrid welded joints were evaluated, and their structure was examined. Prospects of practical application of laser-plasma welding of thin-sheet stainless steel joints were shown. The ranges of parameters of hybrid welding of stainless steels, where there is no need to use filler materials, were found. It was established that the joints produced by this method are not inferior in their mechanical properties and quality of the weld formation to the laser welded ones, but in a number of cases are superior to them, and are much superior in quality of the weld formation to the plasma welded joints. Productivity of hybrid welding is 2–3 times higher than that of laser welding, and up to 4 times higher than that of plasma welding. 9 Ref., 2 Tables, 6 Figures.

**Keywords:** *stainless steels, hybrid laser-plasma welding, laser radiation, diode laser, hybrid effect, structures, microhardness, mechanical properties, prospects of application*

At present there are many industries that face a number of problems related to the need to weld thin-sheet parts of stainless steels, such as manufacture of expansion bellows for nuclear power engineering and food industry, tanks of refrigerating units to store milk products, etc. The problems posed here include welding of food and commercial stainless steels up to 3–4 mm thick with the butt, overlap and sometimes slot welds. As a rule, such problems are solved by using resistance [1] or argon-arc welding [2], and more rarely – plasma welding [3].

The issue of using this or other welding method is associated with certain optimisation requirements (price of the equipment and its operating cost, quality of the resulting joints, their strength and service life, presence or absence of residual distortions, etc.). Unfortunately, the applied welding methods do not always meet in

full the said requirements. For example, one of the best welding methods (with the absence of residual distortions and production of the high-quality and durable joints) is laser welding. However, this method has not received wide acceptance now because of a comparatively high price of laser equipment. One of the ways of reducing the price of the laser equipment is to decrease its output power by partially replacing it with the plasma-arc component in the welding process. This process is called hybrid laser-plasma (or laser-arc) welding [4, 5]. A new promising welding technology may result, providing that the quality of the welded joints in this case is kept close to that of the laser welded joints. So, this study was dedicated to investigation of this possibility.

Investigations of the process of hybrid laser-plasma welding of stainless steels were carried out in accordance with the flow diagram shown in Figure 1. The diode laser with 0.808 and 0.940  $\mu\text{m}$  radiation wavelengths was used in the experiments. Diameter of the focal spot was var-

**Table 1.** Chemical composition of stainless steel specimens, wt.%

Steel grade	C	Si	Mn	Cr	Mo	Ni	V	W	S	P	Cu	Ti
08Kh17T	≤0.08	≤0.8	≤0.8	16–18	≤0.3	≤0.6	≤0.2	≤0.2	≤0.025	≤0.035	≤0.3	≤0.8
Kh18N10T	≤1	≤0.8	≤2	17–19	≤0.4	10–12	≤0.2	≤0.2	≤0.2	≤0.035	≤0.4	≤0.7

ied in a range of 1.0–1.5 mm by using the focusing optics. The laser beam was combined with the constricted electric arc. The direct-action integrated plasmatron was developed for this purpose [6]. In this plasmatron the laser beam and the constricted arc were guided jointly via the common nozzle (2.0–2.5 mm diameter) to a workpiece to be welded, which was located at about 2 mm from the exit section of the nozzle. The focal plane of the laser beam was located at a depth of 0–0.5 mm from the workpiece surface. The straight-polarity continuous-action electric arc was used in the experiments. The arc current of the integrated plasmatron was gradually adjusted up to 110 A at an arc voltage of up to 20 V.

When performing penetration and butt welding of workpieces of stainless steels Kh18N10T (austenitic) and 08Kh17T (ferritic) with thickness  $\delta = 1.0\text{--}3.5$  mm, the range of adjustment of the laser power was 0.7–2.0 kW, and that of the welding current was 50–110 A at an arc voltage of 18 V. Chemical composition of the steels used is given in Table 1. Welding was carried out using no filler metals. The plasma and shielding gas was argon. The welding speed was varied

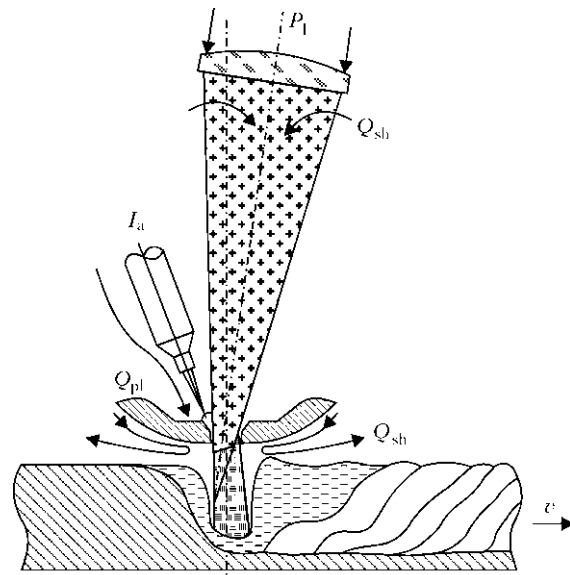


**Figure 1.** Flow diagram of the process of laser-plasma welding of stainless steels:  $P_1$  – laser radiation power;  $v$  – welding speed;  $I_a$  – arc current;  $Q_{pl}$  – plasma gas flow rate;  $Q_{sh}$  – shielding gas flow rate

from 14 to 108 m/h (3.8–30 mm/s). Three welding methods were investigated: laser, plasma and hybrid laser-plasma ones. The experimental results are given in Table 2.

**Table 2.** Parameters of welding of butt (steel 08Kh17T) and penetration (steel Kh18N10T) joints (plates 3 mm thick)

Steel grade	Welding method	Heat input, J/mm	Laser power, kW	Welding speed, m/h	Welding current, A	Arc voltage, V	Result
08Kh17T	Laser	360	2	20	–	–	
08Kh17T	Plasma	357	–	20	110	20	
08Kh17T	Hybrid	375	1	20	60	20	
Kh18N10T	Laser	75	1	50	–	–	
Kh18N10T	Plasma	140	–	50	110	20	
Kh18N10T	Hybrid	137	1	50	50	20	

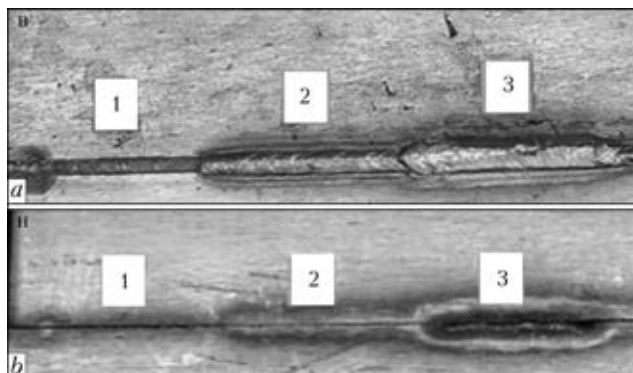


**Figure 2.** Appearance of the upper (*a*) and lower (*b*) sides of the butt joint on the specimens made from steel 08Kh17T ( $\delta = 3.5$  mm): 1 – laser; 2 – plasma; 3 – hybrid welding

In the majority of cases, at a selected ratio of workpiece thicknesses and welding speeds the laser and plasma processes taken separately did

not allow achieving the complete penetration, whereas hybrid laser-plasma welding provided the quality weld formation (Figure 2). Drawbacks of the plasma process also include deviation of the anode spot from the joint, which was observed even at a minimal deformation of the joint assembled in a clamp. This drawback is related not only to the deformation of the workpiece being welded, but also to the effect of wandering of the anode spot, the higher the welding speed, the more pronounced being this effect [3].

In all the cases the upper bead formation was of high quality. The lower bead formation (the hybrid process) depended on the laser beam power density, i.e. the size of the focal spot. At a minimal size of the spot (with growth of the radiation power density) the lower bead formation stability increased, and the effect of wandering of the anode region of the plasma arc minimised. It is the opinion of the authors that this process was strongly affected by stabilisation of the plasma arc by the beam (fixation of the arc to the focused beam [7]), rather than the laser radiation power.

The experiments established the presence of the «hybrid» effect, which consists in the non-additive increase in volume of the molten weld metal in the laser-arc process, compared to the total volume of the weld metal melted separately by the laser and plasma methods (see Table 2). Also, it was established that as the size of the focal radiation spot decreases (with growth of the radiation power density), the weld width decreases with a simultaneous increase in the penetration depth, i.e. the hybrid effect becomes more pronounced.

Another important result of technological investigations of the hybrid welding process was defining of such process parameters which did not require the use of any filler metal. It was found that if the laser-arc method provides the weld in a joint between the 3.0–3.5 mm thick sheets, in which width of the lower bead is not in excess of quarter of width of the upper bead, the weld may have no sag. Moreover, the bead reinforcement approximately 0.5 mm high may form in the weld. In this case the shape of the cross section of the weld will be closest to that observed in laser welding.

Investigations of microhardness of the welds showed that in the case of laser and plasma welding the instability of hardness in the cast weld metal and HAZ metal was higher than in the case of hybrid laser-plasma welding. This dependence is more pronounced for the steels that are sensitive to formation of quenching structures. In our

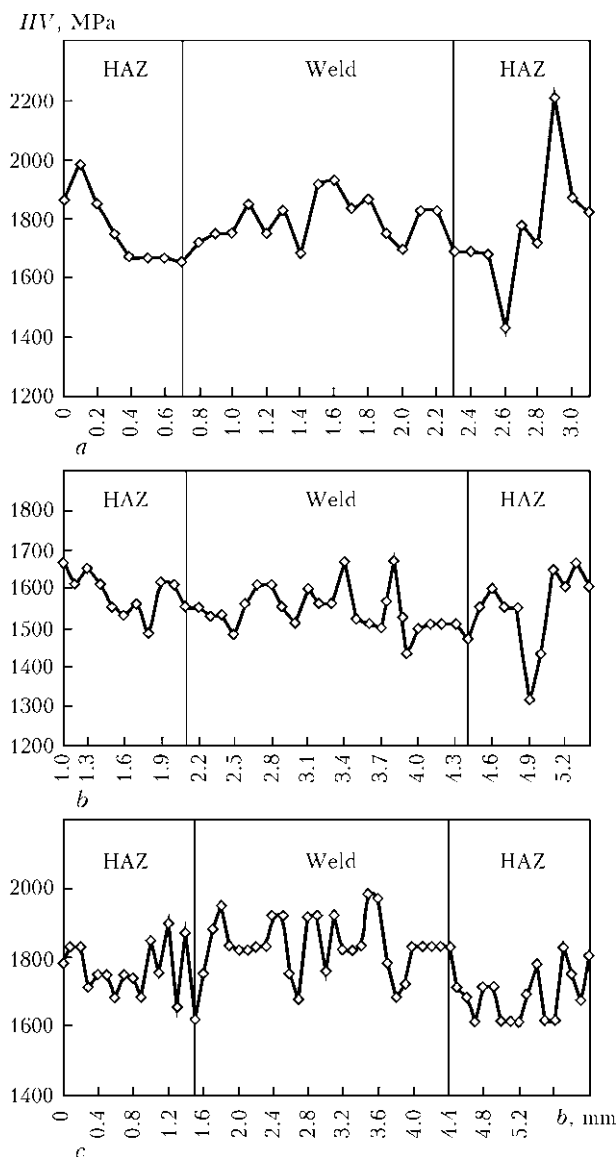


**Figure 3.** Measurements of microhardness (load of 50 g) in cross section of the welds of specimens made from steel 08Kh17T ( $\delta = 3.5$  mm): *a* – laser; *b* – plasma; *c* – hybrid method

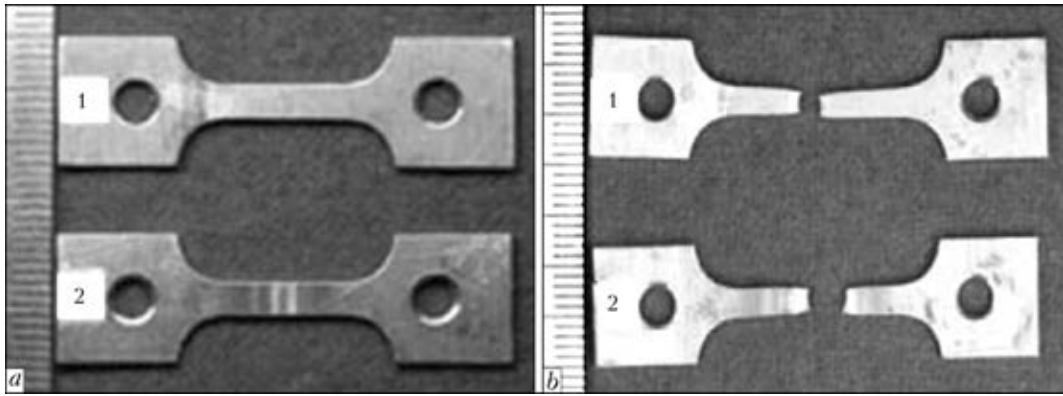


**Figure 4.** Appearance of specimens Mi-96 (steel Kh18N10T,  $\delta = 3.5$  mm) before (a) and after (b) tensile tests: 1 – BM; 2 – butt joint

case it is steel 08Kh17T (Figure 3). Note that formation of structures with an increased hardness in laser welding is caused to a greater degree by a high thermal locality of the process and small sizes of the weld and HAZ (Figure 3, a). This also leads to formation of quenching structures in the HAZ metal. Unlike laser welding, formation of the increased-hardness structures in hybrid welding is caused primarily by a high speed of the process. Therefore, increase in hardness is observed mainly in the cast weld metal (Figure 3, c). In laser welding, some decrease in impact toughness may be expected in the HAZ metal, and in hybrid welding – in the weld.

To conduct mechanical tests the following specimens: Mi-96 (GOST 6996–66) – for determination of tensile strength (Figure 4), and Mi-50 (GOST 9454–78) – for determination of impact toughness, were cut out from the quality regions of the welds made by the three methods being compared. The tensile tests were carried out by using tensile testing machine TsDM-4 at +20 °C. For this, three templates were cut out from specimen 195 for the hybrid butt welded joint, and three templates – for the base metal (BM). The test results on tensile strength  $\sigma_t$  of the butt

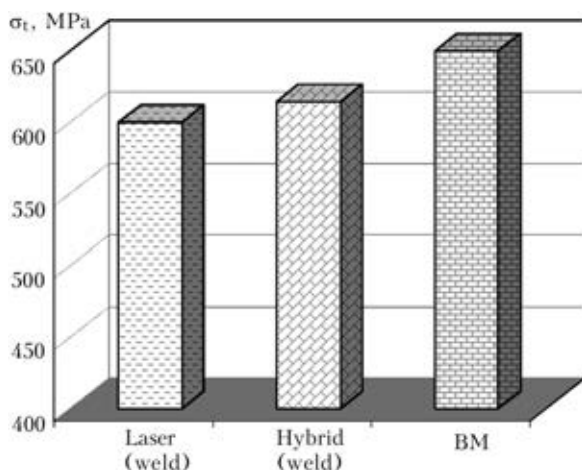


**Figure 5.** Tensile strength of specimens made from steel 08Kh17T

joints on steel Kh18N10T (fracture location – near-weld zone) showed that the level of  $\sigma_t$  for the welded joints is equal to about 0.85 $\sigma_t$  of BM ( $\sigma_t = 620$ – $679$  MPa for the welded joint at  $\sigma_t$  of BM equal to 750–760 MPa), which is higher than the corresponding values for the welded joints made by the arc methods [8]. These results are in good agreement with the data on electron beam welding of specimens of the American 304 type steel performed in a pressure chamber [9].

Templates of the laser and hybrid welded joints (series of three pieces) made at the same process parameters were prepared to conduct tensile tests of specimens of steel 08Kh17T ( $\delta = 3.5$  mm). The specimens of BM were prepared as well. The tests were carried out at +20 °C. It was found that strength of the specimens welded by the hybrid method was 3–5 % higher than that of the specimens made by the laser method, and approximately 5–7 % lower than that of BM (Figure 5).

The tests to impact toughness *KCV* (by the Charpy method) were carried out according to

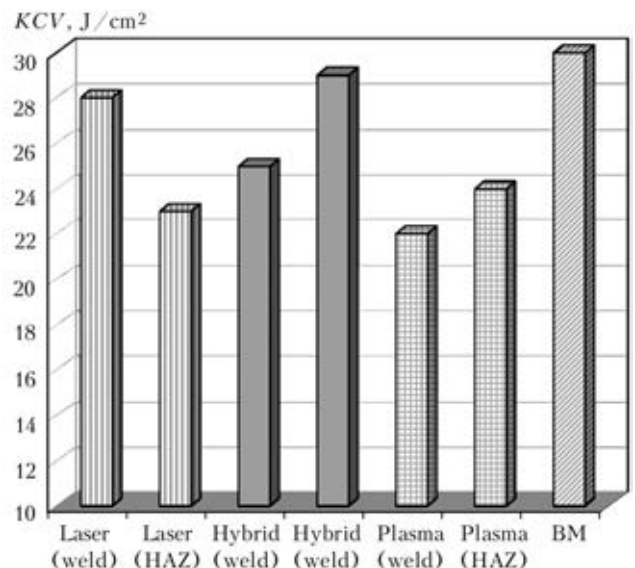


**Figure 6.** Impact toughness of specimens made from steel 08Kh17T



GOST 9454–78 by using pendulum hammer K-15 at +20 °C. Results of these tests obtained on specimens Mi-50 from steel 08Kh17T ( $\delta = 3.5$  mm) are shown in Figure 6. As expected, decrease in impact toughness of the laser welded joints was observed in the HAZ metal, and decrease in impact toughness of the hybrid welded joints – in the cast weld metal. The distribution of impact toughness in the welded joints made by the plasma method was similar to that observed with the hybrid method, the only difference being that toughness in the plasma weld was lower approximately by 10 %, and in the HAZ metal – by 15–18 %.

Therefore, as proved by the investigations, the hybrid laser-plasma welding method holds promise for addressing industrial problems of joining thin-sheet (up to 3–4 mm thick) stainless steels of both austenitic and ferritic grades. It was established that hybrid welding of such steels does not require the use of filler metals. The welded joints made by this method are not inferior in their mechanical properties to those made by laser welding, and in a number of cases are superior to them, and are much superior in quality to the plasma welded joints. The productivity of hybrid welding is 2–3 times higher than the pro-

ductivity of laser welding, and up to 4 times higher than that of plasma welding.

1. Chuloshnikov, P.L. (1977) *Resistance welding*. Moscow: Mashinostroenie.
2. Parshin, S.G. (2001) *Technology of manual argon-arc welding of 12Kh1MF steel pipes using activating flux*: Syn. of Thesis for Cand. of Techn. Sci. Degree. Toliatti: TolPI.
3. Malakhovsky, V.A. (1987) *Plasma welding*. Moscow: Vysshaya Shkola.
4. Kaul, R., Kumar, H., Rao, B.T. et al. (2010) Studies on characteristics of CO<sub>2</sub> laser-GTAW hybrid welding of austenitic stainless steel. *J. Laser Appl.*, **22**, 79–86.
5. Li, D., Ji, H., Liu, Y. et al. (2011) Simulation on temperature and residual stress field of laser-MIG hybrid welding of A6N01-T5 alloy. *Adv. Mater. Res.*, **399–401** (Nov.), 2040–2043.
6. Paton, B.E., Gvozdetsky, V.S., Krivtsun, I.V. et al. (2002) Hybrid laser-microplasma welding of thin sections of metals. *The Paton Welding J.*, **3**, 2–6.
7. Shelyagin, V.D., Khaskin, V.Yu., Garashchuk, V.P. et al. (2002) Hybrid CO<sub>2</sub>-laser and CO<sub>2</sub> consumable-arc welding. *Ibid.*, **10**, 35–37.
8. Paton, B.E., Gvozdetsky, V.S., Dudko, D.A. et al. (1979) *Microplasma welding*. Kiev: Naukova Dumka.
9. Nazarenko, O.K., Kajdalov, A.A., Kovbasenko, S.N. et al. (1987) *Electron beam welding*. Ed. by B.E. Paton. Kiev: Naukova Dumka.

Received 04.09.2012

## NEWS

### *Devices for Improvement of AC Arc Stability*

Devices for arcing stabilization (DAS) are the instruments, connection of which to any arc welding transformers (earlier manufactured by industry and those manufactured now) allows an essential widening of the field of their application, additionally giving them the technological properties of welding rectifiers for coated-electrode manual arc welding and nonconsumable electrode argon-arc welding systems. The device uses the principle of energy pulse transfer into the welding arc at the moment of reversal of polarity of the latter.

*Technical and economic advantages:* Compared to analogs the device greatly improves welding quality – process stability, weld appearance, weld metal structure and its

mechanical properties; improves labour conditions-work can be performed by welder of a lower qualification level. Power saving is up to 15 %.

*Efficiency:* Increase of labour efficiency by 20 % due to increased time of stable arcing and reliability of its initial ignition.

*State of development:* DAS samples have been successfully tested in industry in argon-arc welding by nonconsumable electrodes of stainless steels, aluminium and its alloys, welding by coated electrodes, designed both for AC and DC, of different steel grades, in particular, positive results were obtained in welding of critical products and structures by UONI type electrodes.

# IMPROVEMENT OF FATIGUE STRENGTH OF OVERLAP JOINTS OF SHEET ALUMINIUM ALLOYS MADE BY FUSION WELDING

V.V. KNYSH, I.N. KLOCHKOV and I.V. BEREZIN

E.O. Paton Electric Welding Institute, NASU

11 Bozhenko Str., 03680, Kiev, Ukraine. E-mail: office@paton.kiev.ua

Overlap joints have the advantage of simplicity of their preparation and fit-up for welding, however, because of a number of technological factors, they are characterized by low values of cyclic fatigue life. The influence of structural eccentricity and overlap value on fatigue strength of overlap welded joints of sheet aluminium alloys AMg6 and 6061-T6 made by consumable electrode gas-shielded pulsed-arc welding was shown experimentally. Application of high-frequency mechanical peening of the zones of weld-to-base metal transition was proposed as cold straightening technique to lower the values of structural eccentricity and improve the values of welded joint fatigue strength. Low-intensity high-frequency peening from one side results in plastic deformation of the surface metal layer in the treatment zone, leading to formation of a system of residual stresses, the impact of which causes bending-out in the joint plane. Treatment mode is selected so that the angle of misalignment relative to load application in the treated joints was close to zero. It is found that strengthening by high-frequency mechanical peening of fillet sections of fusion zones of two fillet welds in sheet overlap joints of the studied aluminium alloys leads to increase of their limited fatigue limits on the base of fatigue lives from  $5 \cdot 10^3$  up to  $10^6$  cycles of stress alternation, thus increasing their cyclic fatigue life up to 30 times at zero-to-tension loading. 10 Ref., 4 Figures.

**Keywords:** arc welding, sheet aluminium alloys, overlap welded joints, fatigue strength, structural eccentricity, high-frequency mechanical peening, strengthening

Application of overlap welded joints of aluminium alloys is due to their high adaptability-to-fabrication. In view of the simplicity of preparation and fit-up for welding, they are often applied for welding sheet blanks. Another advantage of overlap joining of sheets also is no need for edge preparation at any thickness and smaller shrinkage stresses compared to butt welding. However, overlap welded joints, made by two one-sided fillet welds, feature a high stress concentration that is mainly due to the effect of structural eccentricity. Simultaneous action of eccentricity and stress raiser, which is due to geometrical shape of the joint, considerably lowers the fatigue strength of overlap joints [1].

To reduce postweld angular deformation of sheet welded elements various methods of hot and cold straightening of the entire structure and its individual components [1–8] are applied, which are based on application of nonuniform local or bulk plastic deformation. Such methods of straightening the structural elements include: hammer peening, postweld rolling of the weld, as well as bending along the weld and vibrational treatment of structural element [3]. The main

disadvantage of cold straightening at high treatment intensities is formation of high tensile residual stresses, nonuniformly distributed across the thickness. In addition, cold straightening does not always improve the profile geometry in the zone of weld-to-base metal transition [5, 9]. At straightening of sheet material surface, treatment by a jet of steel shot from one side is used [9, 10]. Plastically deformed surface layer of metal in the zone of such treatment makes an impact on lower-lying plastically undeformed metal layers, as an off-center force, and causes their elastic deformation. A system of residual stresses balanced across the thickness is formed, namely compressive stresses in the active work-hardened layer, tensile stresses in the lower-lying and central layers of metal and compressive stresses on the surface from the reverse side of the element. Low intensity shot blasting induces low levels of tensile residual stresses in the metal central layers, and compressive residual stresses induced on the surface promote a significant improvement of fatigue strength of the element in the straightening zone.

This work is devoted to experimental determination of the effectiveness of application of the technology of high-frequency mechanical peening (HFMP) of sheet overlap welded joints as a method of cold straightening, in order to increase the fatigue strength. Results of fatigue

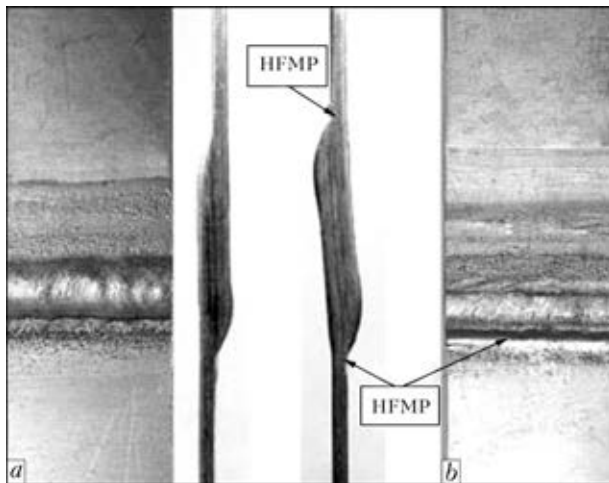


**Figure 1.** Samples of overlap welded joint in as-welded condition (*a*) and after HFMP of fusion zones (*b*)

testing are given for welded joints of aluminium alloys AMg6 (Al–Mg–Mn) and 6061-T6 (Al–Mg–Si) made by consumable electrode inert-gas pulsed-arc welding in as-welded condition and after HFMP.

At one-sided strengthening by HFMP technology of the zone of weld-to-base metal transition of overlap welded joints of the studied aluminium alloys, the effect of bending-out of welded joint plane is manifested, similar to the one found at low intensity shot blasting of the base metal. This promotes elimination of angular residual deformation in sheet overlap welded joints and, consequently, minimizes the undesirable moments of forces arising at loading of joints with structural eccentricity. Samples of overlap welded joints of AMg6 alloy 2 mm thick in the as-welded condition and after HFMP are given in Figure 1.

To perform experimental studies, blanks of overlap joints in the form of plates of 250 × 500 mm size with 2δ and 5δ overlap (mm) were welded from rolled sheets of aluminium AMg6 and 6061-T6 alloys 2 and 3 mm thick, respectively. Welding was performed by two welds with consumable electrode in a mixture of argon and helium. In welding the plates were rigidly fixed in the jig.

The angle of misalignment φ of application of force *F* in overlap joints was determined through the ratio of the value of eccentricity *e* to joint width as follows:

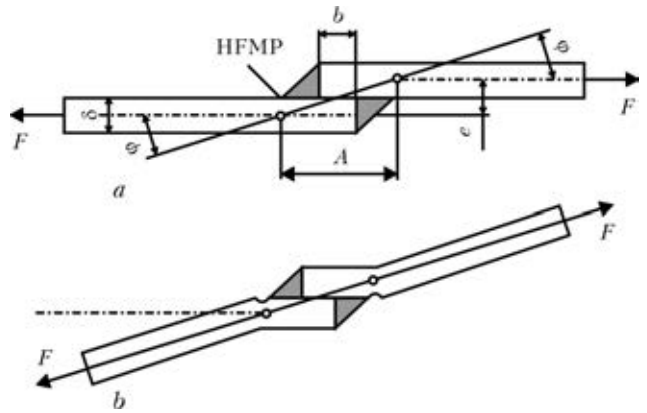


**Figure 2.** Schematic of overlap joint: *a* – as-welded condition; *b* – after HFMP

$$\varphi = \arctg \left( \frac{e}{A} \right).$$

Width of joint *A* (Figure 2, *a*) was taken to be equal to the sum of overlap size and two sizes of weld leg, equal to base metal thickness δ. For overlap joints of base metal plates of the same thickness δ, eccentricity *e* was equal to plate thickness, respectively. At HFMP strengthening of two fusion zones of overlap joints of the studied aluminium alloys treatment modes were selected so that the angle of misalignment φ in strengthened joints was close to zero (Figure 2, *b*).

Fatigue testing of samples of overlap joints 250 mm long with 40 mm width of the working section (Figure 3) in as-welded condition and after local HFMP was conducted in servohydraulic testing machine MTS 318.25 with digital control at zero-to-tension cycle asymmetry. Samples were cut out normal to the joint from large-sized welded blanks.

It is experimentally established that HFMP of the zone of weld-to-base metal transition increases the limited fatigue limit of overlap joints over the entire testing base from 5·10<sup>3</sup> up to 10<sup>6</sup> cycles of stress alternation of sheet aluminium alloys AMg6 and 6061-T6 (Figure 4). On the base of 10<sup>6</sup> cycles of stress alternation their conditional fatigue limit increases by 40 to 45 MPa, that is by 2.3–2.5 times for AMg6 alloy and by 2.7–3 times for 6061-T6 alloy (see Figure 4). Such an improvement of fatigue strength at application of HFMP of overlap joint is due primarily to elimination of structural eccentricity, as well as provision of a smother transition from weld to base metal and strengthening of the sur-



**Figure 3.** Sample of overlap joint for fatigue testing

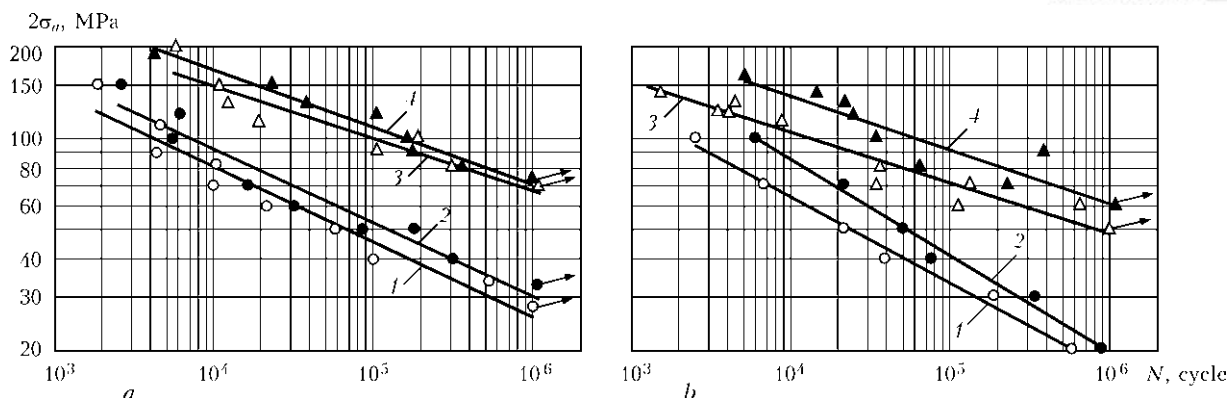


**Figure 4.** Fatigue curves of overlap joints: *a* – AMg6 alloy 2 mm thick; *b* – 6061-T6 alloy 3 mm thick; 1, 2 – as-welded condition with 2 $\delta$  and 5 $\delta$  overlap, respectively; 3, 4 – after HFMP with 2 $\delta$  and 5 $\delta$  overlap, respectively

face layer. Reduction of overlap size leads to lowering of joint fatigue life both in as-welded condition and after HFMP. This is related to the fact that at small overlap dimensions the value of angle  $\phi$  increases, and in joints with a small overlap size it can be decreased by spending more time for HFMP performance.

Thus, eccentricity or angular misalignment of force application in overlap welded joints of sheet aluminium structures can be eliminated with simultaneous formation of a more favourable profile of weld-to-base metal transition by treatment of fusion zones by HFMP technology.

### Conclusions

1. Fatigue curves of overlap joints of AMg6 alloy 2 mm thick and 6061-T6 alloy 3 mm thick with overlaps of two and five thicknesses, made by consumable electrode inert-gas pulsed-arc welding, in as-welded condition and after strengthening by HFMP, were determined.

2. It is experimentally established that HFMP of the two fusion zones of sheet overlap joints of aluminium alloys AMg6 and 6061-T6 improves the limited fatigue limits of the joints on the base of fatigue lives of  $5 \cdot 10^3$  up to  $10^6$  cycles of stress alternation, increasing their cyclic life by 25–30 times for AMg6 alloy and by 10–20 times for 6061-T6 alloy.

3. HFMP strengthening of fillet regions of fillet welds in sheet overlap joints improves the limited fatigue limit on the base of  $10^6$  cycles of stress alternation for AMg6 alloy up to 2.5 times, and for 6061-T6 alloy – up to 3 times at zero-to-tension alternating loading.

1. Kudryavtsev, I.V., Naumchenkov, N.E. (1976) *Fatigue of welded structures*. Moscow: Mashinostroenie.
2. Shonin, V.A., Mashin, V.S., Vojtenko, O.V. (2003) Improvement of fatigue resistance of tee welded joints in sheet aluminium alloy AMg6. *The Paton Welding J.*, 7, 7–10.
3. Sagalevich, V.M. (1974) *Methods of elimination of welding strains and stresses*. Moscow: Mashinostroenie.
4. Kiselyov, S.N. (1972) *Gas-arc welding of aluminium alloys*. Moscow: Mashinostroenie.
5. Trochun, I.P. (1964) *Internal forces and deformations in welding*. Moscow: Mashgiz.
6. Makhnenko, V.I., Mosenkis, R.Yu. (1985) Calculation of coefficients of stress concentration in butt and fillet welded joints. *Avtomatich. Svarka*, 8, 7–19.
7. Sanders, W.W., Day, R.H. (1969) Fatigue of aluminium alloy weldments. *WRC Bull.*, August, 21.
8. Stepanov, V.G., Klesto, M.I. (1977) *Surface strengthening of hull structures*. Leningrad: Sudostroenie.
9. Stepanov, M.N., Giatsintov, E.V. (1973) *Fatigue of light structural alloys*. Moscow: Mashinostroenie.
10. Hertel, H. (1969) *Ermüdungsfestigkeit der Konstruktionen*. Berlin: Springer.

Received 01.02.2013

# EXPERIENCE IN CLADDING OF PARTS AND UNITS OF CONSTRUCTION AND ROAD-BUILDING MACHINERY

**Ya.P. CHERNYAK**

E.O. Paton Electric Welding Institute, NASU  
11 Bozhenko Str., 03680, Kiev, Ukraine. E-mail: office@paton.kiev.ua

Described is the experience gained in development of technologies and procedures for repair arc cladding of fast-wearing parts and units of various construction and road-building machines and mechanisms (rotary supports of cranes, drive sprockets of caterpillar machines, support and stretch road rollers, caterpillar tracks, etc.). Consumables developed for cladding make it possible to effectively repair parts and units of the construction and road-building machinery by extending their overhaul life. Flux-cored wire PP-AN202 was developed to weld parts and units made from high-carbon hard-to-weld steels. This wire allows repairing them without or with minimal preheating, thus considerably reducing the power consumption in repair operations. The metal deposited with flux-cored wires PP-AN194, PP-AN198 and PP-AN199 features high operating properties. High wear resistance in metal to metal friction and abrasive resistance of these consumables provides a 2–3 times increase in extension of service life of fast-wearing road-building machine parts and mechanisms. Industrial verification of the repaired parts confirmed the high efficiency of the developed consumables and technologies. 5 Ref., 7 Figures.

**Keywords:** *arc cladding, low-alloy and high-carbon steels, fast-wearing parts, construction machinery, welding technology, deposited metal, flux-cored wires, development of technologies*

Many parts or units of construction and road-building machinery are operated under conditions of metal to metal friction with or without an abrasive interlayer. In some cases, wear is accompanied by impact loads, which intensify the wearing process. Such parts are made from medium- or high-carbon unalloyed or low-alloy structural hard-to-weld steels.

The E.O. Paton Electric Welding Institute developed the cladding consumables with high welding-operating properties, as well as the technology and procedure for cladding them. Application of the developed cladding consumables allows extending service life of fast-wearing parts of construction and road-building machinery.

In particular, flux-cored wire PP-AN202 providing the deposited metal with a structure of meta-stable austenite was developed for cladding without or with minimal preheating [1–3]. In contrast to solid wire Np-30Kh10G10, flux-cored wire PP-AN202 contains a decreased amount of carbon and has a modified alloying system. As a result, the metal deposited with this wire had hardness in the as-clad condition at a level of *HRC* 30–35. After cold working, the hardness grew to *HRC* 45–50, and the wear resistance increased. Wire PP-AN202 successfully passed

verification in cladding of high-carbon steel tram rails [4].

Also, the technology and procedure were developed for cladding of rotary supports of different-modification hoisting cranes by using wire PP-AN202. The hoisting cranes are equipped with unified rotary supports: OPU-1190 (OPU-2), OPU-1400 (OPU-3), OPU-1450 (OPU-4), OPU-1600 (OPU-5), OPU-2240 (OPU-6), and OPU-2500 (OPU-7). Physically, a rotary support is a heavy-weight (up to 1.5 t) large-size radial-thrust roller bearing consisting of a gear ring, and upper and lower half-cages. Components of the rotary support are made from high-carbon low-alloy steels of the 50Kh and 50KhGM grades (hardness of roll surface – *HRC* 55–60).

Surfaces of the gear ring and upper and lower half-cages, over which the rollers move, are subjected to repeated deformations, this leading to their wear.

The technology and procedure were developed for cladding of components of the rotary support for a unique crane with a carrying capacity of 250 t. This support differs in design from the mass-produced devices (Figure 1).

Visual examination, dye-penetrant and ultrasonic inspection show that the following defects are characteristic of roll surfaces of the gear and connection rings: non-uniform mechanical wear of races, as well as fatigue wear showing up as microcracks and local separations of metal caused by repeated deformation of the same volumes of metal (Figure 2).

Prior to cladding, the worn-out surfaces and the rings proper were cleaned from dust, dirt, grease and rust. All the surfaces subject to cladding were tested by the dye-penetrant and ultrasonic methods to check the presence of cracks and other defects. The worn-out surfaces of both rings were machined for cladding by using a boring machine up to complete removal of all defects. Thickness of the removed layer on the rings was not in excess of 5 mm. Repeated dye-penetrant and ultrasonic inspection confirmed the absence of the defects after machining.

Self-shielding flux-cored wire PP-AN202 with a diameter of 2 mm was used for cladding of worn-out rings of the rotary support. The surfaces being repaired were clad in sectors: the length of the arc on the outside diameter was 200–250 mm (approximately 50 sectors). Cladding of the rings was performed simultaneously by two cladding operators (Figure 3) on the diametrically opposite regions of the gear ring. Cladding on the internal surface of the connection and gear

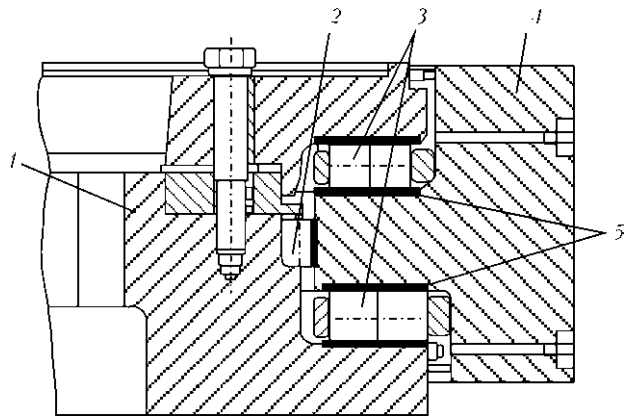


**Figure 1.** Schematic of rotary support: 1 – gear ring; 2 – vertical rollers; 3 – horizontal rollers; 4 – connection ring; 5 – wear locations

rings was performed by one cladding operator also in sectors (the length of the arc was 400–500 mm, following the similar scheme with tilting of the ring using a crane).

Cladding on the horizontal surfaces of the connection and gear rings was performed in two lay-

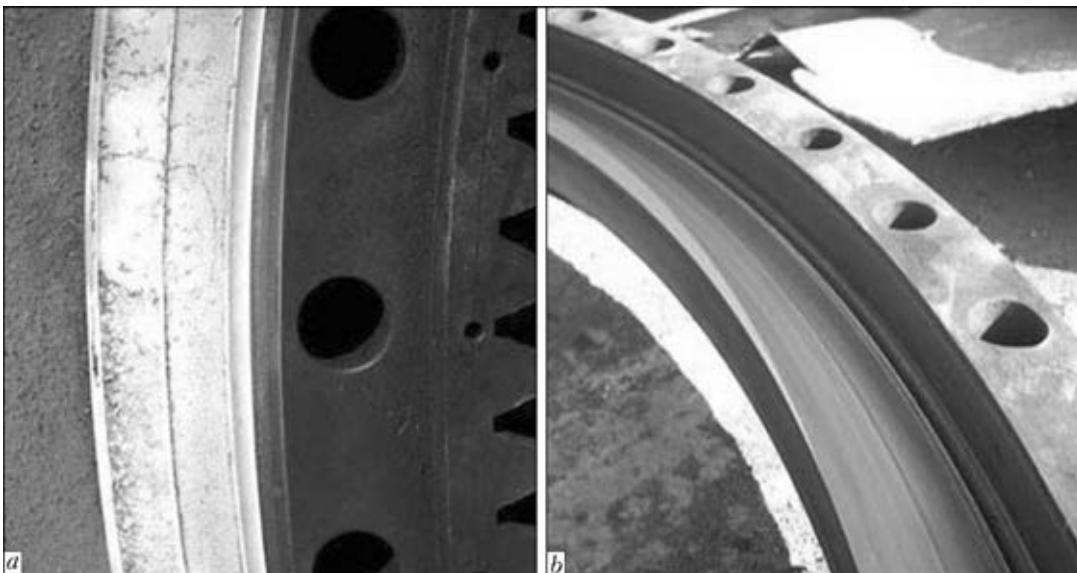


**Figure 2.** Appearance of worn-out roll surfaces of gear (a) and connection (b) rings of rotary support

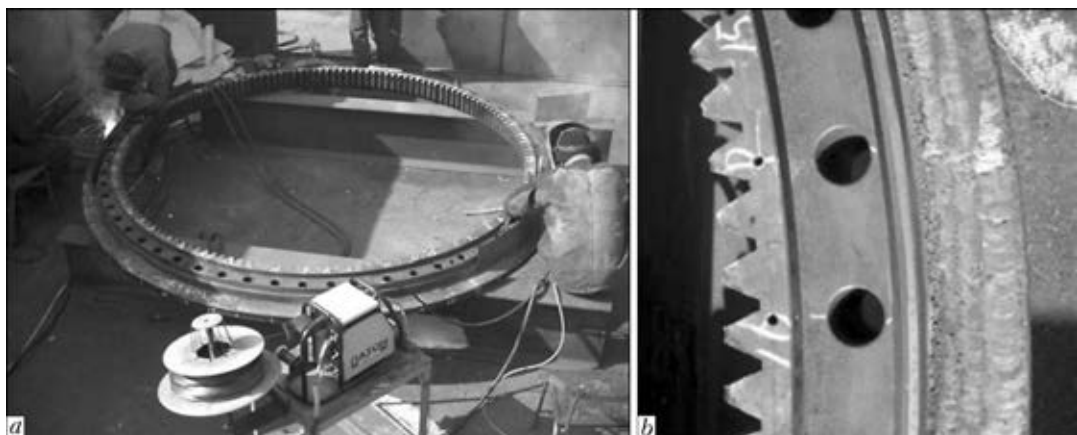


**Figure 3.** Cladding on gear ring simultaneously by two cladding operators (a), and clad region of gear ring (b)



Figure 4. Appearance of repaired drive sprocket of crane KS8165

ers, and that on the internal surface of the connection ring — in one layer. Total thickness of the deposited layer was chosen based on the 1.5–3.0 mm allowance for final machining. After cladding, the clad rings were subjected to slow cooling by wrapping them in heat-insulating materials.

No defects were detected in the deposited layer of the clad rotary support rings by dye-penetrant and ultrasonic inspection after machining. Qual-

ity of the repaired rings allowed using them in the rotary support of crane MKT-250.

The technology for semiautomatic two-layer cladding using two grades of the self-shielding flux-cored wires (Figure 4) was developed to repair gears of the steel 55 drive sprocket of crane KS8165 with a carrying capacity of 100 t. To prevent cracking, the worn-out surface of a gear was clad using flux-cored wire PP-AN1 providing the ductile sub-layer. Flux-cored wire PP-AN199, which provided the deposited metal with hardness *HRC* 43–52, was used to restore geometry of the gears. Wear resistance of this deposited metal (in metal to metal friction at the presence of abrasive) was more than 2 times as high as that of steel 55.

One of the most fast-wearing parts of caterpillar machines is a caterpillar track. About 80 tracks on the average are used in one caterpillar belt, depending on the model. Special problems arise in repair of tracks of large caterpillar cranes. In particular, the roll surface and studs having the shape of a pyramid with a splayed vertex are subjected to wear in tracks of caterpillar crane RDK-25 made from steel 55. The technology for electroslag cladding with two 0.6 × 60 mm section strips (steel 65G) was developed to restore studs of the track of caterpillar crane RDK-25. For-

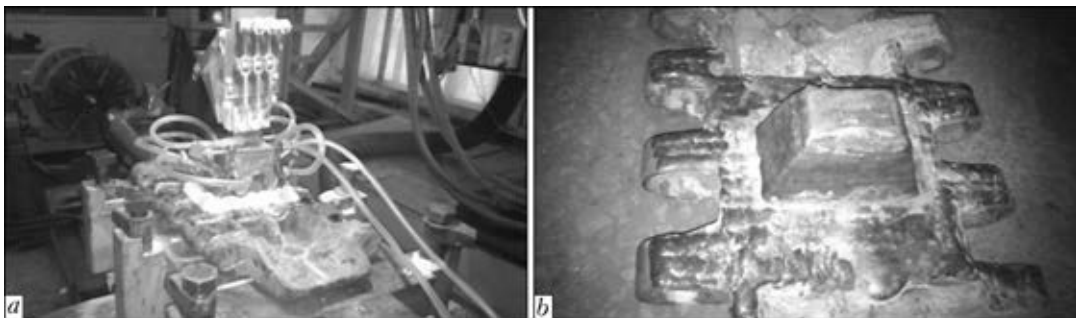


Figure 5. Electroslag cladding of track stud with two strips: *a* — cladding process; *b* — repaired track stud

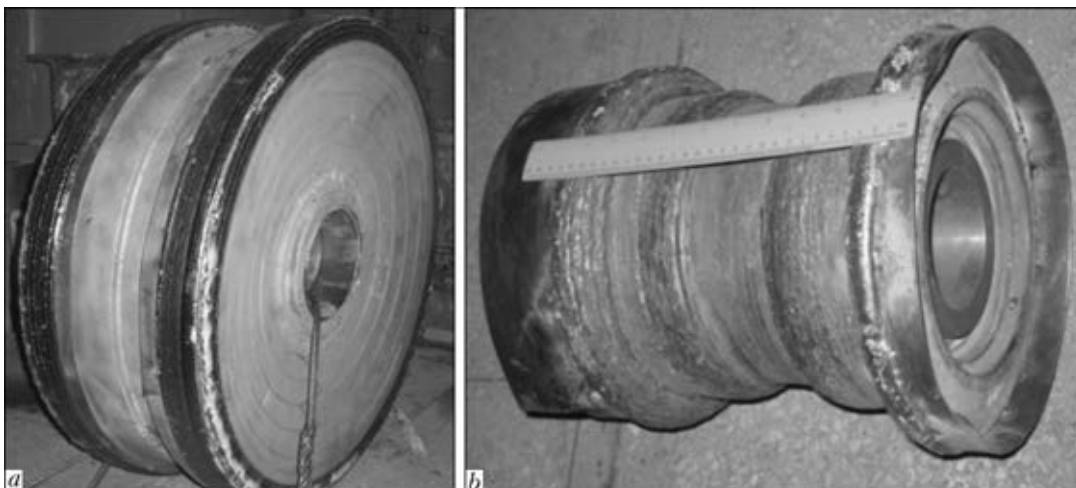


Figure 6. Clad rollers: *a* — stretch roller of bulldozer with diameter of 800 mm; *b* — support roller of excavator Akerman EC450

mation of a stud took place in a copper water-cooled mould (Figure 5). Consumption of the strip for cladding one stud of the track was 4 kg.

Depending on the degree of wear, the roll surface was clad automatically or semiautomatically using the self-shielding flux-cored wire. Here the cost of repair of a track was no more than 30–35 % of the cost of a new track.

Coupled with the caterpillar belt are the stretch and support rolls, which are also subjected to wear. The currently available technologies allow restoring rollers of the caterpillar machines with a diameter of up to 900 mm (Figure 6). The choice of the cladding consumable is based on the roller material. Solid wire Np-30KhGSA and flux-cored wires PP-AN194, PP-AN198 and PP-AN199 are most often applied for cladding of the rollers. Restoration of the imported machine rollers is of a high effect, as the cost of spares for them is very high.

The technology for repair of crane wheels by the arc cladding method is widely applied in industry. Cladding is performed by using solid wire Np-30KhGSA, which provides hardness of the deposited metal equal to *HB* 200–300. For this purpose the E.O. Paton Electric Welding Institute developed sparsely-alloyed flux-cored wire PP-AN194 with phosphorus used as an alloying element, which allowed hardness of the deposited metal to be increased to *HRC* 30–35 [5]. The presence of phosphides in the deposited metal makes it possible to increase wear resistance of the deposited metal more than two times, compared to cladding with wire Np-30KhGSA.

Optimisation of the cladding technology using wire PP-AN194 was performed in restoration of large-size wheels 710 mm in diameter, which are installed on sliding gates of aircraft hangars. Four driving wheels and four driven wheels for such

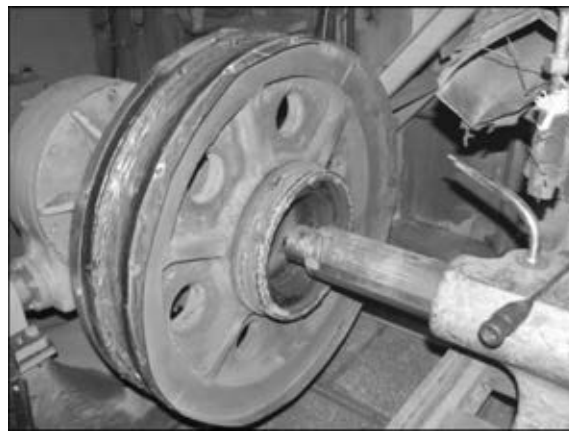


Figure 7. Repaired wheel of sliding hangar gates

gates were restored for Company «Antonov» (Figure 7). The two-year's operation of the restored wheels confirmed the high wear resistance of the deposited metal.

As proved by the industrial experience, the developed arc cladding technologies and consumables allow the construction and road-building machinery parts and units to be repaired with a high efficiency.

1. Kalensky, V.K., Ryabtsev, I.A., Chernyak, Ya.P. *Flux-cored electrode wire for welding and cladding of steel products*. Pat. 39646 Ukraine. Fil. 24.11.2000. Publ. 15.09.2003.
2. Kalensky, V.K., Chernyak, Ya.P., Vasiliev, V.G. et al. (2001) Heat input influence on formation of tears in high-carbon steel building-up with austenitic wires. *The Paton Welding J.*, **11**, 9–12.
3. Chernyak, Ya.P., Bursky, G.V., Kalensky, V.K. (2002) Some peculiarities of delayed fracture of HAZ metal in steel M76 after cladding using austenitic wire. *Ibid.*, **8**, 40–42.
4. Kalensky, V.K., Chernyak, Ya.P., Pritula, S.I. (1999) Repair surfacing of worn out tram rails. *Svarshchik*, **2**, 5.
5. Ryabtsev, I.I., Kuskov, Yu.M., Ryabtsev, I.O. *Composition of steel for surfacing*. Pat. 75682 Ukraine. Int. Cl. B 32 K 35/00. Publ. 15.05.2006.

Received 23.01.2013



## NEWS

## CONTRIBUTION OF SUMY MACHINE BUILDERS IN EQUIPPING OF KOUROU SPACEPORT

PJSC «Sumy M.V. Frunze Machine-Building Science and Production Association» is a part of group of companies «Energetichesky Standart» and one of the largest manufacturers of gascompressor units and packaged compressor stations of different designations, wide nomenclature of pipes, compressors, cen-

trifuges, equipment for chemical, gas and oil-refining industry in Europe.

Press-cutting service of the Company informed that a space project «Soyuz» in the Guiana Space Centre is based on an intergovernmental agreement between the Russian Federation and France signed back in 2003. According to the ambitious program it was planned to construct modern launching complex and develop a new type of rocket-vehicle adapted for launch from French Guiana.

The Association made its contribution in successful launching of «Soyuz-ST» rocket from the Guiana Space Centre also well-known as Kourou spaceport. Sumy machine builders manufactured a series of welded structures for a new launching system (beams, frames and other mechanisms).

The Guiana Space Centre was built on the Atlantic Coast (northeastern coast of South America) and is located just 500 km north of the equator. This provides advantages for launching satellites into geostationary orbit, namely, to make minimal changes in the trajectory of their movement.

Launch vehicles also benefit from the effect of «sling» when energy is created by the Earth's rotation around its axis. Besides, «Soyuz-ST» rocket (new version of «Soyuz-2», specially designed by Russian specialists for launches from Kourou) can place in orbit the spacecraft with greater mass than at the launches from Baikonur and Plesetsk because of such location of the Space Center.





## RULES FOR JOURNAL AUTHORS

*«Avtomaticheskaya Svarka» (Automatic Welding)  
is Published Monthly Since 1948 in Russian, ISSN 005-111X*

*«The Paton Welding Journal» is Published Since 2000 in English, ISSN 0957-798X  
(Translation of «Avtomaticheskaya Svarka» Journal Into English)*

### **Publication of Articles in Journal is Free of Charge, the Fee is not Paid**

1. Standard volume of article shall be 8–10 pages of text including tables, references, 5–6 figures (the volume of review article can be increased up to 12–14 pages). Text shall be printed at 1.5 spacing by Times New Roman, 12 type size.

Information should be described briefly, without repetition of data of tables and figures in the text. References should be given for literature, tables and figures.

Figures should not have the data of secondary importance. Physical units and symbols should be presented using International System of Units SI.

Publication of article will be accelerated if to send it in electron form by E-mail in Word for Windows format. Illustrations shall be presented in separate files in format \*.tif (300 dpi) for raster graphics or \*.cdr (versions of not higher than 11.0, 600 dpi) for vector graphics.

2. The article should not have more than 5 authors (the rest ones, participating in the work, can be mentioned in footnote). Information about author should include affiliation and address, position, scientific title, address, telephone. In addition, the postal address of organization should be given in Russian and English (to take better from official site) and E-mail of one of authors (organization).

3. The article should be added with abstract and key words (from 7 to 10). The abstract (of 1400–1600 characters at a single space between words) should completely enough to describe the article content. It should include the aims and tasks, methods, results, field of application, conclusions.

4. Each article should have a bibliography list, including of not less than 8–10 references (own works of authors should amount to not more than 20 % of the list; references to sources since 2000 are obligatory).

The literature cited in the article should be prepared in the following way:

*for books:* name, initials of author(s), full title, city, publishing house, year of edition, total number of pages;

*for journal articles:* name, initials of author(s), title of article, journal, year of publication, number, volume or issue, pages; foreign publications should be given in the language of original;

*for articles in collection:* title of article, authors, name of collection, number of issue (or volume), place of publication, publishing house (or publishing organization), pages of beginning and end of article; for internet-references: name of resource, access mode.

5. Manuscript of article should be signed by all the authors (or by one author on behalf of author's group). Manuscript should enclose the license agreement for transfer of the author's rights to the editorial board for the article publication. Form of agreement is given on site: [www.paton.kiev.ua](http://www.paton.kiev.ua) or can be sent by the editorial board by E-mail (by request). Non-conformity of materials to the above-mentioned requirements (items 1–5) may serve a reason to refuse a manuscript for publication.

6. Authors of the article can receive free of charge one copy of appropriate numbers of journals «Avtomaticheskaya Svarka» and «The Paton Welding Journal» (by request).

Contacts of Editorial Board of Journal «Avtomaticheskaya Svarka» and «The Paton Welding Journal»:

Tel.: (38044) 200-60-16, 200-82-77; Fax: (38044) 200-82-77, 200-81-45

E-mail: [journal@paton.kiev.ua](mailto:journal@paton.kiev.ua); [www.patonpublishinghouse.com](http://www.patonpublishinghouse.com); URL: [www.rucont.ru](http://www.rucont.ru)

## SUBSCRIPTION FOR «THE PATON WELDING JOURNAL»

If You are interested in making subscription directly via Editorial Board, fill, please, the coupon and send application by fax or e-mail.

The cost of annual subscription via Editorial Board is \$348.

«The Paton Welding Journal» can be also subscribed worldwide from catalogues of subscription agency EBSO.

<b>SUBSCRIPTION COUPON</b>			
Address for journal delivery	_____		
Term of subscription since	20	till	20
Name, initials	_____		
Affiliation	_____		
Position	_____		
Tel., Fax, E-mail	_____		

Subscription to the electronic version of «The Paton Welding Journal»  
can be done at site: URL: [www.rucont.ru](http://www.rucont.ru)



We offer for the subscription all issues of the Journal in pdf format, starting from 2009. You can subscribe to individual issues or to the entire archive including all issues over a period of 2009–2012. The subscription is available for natural persons and legal entities.



## ADVERTISEMENT IN «THE PATON WELDING JOURNAL»

in «Avtomaticheskaya Svarka» and «The Paton Welding Journal»

**External cover, fully-colored:**  
 First page of cover (190×190 mm) – \$700  
 Second page of cover (200×290 mm) – \$550  
 Third page of cover (200×290 mm) – \$500  
 Fourth page of cover (200×290 mm) – \$600

**Internal cover, fully-colored:**  
 First/second/third/fourth page of cover (200×290 mm) – \$400

**Internal insert:**  
 Fully-colored (200×290 mm) – \$340

Fully-colored (double page A3) (400×290 mm) – \$500

- Article in the form of advertising is 50 % of the cost of advertising area
- When the sum of advertising contracts exceeds \$1001, a flexible system of discounts is envisaged

**Size of journal after cutting is 200×290 mm**

**Editorial Board of Journal «Avtomaticheskaya Svarka» and «The Paton Welding Journal»:**

E.O. Paton Electric Welding Institute of the NAS of Ukraine

International Association «Welding»

11, Bozhenko Str., 03680, Kyiv, Ukraine

Tel.: (38044) 200 60 16, 200 82 77; Fax: (38044) 200 82 77, 200 81 45

E-mail: [journal@paton.kiev.ua](mailto:journal@paton.kiev.ua); [www.patonpublishinghouse.com](http://www.patonpublishinghouse.com); URL: [www.rucont.ru](http://www.rucont.ru)